A Study of Quasar Outflows: Physical Characteristics and Feedback Effects

Doyee Byun

Dissertation submitted to the Faculty of the
Virginia Polytechnic Institute and State University
in partial fulfillment of the requirements for the degree of

Doctor of Philosophy
in
Physics

Nahum Arav, Chair
Shunsaku Horiuchi
Jonathan Link
Thomas O'Donnell

August 1, 2024
Blacksburg, Virginia

Keywords: Active galactic nuclei, quasars, quasar outflows, extragalactic astrophysics

A Study of Quasar Outflows: Physical Characteristics and Feedback Effects

Doyee Byun

ABSTRACT

Quasars can affect their surrounding environment through a process known as active galactic nucleus (AGN) feedback, through which the quasar can curtail the formation of stars, regulate the evolution of its host galaxy, and affect its surrounding environment in other ways. One possible mechanism for this process is a quasar's outflow, which can be observed as blueshifted absorption troughs in the quasar's spectrum. With enough kinetic power, an outflow can contribute to AGN feedback, regulating star formation and host galaxy evolution.

By analyzing spectra from the Very Large Telescope (VLT) Ultraviolet Echelle Spectrograph (UVES) and the Hubble Space Telescope (HST) Space Telescope Imaging Spectrograph (STIS), we determined the physical parameters of the absorption outflows of five different quasars: including electron number density (n_e), Hydrogen column density (N_H), ionization parameter (U_H), distance from the source (R), and kinetic luminosity ($\dot{E}_k$). We have found that an outflow's chemical abundance can be a determining factor of its ability to contribute to feedback effects.

Particularly notable outflows include a mini broad absorption line (BAL) outflow system of SDSS J0242+0049, which we estimated to be ~ 67 kpc away from the quasar, which is the farthest distance a mini-BAL has been found from its source. We also found a high-velocity C IV BAL from the same quasar which showed noticeable signs of time variability,

which suggests that the ionization of the outflow has changed over time. Another was SDSS J1321-0041 which displayed BAL troughs of C II and Si II, an unusual feature for an outflow of its type.

In our analysis of the EUV500 BAL of QSO B0254-3327B, we compared it with other EUV500 outflows that have been previously studied, with a total sample of 24 outflows. In that comparison, we have found that the outflow of QSO B0254-3327B was one of the most ionized outflows in the sample. We have also found a weak negative correlation between $\log R$ and $\log |v|$, where R is the distance of the outflow from its source, and v is the velocity of the outflow, with a Spearman rank of -0.43 and p value of 0.05, suggesting that the farther the outflow is from its source, the slower its velocity.

A Study of Quasar Outflows: Physical Characteristics and Feedback Effects

Doyee Byun

GENERAL AUDIENCE ABSTRACT

From the prediction of their existence by general relativity, to the first direct image from the Event Horizon Telescope, black holes have been a fascinating subject for both physicists and the public alike. Most massive galaxies, including our own, are said to have a supermassive black hole (SMBH) at their center. In some galaxies, an accretion disk of orbiting matter forms around the black hole, in which gravitational energy is converted into light. This can sometimes cause the galactic nucleus to shine as bright as a star in the night sky, despite it being tens of thousands of times farther away from us than any star in our own galaxy. Such galactic nuclei are called "quasars", or "quasi-stellar objects".

Some quasars show signs of outflowing gases which can absorb some of their emitted light. These are observed as blueshifted absorption troughs in quasar spectra from telescopes such as the Very Large Telescope (VLT) or the Hubble Space Telescope (HST). It is predicted that, with enough power, these outflows can contribute to a process called active galactic nucleus (AGN) feedback, through which the quasar can curtail the formation of stars, regulate the evolution of its host galaxy, and affect its surrounding environment in other ways.

This dissertation discusses the study of five different quasars and their outflows observed with VLT and HST. We determined the physical parameters of the outflows such as electron number density (n_e), Hydrogen column density (N_H), ionization parameter (U_H), and distance of the outflow from its source (R), to ultimately find each outflow's kinetic luminosity

($\dot{E}_k$), or kinetic power. While we found that some outflows are likely to be able to contribute to AGN feedback, there are a number of unknowns that still remain.

Some interesting outflows we have found include the mini-BAL outflow of SDSS J0242+0049, which we found to be at a distance of ~ 67 kpc (or $\sim 220,000$ lightyears) away from its source, the farthest distance observed to date. We also analyzed the extreme UV outflow of QSO B0254-3327B, which we compared to other outflows observed in a similar wavelength range. In that comparison, we found a weak negative correlation between velocity and outflow distance from the central source, suggesting that the farther away an outflow is from the quasar, the slower it becomes.

To my grandfathers.

할아버지, 사랑합니다.

Acknowledgments

I would like to first thank my advisor, Nahum Arav, for his guidance, insight, and support. It is thanks to his encouragement to challenge myself that I have gained the knowledge and skills to appreciate the wonders of the universe as much as I do. He has always had a knack for making sure I understood the physics without getting lost in the numbers.

I would also like to thank my committee members: Shunsaku Horiuchi, Jonathan Link, and Thomas O'Donnell. Their advice and feedback throughout every step towards my Ph.D. have helped me in immeasurable ways.

I want to thank my group members and collaborators: Nahum Arav, Maryam Dehghanian, Patrick B. Hall, Gerard A. Kriss, Timothy R. Miller, Mayank Sharma, Gwen Walker, and Xinfeng Xu. I have become a better scientist thanks to all of them, and have thoroughly enjoyed the discussions we have had. I also thank Paola Rodriguez Hidalgo, Kirk Korista, and J. Michael Shull for their advice and invaluable insight, as well as the undergraduate researchers who have never ceased to amaze me with their fresh perspectives.

I extend my thanks to my fellow graduate students: Joseph Camilleri, Luis A. Delgadillo, Nick Ekanger, R. Andrew Gustafson, Sarah Healy, Sean Heston, Anri Karanovich, Tommy Lam, Varun Mathur, Ruslan Mukhamadiarov, Mayank Sharma, Junhui Shi, Nicholas W. G. Smith, Ho Lun Tang, Gwen Walker, and Xinfeng Xu. The homework struggles, lunches, drinks, board game nights, movie nights, and philosophical discussions we shared have made my life here as a graduate student so much richer. I am glad to have known so many wonderful people.

I would also like to thank my brothers at Naturally Sharp. Bringing our voices together to

create the most beautiful of sounds on stage was one of the best experiences I have had.

I also thank the friends I have met through KQTx, including Brandon Chong and Mideum Hur, for helping me gain comfort and confidence in my own identity. They have provided me with a sense of community that is both precious and irreplaceable.

Next, I want to thank my dear friend Estelle Tian, for being there for me during both some of the best and the toughest times. Her love and support have been a shining light in my universe.

I also want to thank Soohyun Jeong, BoKyung Kang, Do Hyun Kim, Junhyun Park, Juwon Park, Michael Perez, a Turtle, and Hyuna Yi, for sticking around with me over the years. I am thankful to have them in my life, and am glad to call them my lifelong friends.

Finally, I would like to thank my family. I thank my parents for raising me with love and care, inspiring me, and imparting upon me the values of empathy, compassion, and courage. I also thank my grandparents for rooting for me every step of the way. Last but not least, I thank my brother Seungeui for always having my back. I can confidently say that he is the best brother that anyone could ask for.

Attributions

This dissertation is based on the following papers of which I am the first author:

1. ***Doyee Byun***, *Nahum Arav, Patrick B. Hall, The Farthest Quasar Mini-Broad Absorption Line Outflow from Its Central Source: Very Large Telescope/UVES Observation of SDSS J0242+0049, The Astrophysical Journal, Volume 927, Issue 2, March 2022, Page 176*

2. ***Doyee Byun***, *Nahum Arav, Patrick B. Hall, VLT/UVES observation of the SDSS J2357-0048 outflow, Monthly Notices of the Royal Astronomical Society, Volume 517, Issue 1, November 2022, Pages 1048-1057*

3. ***Doyee Byun***, *Nahum Arav, Gwen Walker, VLT/UVES observation of the outflow in quasar SDSS J1439-0106, Monthly Notices of the Royal Astronomical Society, Volume 516, Issue 1, October 2022, Pages 100-105*

4. ***Doyee Byun***, *Nahum Arav, Mayank Sharma, Maryam Dehghanian, Gwen Walker, Extreme FeLoBAL outflow in the VLT/UVES spectrum of quasar SDSS J1321−0041, Astronomy and Astrophysics, Volume 684, April 2024, Article A158*

5. ***Doyee Byun***, *Nahum Arav, Maryam Dehghanian, Gwen Walker, Gerard A. Kriss, BAL outflow in quasar B0254-3327B: analysis and comparison with other extreme UV outflows, Monthly Notices of the Royal Astronomical Society, Volume 529, Issue 4, April 2024, Pages 3550-3562*

Contents

List of Figures

List of Tables

Preface

This dissertation is based on a collection of published papers of which I am the first author. The chapters are arranged in an order that maximizes thematic consistency and fluidity. In the introduction, I discuss background information necessary for readers to understand the rest of the dissertation, including what quasars are and what we hope to learn from these outflows. Chapters 2–7 discuss the analysis of outflows from individual quasars.

Chapter 1 introduces the reader to the concept of active galactic nuclei (AGN) and quasars. It also describes quasar outflows, and explains their significance in the process known as AGN feedback. Section 1.2 discusses the thin spherical shell model that is used for the analysis conducted in the later chapters, and the following sections describe the different types of outflows that have been analyzed. In writing this chapter, figures from [1–8] have been adapted to illustrate the concepts being explained.

Chapter 2 is based on Ref. [17] "*The Farthest Quasar Mini-Broad Absorption Line Outflow from Its Central Source: Very Large Telescope/UVES Observation of SDSS J0242+0049.*" In this work, we identified and analyzed four absorption outflow systems in the VLT/UVES spectrum of the quasar SDSS J0242+0049. The two most notable of them was a mini-BAL system at $\sim$ 67 kpc away from the quasar, as well as a high velocity BAL system that displayed time variability. I have conducted calculations, created figures, and wrote most of the paper. All authors were involved in discussing and verifying the results.

Chapter 3 is based on Ref. [18] "*VLT/UVES observation of the SDSS J2357-0048 outflow.*" In this work, we analyzed the VLT/UVES spectrum of another quasar, SDSS J2357-0048, in which we found a BAL outflow with four subcomponents, as well as a high-velocity mini-BAL. We analyzed the physical parameters of one of the subcomponents, and examined the

time variability of the mini-BAL. I have conducted most of the calculations and analysis in this work, as well as writing and creating figures. All authors actively participated in the discussion of methodology and results.

Chapter 4 is based on Ref. [19] "*VLT/UVES observation of the outflow in quasar SDSS J1439-0106.*" We analyzed the VLT/UVES spectrum of the quasar SDSS J1439-0106, in which we identified two outflow systems. Only one of them had the necessary diagnostics for finding the outflow distance from its source. I have conducted most of the analysis and calculations, as well as writing and creating figures. All authors were involved in discussing the results.

Chapter 5 is based on Ref. [20] "*Extreme FeLoBAL outflow in the VLT/UVES spectrum of quasar SDSS J1321–0041.*" In this work, we analyzed the extreme FeLoBAL outflow found in the VLT/UVES spectrum of the quasar SDSS J1321-0041. I have conducted the bulk of the analysis and calculations, as well as writing and creating figures. Mayank Sharma assisted in the identification of different energy states of Fe II, Gwen Walker helped with debugging and analytical calculations, and Maryam Dehghanian provided her insight regarding Cloudy [21] simulations. Nahum Arav advised the project through each step. All authors participated in the discussion and interpretation of results.

Chapter 6 is based on Ref. [22] "*BAL outflow in quasar B0254-3327B: analysis and comparison with other extreme UV outflows.*" In this work, we analyzed the HST/STIS spectrum of QSO B0254-3327B, in which we found a BAL outflow. As the wavelength range the outflow was observed in fit into the definition of an EUV500 outflow [2], we also conducted a comparison of its parameters with other EUV500 outflows that have been analyzed in the past. I have conducted most of the analysis, calculation, writing, and creation of figures. Maryam Dehghanian provided her insight in Cloudy simulations, Gerard A. Kriss helped with creating and verifying the spectral energy distribution model used for the analysis,

and Gwen Walker helped with debugging and analytical calculations. Nahum Arav advised the project and provided physical insight. All authors were involved in the discussion and interpretation of results.

While they are not included in this dissertation, I have also been involved as a co-author in the following works studying AGN: Ref. [23] "*High mass flow rate in a BAL outflow of quasar SDSS J1130+0411,*" Ref. [24] "*AGN STORM 2. I. First results: A Change in the Weather of Mrk 817,*" Ref. [25] "*AGN STORM 2. III. A NICER View of the Variable X-Ray Obscurer in Mrk 817,*" and Ref. [26] "*Narrow absorption line outflow in Seyfert 1 galaxy J1429+4518: outflow's distance from the central source and its energetics.*"

Chapter 1

Active Galactic Nuclei and Quasar Outflows

Foreword

In this chapter, I introduce the reader to quasars and active galactic nuclei (AGN), as well as the concept of AGN feedback. I also describe quasar outflows and different types of absorption outflows that are found in the ultraviolet (UV) wavelength range.

Introduction

Quasars were an enigmatic type of object during their early observations. The first known quasar, 3C 273, was simply referred to as a "radio source", marking its prominent radio emission, or a "star-like object", due to its star-like appearance in the visible wavelength range [27, 28] (The two characteristics would later be combined to coin the term "quasar": short for "quasi-stellar radio source"). [28] and [29], through an analysis of the radio emission features, identified the lines of Mg II[1], [O III], as well as several Hydrogen Balmer lines, with their wavelengths significantly lengthened due to cosmological redshift (z=0.158). This led

[1]In accordance with the notation of ions in astronomy, Mg II indicates a transition from the first ionized state Mg^+ to a more highly ionized state. Neutral Mg would be denoted as Mg I.

to the conclusion that 3C 273, and other objects like it, were extragalactic objects with a potential connection to radio galaxies, which display lobes of radio emission outside of the regions which are observed in visible light [30].

Today, quasars are known to be a type of active galactic nucleus (AGN), composed of a black hole, surrounded by an accretion disk of material. Other examples of of AGN previously misidentified as stars exist, such as BL Lacertae [31–33]. Quasars are notable for their extremely large luminosity ($L \gtrsim 10^{45}$ erg s^{-1}), and their outflows are often mentioned in the literature as likely contributors to a process known as active galactic nucleus (AGN) feedback [e.g., 34–36]. In the following sections, we will introduce the concept and a commonly used model of quasar outflows, as well as different types of absorption outflow categories in the UV range.

1.1 Quasar Outflows and Their Observations

A large portion of quasars ($\lesssim 40\%$) show signs of outflowing material, detected as blueshifted absorption troughs in their spectra [37, 38]. As mentioned above, quasar outflows are commonly invoked as potential contributors to AGN feedback: a process through which an AGN affects its surrounding environment. There are several effects of AGN feedback. One of these effects is the mass correlation between the black hole and galactic bulge [e.g., 34, 35, 39–45]. [34] explain that if a quasar's black hole is above a critical mass, its outflowing wind could unbind the host galaxy's material. This provides an upper limit to the mass of the black hole for its host to remain a star forming galaxy, and relates to the black hole and bulge mass correlation described by [46]. Feedback effects also include limitations on the growth of the host galaxy [e.g., 40, 47–52]. Outflows can be a potential explanation for the smaller number of massive or bright galaxies than predicted by theoretical models [47, 53]. Finally,

AGN feedback can contribute to the chemical enrichment of the intergalactic medium (IGM) and intercluster medium (ICM), caused by chemically rich outflows traveling faster than the escape velocity of their galaxies [e.g., 44, 53–57].

Theoretical models suggest that the kinetic luminosity, or kinetic power ($\dot{E}_k$), of an outflow must reach a certain percentage of the quasar's luminosity. [53] argue that it must be 5% for the modeled number density of bright galaxies to match observed values. On the other hand, [58] claim that due to the presence of radiative pressure, 0.5% may be sufficient. As discussed by [2], we take the luminosity of the quasar to be its Eddington luminosity ($L_{\rm Edd}$), which is the maximum luminosity that an object can maintain while staying in hydrostatic equilibrium. The range of observed cosmological redshifts of quasars is quite wide. 3C 273, the first confirmed quasar, was found to have a redshift z=0.158 [28], while more quasars with higher redshifts above 1 were found in later observations [e.g., 59]. More recent observations led to the discovery of quasars with redshifts as high as z=10.1 [60, 61]. As such, gaining an understanding of the interactions between quasars and their surrounding environments will give us deeper insight into the history of galaxy formation and evolution.

Several different types of outflows have been observed and studied. Molecular outflows show signs of molecular transitions such as those of CO, HCN, and HCO, which are often observed with radio instruments such as the Atacama Large Millimeter Array (ALMA), the Submillimeter Array, and the IRAM 30m telescope [e.g., 62–64]. Atomic outflows include outflows detected via H I 21cm absorption features, also observed with radio instruments [e.g., 65, 66]. Ionized outflows can be seen in both emission, such as in integral field spectroscopy [e.g., 67–69], and absorption, such as in optical and UV spectra [e.g., 70–72]. Extremely ionized outflows can be found X-ray spectra as well [e.g., 73–75]. The wide range of outflows is demonstrated in Figure 1.1, and explained in more detail by [1]. While this work focuses on ionized absorption outflows, insight into the different phases of outflows can provide us

with a more holistic understanding of how they operate.

As previously mentioned, absorption outflows are observed as troughs in the spectra of quasars. An example of such is shown in Figure 1.2. Analysis of absorption troughs such as this can reveal the physical characteristics of the outflows, such as hydrogen column density (N_H), ionization parameter (U_H), distance R, and ultimately, kinetic luminosity $\dot{E}_k$.

1.2 The Spherical Shell Model

Due to the limitations of observational data of absorption outflows, we must adapt a kinematic model to approximate their physical parameters. For this purpose, we use a spherical shell model, introduced by [71] and later refined by [14]. As the term suggests, the model assumes that a quasar's outflow is a thin partial spherical shell, with a solid angle $< 4\pi$ which we represent with a normalized parameter called the global covering factor $\Omega < 1$. A typically used value for Ω is 0.2, as that is the approximate portion of quasars that show signs of C IV broad absorption line (BAL) outflows [37, see Section 1.3]. See Figure 1.3 for a visual representation of the model.

According to the model, as outlined by [14], the mass of the outflow M is given by the following:

$$M \simeq 4\pi\Omega R^2 N_H \mu m_p \tag{1.1}$$

where Ω is the aforementioned global covering factor, R is the distance of the outflow from the central source, N_H is the hydrogen column density, $\mu = 1.4$ is the molecular weight per proton, and m_p is the mass of a proton. As we are assuming a thin shell, we use the

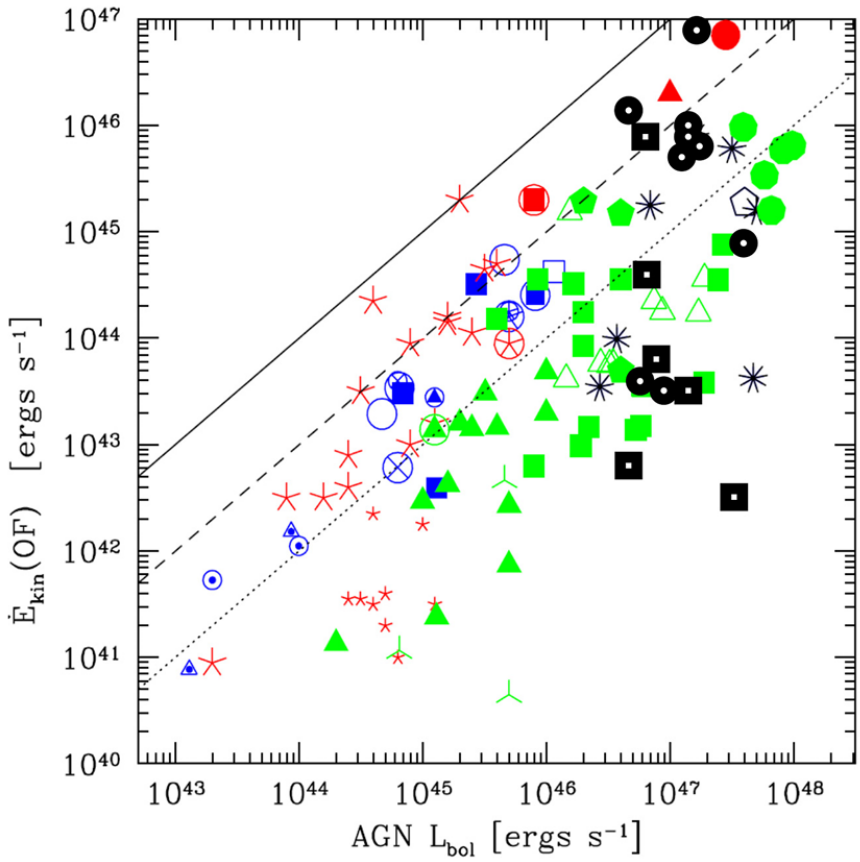

Figure 1.1 Figure 1 of [1], adapted and modified by [2]. $\dot{E}_{kin}(\mathrm{OF}) = \dot{E}_k$, and the dotted, dashed, and solid lines indicate where $\dot{E}_k = 0.01, 0.1$ and $1.0 L_{\mathrm{bol}}$ respectively, where L_{Bol} is the bolometric luminosity of the AGN. **The red, blue, and green points indicate X-ray, molecular, and ionized outflows, while BAL outflows are denoted by black points.** To be more specific, out of the red symbols, the large stars show local ultrafast outflows (UFOs), the starred open circle marks the outflow of Markarian 231, the filled triangle shows the outflow of PDS456, the circled square marks the outflow of IRAS F11119+13257, and the small stars mark slower warm absorbers. Out of the blue points, open circles mark CO outflows, the open square marks the IRAS 23060 outflow, the filled squares mark OH outflows, the starred open circles mark the outflows of Markarian 231, the crossed open circles are the outflows of NGC 6240, the small dotted open triangle marks the measurements in NGC 1068 and NGC 1433, the small dotted open circles mark NGC 1266 and IC 5066, and the squared open circle marks IRAS F11119+13257. Of the green points, filled squares show outflows of AGN at $z > 1$, filled triangles show outflows of AGN with redshifts between 0.1 and 0.2, open triangles show redshifts from 0.4 to 0.6, pentagons show radio galaxies at z=2–3, and filled circles show hyper-luminous quasars at z=2–3. Outf of the black symbols, the pentagon marks the [C II] wind of J1148+5251, while the stars indicate the other BAL outflows reported by [1]. The black circles and squares are EUV500 (see Section 1.5) and S IV absorption outflows (outflows with S IV absorption troughs) reported by [2]. A more detailed explanation can be found in [1] and [2].

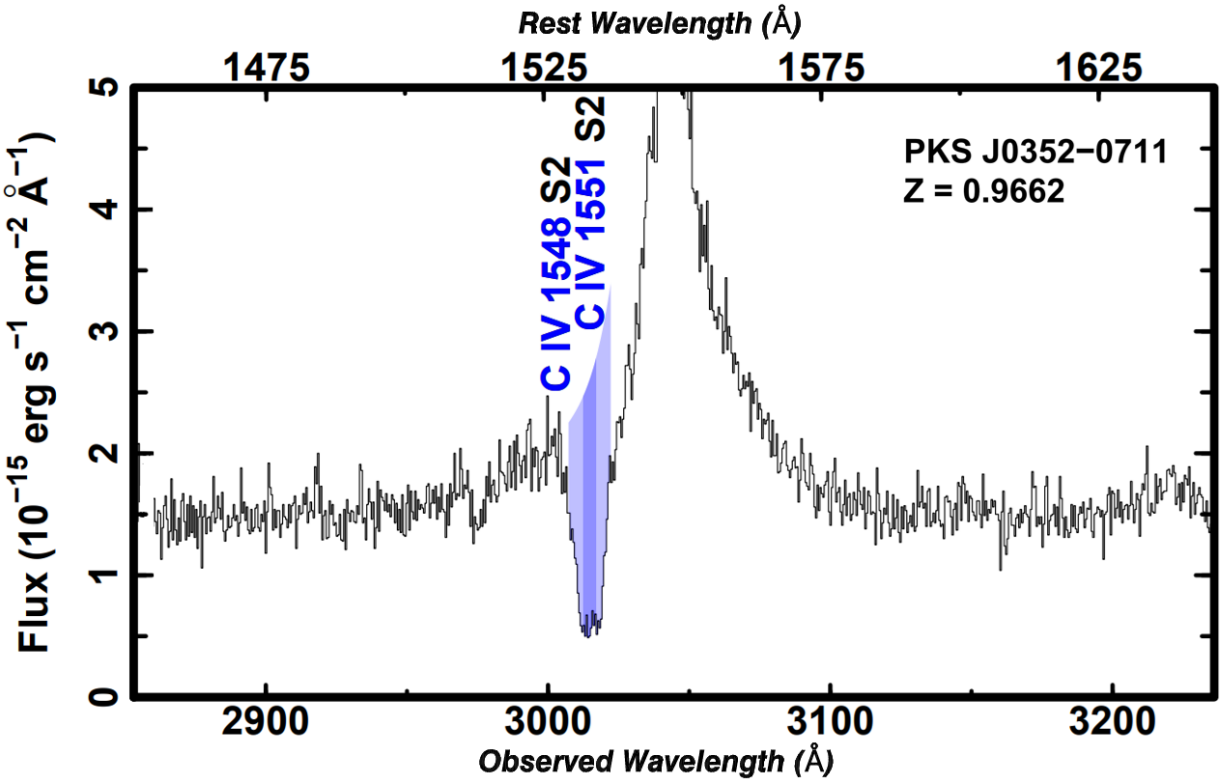

Figure 1.2 A portion of Figure 1 from [3], adapted by [4]. It shows a segment of the HST/COS spectrum of the quasar PKS J0352-0711. The y axis shows the flux, and the top and bottom x axes show the rest and observed wavelengths in angstroms (Å) respectively. Note that at observed wavelength $\lambda_{obs} \approx 3050$ Å, there is a C IV emission feature that has been redshifted due to the cosmological distance of the quasar, while to the left of it, there is an absorption trough from an outflowing gas (shaded in blue), blueshifted relative to the redshifted emission feature.

dynamical time scale $t = R/v$ to find the mass flow rate $\dot{M}$ as follows:

$$\dot{M} \equiv \frac{M}{(R/v)} = 4\pi\Omega R N_H \mu m_p v \tag{1.2}$$

which ultimately leads to the kinetic luminosity:

$$\dot{E}_k = \frac{1}{2}\dot{M}v^2 \tag{1.3}$$

Note that there are three required parameters for this process: N_H, R, and the velocity v. Outflow velocity v is the simplest of the three parameters to find, as it is based on the blueshift of the absorption troughs relative to the systemic redshift of the quasar. The process of finding N_H, which is an analogue for the total column density of the outflow, involves the calculation of ionic column densities and photoionization analysis, which will be further detailed in the following chapters. This process uncovers not only N_H but also the ionization parameter U_H, which is defined as follows:

$$U_H \equiv \frac{Q_H}{4\pi R^2 n_H c} \tag{1.4}$$

where Q_H is the ionizing photon emission rate, n_H is the hydrogen number density of the outflow, and c is the speed of light. Q_H can be found via the quasar's continuum flux level and bolometric luminosity, and n_H can be approximated by finding the column density ratios of different energy levels of the same ion. Using the found values of U_H, n_H, and Q_H, along with Equation 1.4, we can find the distance R. Using the found parameters with Equations 1.2 and 1.3 allows us to find $\dot{M}$ and $\dot{E}_k$. Comparing $\dot{E}_k$ with L_{Edd} ultimately allows us to determine the feasibility of AGN feedback contributions by the outflow.

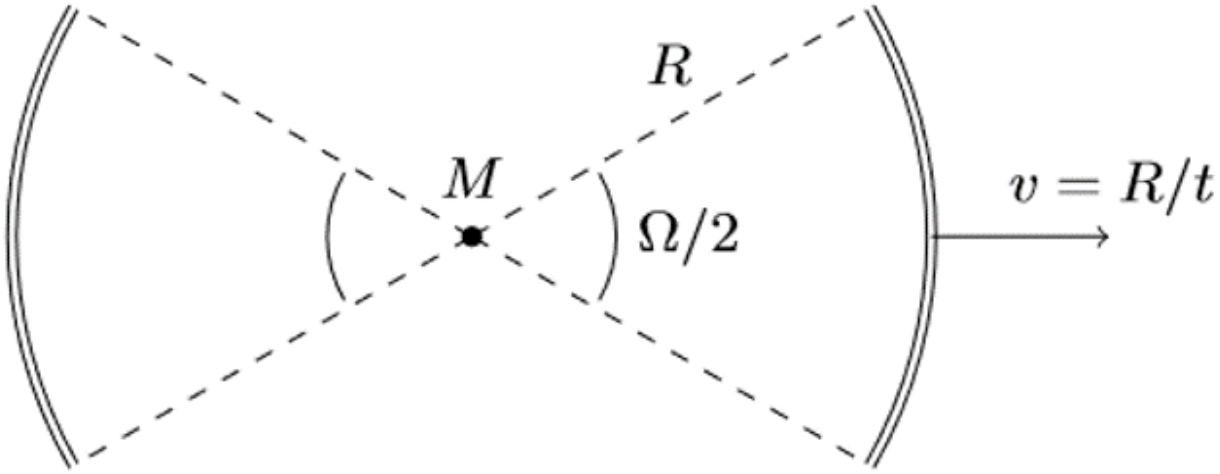

Figure 1.3 Diagram by [5] representing the geometry of the spherical shell model of quasar outflows.

1.3 BAL and Mini-BAL Outflows

A category of absorption outflows that is commonly referred to is broad absorption line (BAL) outflows. [76] define a BAL as an absorption outflow with continuous C IV absorption that reduced flux by at least 10% over a velocity width $\Delta v \geq 2000$ km s^{-1}, starting from at least -3000 km s^{-1}. Many outflows that fit into this category have been studied over the years [e.g., 77–80]. An example of an outflow that fits well into this category is shown in Figure 1.4. Note that not all BAL outflows are able to fit into this category, as will be further explained in Sections 1.4 and 1.5. Outflows that do not quite reach the width threshold of a BAL are called mini-BALs. Mini-BALs are defined as outflows with a velocity width between 500 and 2000 km s^{-1} [81]. Likewise with BALs, the mini-BAL outflows of several quasars have been analyzed for their physical characteristics [e.g., 7, 17].

As described in Section 1.2, finding the distance (R) of a BAL (or mini-BAL) outflow from its central source requires finding its hydrogen number density (n_H). n_H can be approximated by finding the column density ratio between the resonance and excited states of an ion, a

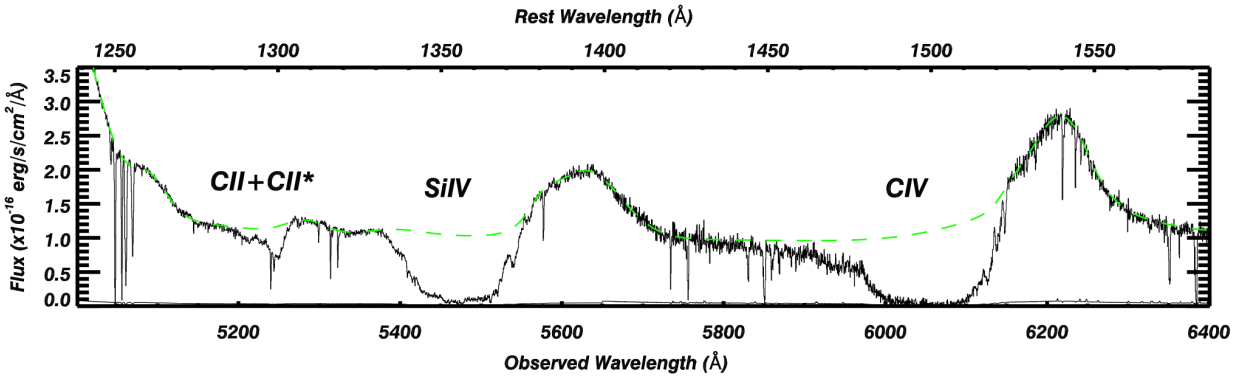

Figure 1.4 A portion of the X-Shooter spectrum of the quasar SDSS J1106+1939 as shown in Figure 1 of [6]. The black curve shows the data, while the green dashed curve shows the continuum and emission model without the absorption. Note the presence of broad Si IV absorption along with the C IV trough.

method that has been conducted in many studies in the past [e.g., 6, 7, 79, 82]. For instance, [7] compared the column densities of the resonance and excited states of S IV in the mini-BAL outflow of the quasar SDSS J1111+1437, of which the troughs are shown in Figure 1.5. Given the ratio between energy states, computational software such as Cloudy [21] or Chianti [12, 13] can calculate the electron number density n_e via collisional excitation modeling. As $n_e \approx 1.2 n_H$ in highly ionized plasma [83], the n_e solution allows for an approximation of n_H and, by extension, R.

1.4 FeLoBALs

Among the category of BALs, there is a type of outflow in which there is prominent absorption of Fe II, and in some cases, Fe III. These low-ionized iron BALs, or FeLoBALs, offer a plethora of diagnostics for n_e due to the presence of Fe II absorption troughs of multiple excited state transitions. Thanks to this, an extensive amount of analysis of FeLoBALs has been conducted [e.g., 80, 84, 85]. The blending of troughs can add difficulty to the identification of individual absorption lines (See Figure 1.6, [8]). The limitation due to blended

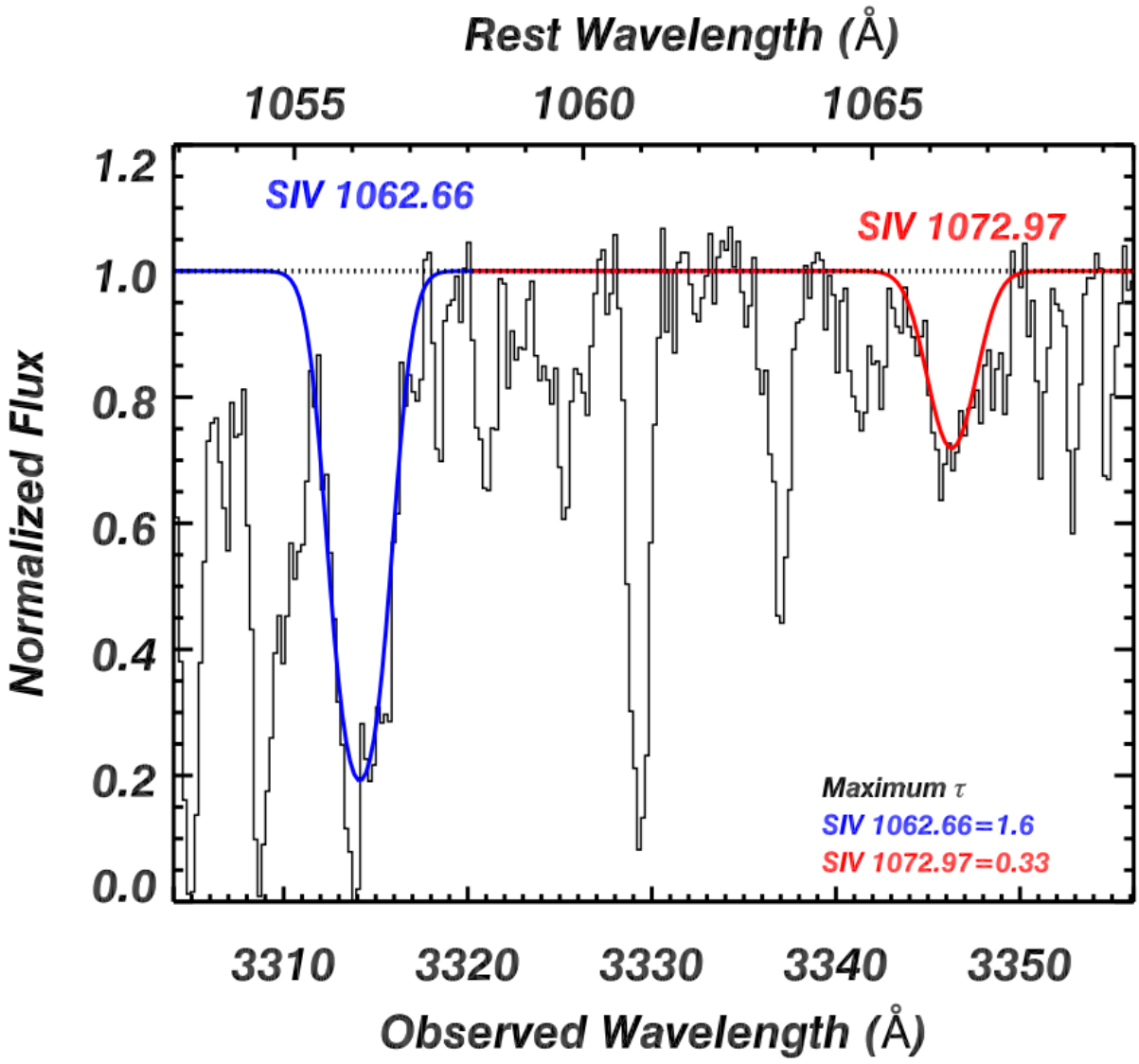

Figure 1.5 A portion of the normalized X-Shooter spectrum of SDSS J1111+1437, adapted from [7]. The black curve shows the spectrum, while the dotted line indicates the continuum without absorption. The blue and red curves show the Gaussian fitting models of the S IV resonance and excited state troughs, respectively. The column density ratios from troughs such as these allow for an approximation of the distance of the outflow from its central source.

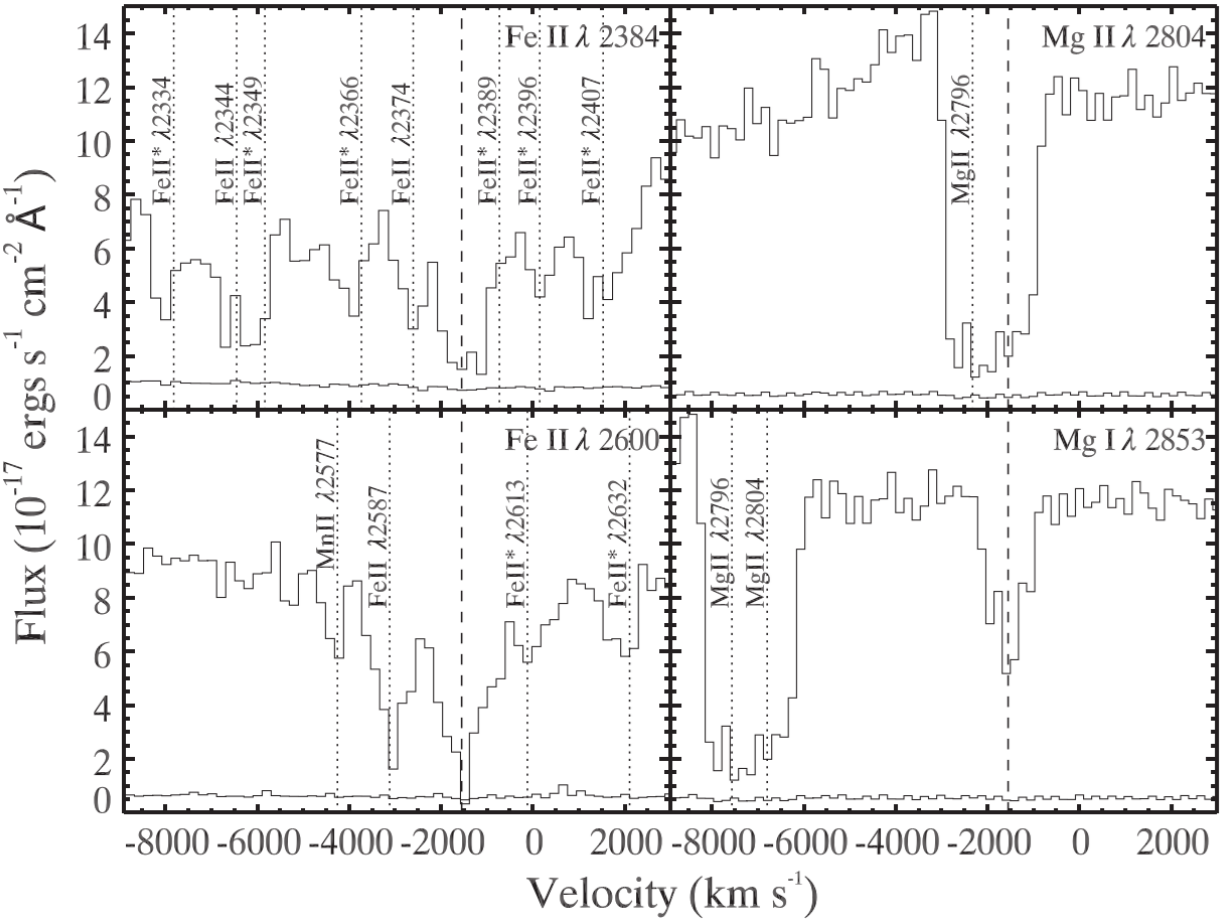

Figure 1.6 Absorption troughs of the quasar SDSS J0802+5513, adopted from [8]. The x-axis shows the velocity of the outflow indicated by the troughs marked by the dashed vertical lines. The dotted lines mark other absorption troughs in the same system. Note the upper left panel in which the absorption features of multiple Fe II lines are blended.

absorption troughs has led to different spectral simulation methods such as the Synthetic Spectral Simulation (SSS) method [23, 86], and SimBAL [84], both of which simulate the absorption troughs of an outflow in a spectrum given its physical parameters.

1.5 EUV500 Outflows

Absorption outflows observed at extreme UV wavelengths (rest wavelength between 500–1050 Å) are called EUV500 outflows [2]. Notable for prominent absorption features of very highly ionized species such as Ne VIII, Na IX, and Mg X [e.g., 9, 16, 82], EUV500 outflows are rich in diagnostic lines that can help determine their physical characteristics (See Figure 1.7, [9]).

As can be seen in Figure 1.7, C IV is outside of the EUV500 range, making the aforementioned criteria for BALs by [76] inapplicable. Due to this limitation, [9] adjusted the definition of a BAL in the EUV500 range to cover velocity widths of $\Delta \gtrsim 1500$ km s^{-1}, regardless of which ion.

As previously discussed in Section 1.1, the effects of AGN feedback can be instrumental in bridging the gap between observations and theoretical models in galaxy evolution, as well as provide an explanation for the chemical enrichment of the IGM and ICM. Studying quasar outflows, which could potentially be an agent of feedback, can help us improve the understanding of these phenomena. The following chapters cover analyses conducted on BALs and mini-BALs found in the spectra of five different quasars. Chapters 2, 3, and 4 discuss the analysis of outflows found in the Very Large Telescope (VLT) Ultraviolet Echelle Spectrograph (UVES) spectra of quasars, some of which display an intriguing amount of time variability. Chapter 5 discusses an extreme FeLoBAL. Chapter 6 discusses the analysis of an EUV500 BAL, along with a comparison of that outflow with other EUV500 outflows.

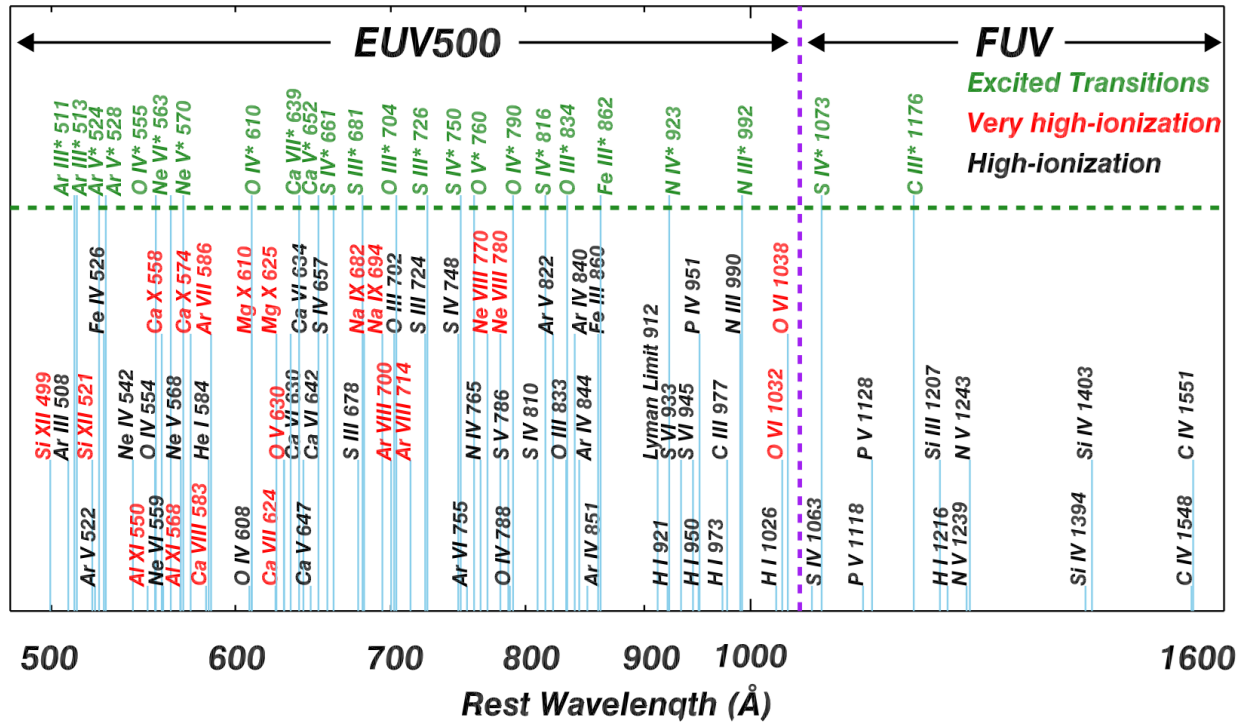

Figure 1.7 Comparison of diagnostic lines in the EUV500 wavelength range, and those in the far UV range in which C IV and Si IV are observed. Adopted from [9]. The large number of excited transitions allows for more measurements of n_e, leading to a more accurate approximation of distance R.

Chapter 2

The Farthest Quasar Mini-BAL Outflow from its Central Source: VLT/UVES Observation of SDSS J0242+0049

Foreword

This chapter is based on the published paper "*The Farthest Quasar Mini-BAL Outflow from its Central Source: VLT/UVES Observation of SDSS J0242+0049*" [17]. I led the project by analyzing the data, doing calculations, creating the figures, and writing the paper.

2.1 Abstract

We analyze VLT/UVES observations of the quasar SDSS J024221.87+004912.6. We identify four absorption outflow systems: a C IV BAL at $v \approx -18,000$ km s^{-1}, and three narrower low-ionization systems with centroid velocities ranging from –1200 to –3500 km s^{-1}. These outflows show similar physical attributes to the [O III] outflows studied by [87]. We find that

two of the systems are energetic enough to contribute to AGN feedback, with one system reaching above 5% of the quasar's Eddington luminosity. We also find that this system is at a distance of 67 kpc away from the quasar, the farthest detected mini-BAL absorption outflow from its central source to date. In addition, we examine the time variability of the BAL, and find that its velocity monotonically increases, while the trough itself becomes shallower over time.

2.2 Introduction

Quasar absorption outflows are seen in a large fraction of quasar spectra ($\lesssim$ 40%), often detected via blueshifted absorption troughs in the rest frame of quasars [37, 38, 88]. These outflows are often mentioned as likely candidates for producing AGN feedback [e.g., 34–36, 47, 53]. According to theoretical models, outflow systems require a kinetic luminosity ($\dot{E}_k$) of at least $\sim$ 0.5% [58] or $\sim$ 5% [53] of the quasar's Eddington luminosity (L_{Edd}) to contribute to AGN feedback. Outflow systems that fit these criteria have been found [e.g., 9, 14, 16, 77, 82, 86, 89–91].

The kinetic luminosity of a quasar's outflow system is dependent on its distance from its central source (R), which we can find by measuring both the electron number density (n_e) and ionization parameter (U_H) [92]. Our group and others have used this method to find the distances of outflow systems in the past [7, 9, 82, 92–96]. Using the ratios between excited and resonance state column densities of ionized species (N_{ion}) can lead us to a value of n_e [97]. This paper presents one such determination of the R and $\dot{E}_k$ values of three outflow components found in the VLT/UVES spectrum of SDSS J024221.87+004912.6 (hereafter J0242+0049).

The analysis of J0242+0049 shown in this paper is based on data from the VLT/UVES

Spectral Quasar Absorption Database (SQUAD) published by [10], containing the spectra of 475 quasars. Analysis of more SQUAD objects will be conducted in the future.

The UVES data of J0242+0049 is from the program 075.B-0190(A) which [98] used to identify a high velocity C IV broad absorption line (BAL) at $z \approx 1.88$ ($v \approx -18,000$ km s^{-1}), as well as two mini-BAL outflows and one narrow absorption line (NAL) outflow at lower velocities; all four of which we have identified independently. Comparing the UVES spectrum to SDSS spectra from previous epochs, [98] have identified a shift in the velocity of the high velocity BAL, which could potentially be explained by acceleration. They have also found potential line locking in the Si IV absorption doublets of the two lower velocity mini-BAL systems. In addition to the analysis of the UVES data, we conduct a follow up to their observation of the velocity shift using SDSS observation data from more recent epochs.

This paper is structured as follows. Section 2.3 discusses the observation of J0242+0049, as well as the data acquisition process. In Section 2.4, we present the ionic column density measurements, and the process of finding n_e and U_H. Section 2.5 shows the results of the analysis, including the energetics parameters of the outflow systems. We also show observations of the high velocity BAL from recent SDSS epochs. Section 2.6 provides a discussion of the results, and Section 2.7 summarizes and concludes the paper. For this analysis, we adopt a cosmology of $h = 0.696$, $\Omega_m = 0.286$, and $\Omega_\Lambda = 0.714$ [99], and use the Python astronomy package Astropy [100, 101] for cosmological calculations.

2.3 Observation, Data Acquisition, and Line Identification

The quasar J0242+0049 (J2000: RA=02:42:22, DEC=+00:49:12.6; z=2.06) [102] was observed in September 5, 2005 with the VLT/UVES as part of the program 075.B-0190(A), with resolution $R \simeq 40,000$ and wavelength coverage from 3291 to 9300 Å[98]. The systemic redshift z=2.06 given by [10] is consistent with the value we find based on the Mg II emission line in the SDSS spectrum of the MJD=57758 epoch. The spectral data was reduced and normalized by its continuum and emission by [10] as part of their SQUAD database. Broad and narrow absorption lines have been found in the spectrum of J0242+0049 by [98], which we identify here as NAL S1 at –1200 km s^{-1} (Ly α FWHM = 240 km s^{-1}), mini-BAL S2 at -1800 km s^{-1} (N v FWHM = 900 km s^{-1}), mini-BAL S3 at –3500 km s^{-1} (N v FWHM = 720 km s^{-1}), and the aforementioned BAL S4 at –18,000 km s^{-1}, as shown in the full spectrum in Figure 2.1. Following [76], a BAL is a continuous absorption feature below 0.9 normalized intensity over 2000 km s^{-1}, a mini-BAL is the same but between 500 and 2000 km s^{-1} [81], and a NAL is an absorption feature with width below 500 km s^{-1}. We measure the width of S4 at 0.9 normalized intensity to be 2200 km s^{-1}, which is above the threshold of a BAL, with balnicity index as defined by [76] of 660 km s^{-1}. [103] have identified four C IV absorption systems, two of which coincide with systems S3 and S4. We label the other two as systems A and B, and show them in Figure 2.1. The focus of this paper is on the four systems S1, S2, S3, and S4. We do not discuss systems A and B because they only show absorption in C IV, which does not lend itself to further analysis.

The outflows show absorption from low ionization species such as Si II, C 2, and Fe II, as well as lines of Ly α, C IV, N V, P V, Mg II, Al II, and Al III. For the purpose of measuring the ionic column densities, we convert the normalized spectrum data from wavelength to

Epoch in MJD	Spectrograph	Plate	Fiber	Observed Date	Wavelength Coverage (Å)
52177	SDSS	707	332	Sep. 25, 2001	3824–9215
52199	SDSS	706	617	Oct. 17, 2001	3820–9202
55455	BOSS	4240	754	Sep. 16, 2010	3590–10382
57758	BOSS	9381	79	Jan. 5, 2017	3573–10334

Table 2.1 SDSS Spectra Information

velocity space via the systemic redshift of the quasar, as shown in Figure 2.2. Note that S2 appears to be composed of at least seven sub-components, as seen in Plot (l) of Figure 2.2. The components are blended in the absorption troughs of C IV and Si IV, and due to the shallowness of the C II* troughs, it is impossible to decompose it into the different sub-components. For this reason, they are treated as a singular absorption system for the sake of the analysis in this paper.

For the velocity shift analysis, SDSS spectra from MJD=52177, 52199, 55455, and 57758 were retrieved and corrected for galactic extinction with $E(B-V) = 0.0269$ [104]. The spectra from both the BOSS and SDSS spectographs have spectral resolutions of $R \approx 2000$ [102, 105, 106]. More details on the SDSS spectra can be found in Table 2.1.

2.4 Analysis

2.4.1 Ionic Column Density

To find the physical characteristics of the outflow systems, we first find the column densities of the observed ions (N_{ion}). The simplest method of measuring column densities is by assuming the apparent optical depth (AOD) of a uniformly covered homogeneous source, as demonstrated by [107]. When calculating column density under this assumption, we first assume the relation between intensity and optical depth as follows [see equation 1 of 107]:

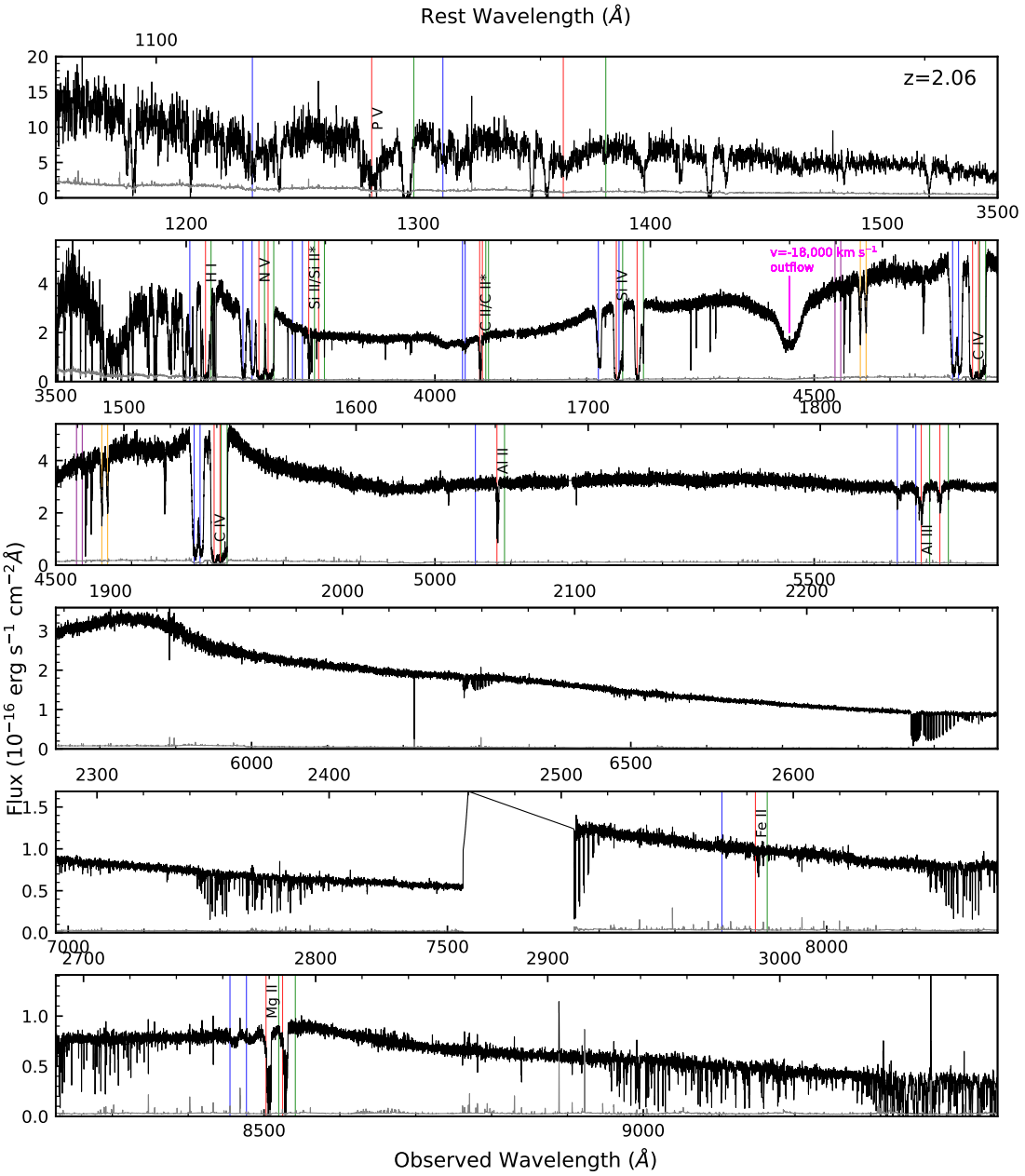

Figure 2.1 Normalized flux of J0242+0049 multiplied by the emission model by [10], based on the SQUAD data set. The flux has been scaled to match the BOSS spectrum from the epoch of MJD=57758 (Jan. 5, 2017) at observed wavelength $\lambda = 6500$ Å. The black curve represents the flux, and the gray shows the error in flux. The green, red, and blue vertical lines mark absorption troughs of outflow systems S1, S2, and S3, respectively, while the S4 C IV BAL is labeled in magenta. Systems A and B are marked in orange and purple respectively. Note that the absorption troughs for S1 are significantly narrower when compared to those of S2 and S3.

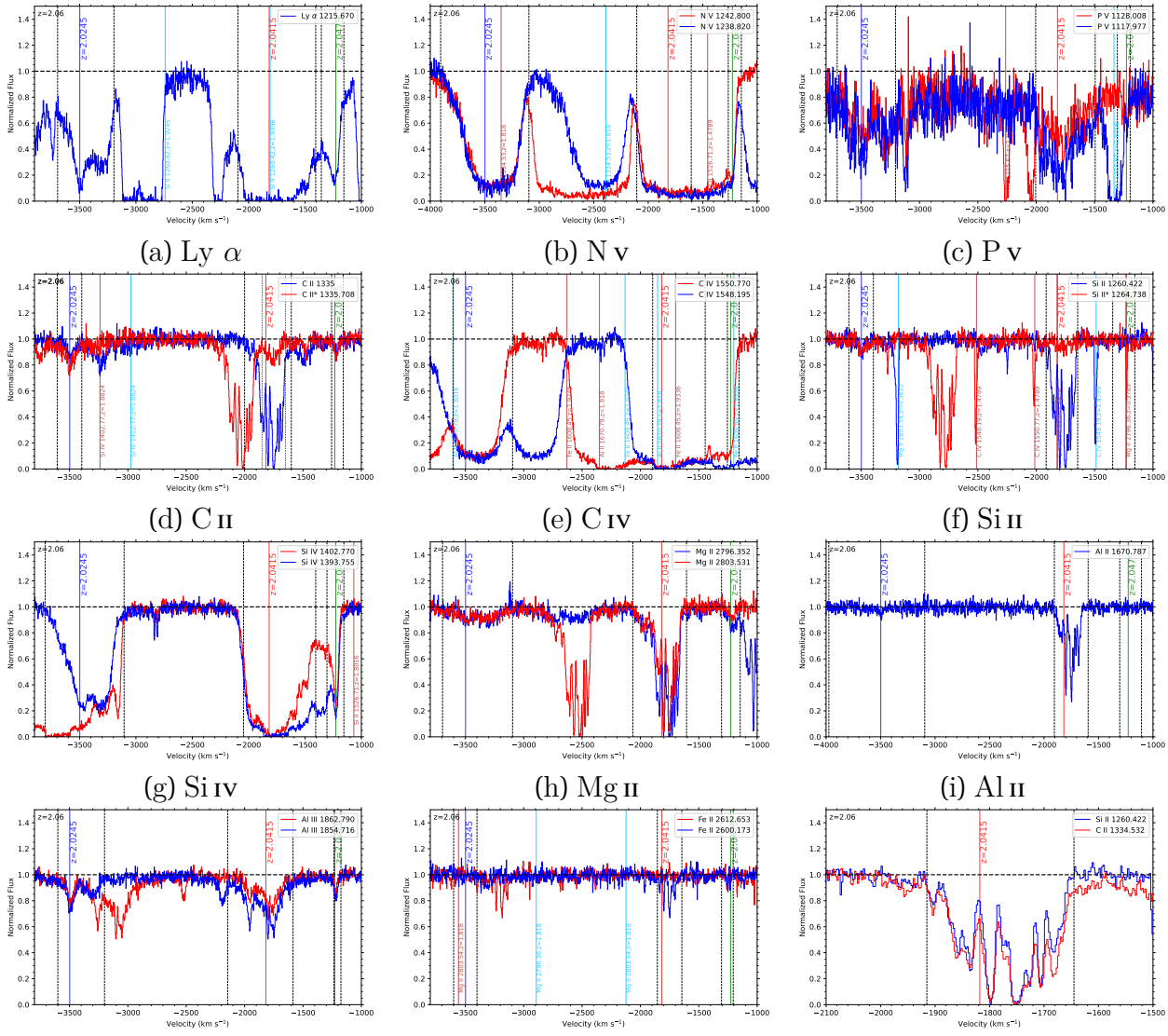

(a) Ly α (b) N v (c) P v

(d) C ii (e) C iv (f) Si ii

(g) Si iv (h) Mg ii (i) Al ii

(j) Al iii (k) Fe ii (l) C ii & Si ii

Figure 2.2 Normalized spectrum plotted in velocity space for each ion in the absorption systems. The green, red, and blue vertical lines represent the velocity of systems S1, S2, and S3, respectively. The dotted vertical lines show the integration ranges used for the calculation of the ionic column densities. The horizontal dashed line represents the continuum level. Intervening absorption systems that contaminate the blue spectra are marked with cyan vertical lines, while intervening systems contaminating the red spectra are marked with brown vertical lines. Note in Plot (f) that the S1 integration range for Si ii 1265Å is contaminated with Mg ii 2796Å absorption of the z=0.3783 intervening system. Plot (l) shows the structure of the S2 absorption trough of Si ii and C ii, on a narrower velocity scale.

$$I(\lambda) = I_0(\lambda)e^{-\tau(\lambda)} \tag{2.1}$$

where $I(\lambda)$ is the intensity, $I_0(\lambda)$ is the intensity without absorption, and $\tau(\lambda)$ is the optical depth as a function of wavelength. When writing optical depth as a function of outflow velocity, it has a relation with column density $N(v)$ of [see equation 8 of 107]:

$$\tau(v) = \frac{\pi e^2}{m_e c} f\lambda N(v) \tag{2.2}$$

where m_e is the mass of an electron, e is the elementary charge, and f and λ are the oscillator strength and wavelength of the transition line, respectively. Finding $N(v)$ and integrating it over the velocity range of the absorption trough yields the column density based on the AOD assumption. The AOD method is used to find lower limits of N_{ion} for singlets or contaminated doublets, or upper limits when there are no discernible absorption troughs.

When there are multiple lines of the same ion and energy state, we can use the partial covering (PC) method, which assumes a homogeneous source partially covered by the outflow [108–110], and solves for a velocity dependent covering factor [111, 112], to improve our measurements by taking phenomena such as non-black saturation into account [113, 114]. When calculating the PC based column density of an ion with a doublet of transition lines, we find the covering fraction $C(v)$ via the following relations [see equations 2 & 3 of 112]

$$I_R(v) - [1 - C(v)] = C(v)e^{-\tau(v)} \tag{2.3}$$

$$I_B(v) - [1 - C(v)] = C(v)e^{-2\tau(v)} \tag{2.4}$$

where $I_R(v)$ and $I_B(v)$ are the normalized intensities of the red and blue absorption features respectively, and $\tau(v)$ is the optical depth of the red component.

We choose integration ranges that cover visible absorption in the data, as can be seen in Figure 2, while minimizing the effects of blending and contamination. For instance, for Si IV, we use the blue line for S3 and the red line for S2. Si II* of S1 shows contamination due to an intervening absorption feature, so we use the measured column density as an upper limit for the sake of our analysis. C IV of S2 is heavily blended between the red and blue features, so we choose a velocity range in which the blue and red spectra do not overlap with each other in order to find a lower limit of the column density.

Attempting a Gaussian fit of the C IV absorption of S2 yields a poor fit due to the saturation of the trough. Calculating the column density based on the fit results in a lower limit of $2400 \times 10^{12}\text{cm}^{-2}$, compared to the measured lower limit of $3900 \times 10^{12}\text{cm}^{-2}$. This difference does not affect the solution of the hydrogen column density and photoionization parameter as described in Section 2.4.2.

The measured column density values can be found in Table 2.2. Note that most adopted values in Table 2.2 are upper or lower limits. The errors in the column densities are propagated from the errors in the normalized flux from the data, binned along with the data into segments of $\Delta v = 10$ km s^{-1} for numerical integration. 20% error is added in quadrature for the column density values adopted for photoionization analysis (see last column of Table 2.2) to take into account the uncertainty in the modeled continuum level [7].

Table 2.2: J0242+0049 Outflow Ionic Column Densities

Troughs	AOD	PC	Adopted
		S1, $v = -1200$ km s^{-1}	
H I	$177.0^{+1.9}_{-1.8}$		$> 180_{-40}$
N v	467^{+5}_{-5}		$> 470_{-90}$
P v	56^{+4}_{-4}		$> 50_{-10}$

Table 2.2: J0242+0049 Outflow Ionic Column Densities

Troughs	AOD	PC	Adopted
C II total	26^{+2}_{-2}		$> 26_{-5}$
C II 1335	$10.8^{+1.5}_{-1.2}$		
C II* 1336	$14.7^{+1.5}_{-1.3}$		
C IV	350^{+5}_{-4}		$> 350_{-70}$
Si II total	$5.5^{+0.3}_{-0.4}$		$< 5.5^{+1.2}$
Si II 1260	$1.3^{+0.3}_{-0.2}$		$< 1.3^{+0.4}$
Si II* 1265	$2.8^{+0.2}_{-0.2}$		$< 2.8^{+0.6}$
Si IV	$92.6^{+1.0}_{-1.0}$		$> 90_{-20}$
Mg II	$2.7^{+0.3}_{-0.3}$		$> 2.7_{-0.6}$
Al II	$0.3^{+0.09}_{-0.08}$		$< 0.3^{+0.1}$
Al III	$3.3^{+0.3}_{-0.3}$	$4.9^{+0.8}_{-0.5}$	$4.9^{+1.3}_{-1.1}$
Fe II	$1.9^{+0.4}_{-0.3}$		$< 1.9^{+0.5}$
S2, $v = -1800$ km s^{-1}			
H I	1680^{+180}_{-10}		$> 1680_{-340}$
N V	4620^{+30}_{-30}		$> 4620_{-920}$
P V	450^{+10}_{-10}		$> 450_{-90}$
C II total	740^{+90}_{-10}		$> 740_{-150}$
C II 1335	690^{+90}_{-10}		
C II* 1336	50^{+2}_{-2}		
C IV	3910^{+330}_{-20}		$> 3910_{-780}$
Si II total			$> 80_{-20}$
Si II 1260	$77.6^{+1.3}_{-1.1}$		$> 80_{-20}$
Si II* 1265	$2.9^{+0.3}_{-0.3}$		$< 3^{+0.7}$

Table 2.2: J0242+0049 Outflow Ionic Column Densities

Troughs	AOD	PC	Adopted
Si IV	1410^{+100}_{-10}		$> 1410_{-280}$
Mg II	$84^{+1.0}_{-0.9}$	$90.7^{+1.0}_{-1.0}$	90^{+20}_{-20}
Al II	$10.3^{+0.2}_{-0.1}$		$> 10_{-2}$
Al III	$48.4^{+0.9}_{-0.9}$	$55.6^{+0.9}_{-0.8}$	55^{+10}_{-10}
Fe II total			$> 12_{-2.5}$
Fe II 2600	$12.2^{+0.5}_{-0.5}$		$> 12_{-2.5}$
Fe II* 2612	$1.0^{+0.5}_{-0.5}$		$< 1.0^{+0.5}$
S3, $v = -3500$ km s^{-1}			
H I	$417.7^{+3.7}_{-3.4}$		$> 420_{-80}$
N V	3780^{+20}_{-20}		$> 3780_{-760}$
P V	390^{+10}_{-10}		$> 390_{-80}$
C II total	$94.2^{+3.5}_{-3.3}$		$> 90_{-20}$
C II 1335	$32^{+2.4}_{-2.2}$		
C II* 1336	$62.1^{+2.5}_{-2.5}$		
C IV	2180^{+10}_{-10}		$> 2180_{-440}$
Si II total	$5.1^{+0.4}_{-0.3}$		$> 5.1_{-1.1}$
Si II 1260	$2.5^{+0.3}_{-0.3}$		
Si II* 1265	$2.6^{+0.2}_{-0.2}$		
Si IV	$285.8^{+1.5}_{-1.4}$		$> 290_{-60}$
Mg II	$17.9^{+0.6}_{-0.6}$		$> 18_{-4}$
Al II	$2^{+0.2}_{-0.2}$		$< 2^{+0.4}$
Al III	$19.7^{+0.4}_{-0.4}$		$> 20_{-4}$
Fe II total	$6.7^{+0.7}_{-0.9}$		$< 6.7^{+1.5}$

Table 2.2: J0242+0049 Outflow Ionic Column Densities

Troughs	AOD	PC	Adopted
Fe II 2600	$2.2^{+0.4}_{-0.5}$		
Fe II* 2612	$4.5^{+0.6}_{-0.7}$		

Note: Units are in 10^{12}cm^{-2}. Values have been calculated by numerical integration over bins with width $\Delta v = 10\text{km s}^{-1}$. Note that most of the adopted values are upper or lower limits.

2.4.2 Photoionization Analysis

We use a grid of photoionization models created using the spectral synthesis code Cloudy (version c17.00) [21], in order to find the Hydrogen column density (N_H) and ionization parameter (U_H) that best fit the measured ionic column densities, following the method of previous works [e.g., 77, 79, 82].

We use Cloudy to create a grid of simulated models that correspond to different N_H and U_H values, assuming solar metallicity, and the spectral energy distribution (SED) of quasar HE 0238-1904 (hereafter HE0238) [14]. The N_H and U_H parameters determine the ionic column densities of each model, which we compare with the measured column densities shown in Table 2.2. For S2, including the lower bound of the Fe II column density in the analysis introduced an N_H and U_H solution that was contradictory to the constraints from the other ions. We suspect that this is because the Fe abundance of the system does not match solar metallicity ($Z_\odot$), requiring a metallicity of $\sim 10Z_\odot$. This is in approximate agreement with the highest outflow metallicity found by [115] ($Z \approx 5Z_\odot$). For this reason, we model our solution using the other ions but excluding Fe II. The $\log N_H$ and $\log U_H$ values from this analysis are shown in Table 2.3, as well as in Figure 2.3.

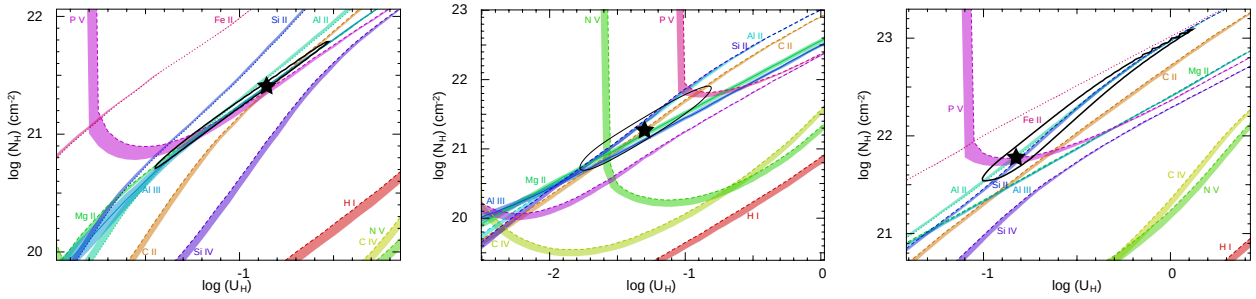

(a) (b) (c)

Figure 2.3 Plots of $\log N_H$ vs. $\log U_H$ for (a) S1, (b) S2, and (c) S3. The colored lines represent the N_H and U_H values allowed by the measured column densities of ions. Solid lines show measurements, dashed lines show lower limits, and dotted lines show upper limits. The colored bands attached to the lines represent the uncertainties in the column density measurements. The black stars in the plots show the solution for N_H and U_H found via χ^2 minimization, and the black ellipses represent the 1σ range for the solutions. For this calculation, the HE0238 SED and solar metallicity are assumed.

2.4.3 Electron Number Density

The electron number density and, by extension, the distance of the outflow systems from the central source, can be found by determining the abundance ratios, measured via column densities, between excited and resonance states of low ionization species [89]. We use the CHIANTI 9.0.1 Database [12, 13] to model the relationship between the ratio of excited and resonance state ion abundances, and the electron number density, based on collisional excitation. We overlay this relation with the ratios based on the measured column densities, as shown in Figure 2.4. For this object, we use the ratios $N(\mathrm{Si\,II^*})/N(\mathrm{Si\,II})$, $N(\mathrm{C\,II^*})/N(\mathrm{C\,II})$, and $N(\mathrm{Fe\,II^*})/N(\mathrm{Fe\,II})$, where $N(ion)$ is the column density of a particular ion.

For S3, we have an upper limit given by the C II ratio, and a measurement from the Si II ratio which agree with one another. Our measurements of Fe II are dominated by noise, and as such, are not included in the n_e measurement. Taking the ratio of N(Si II*)/N(Si II), we find that $\log n_e = 3.3^{+0.8}_{-0.4}$ [cm^{-3}]. S2 provides us a measurement from C II, and upper limits from Si II and Fe II. From the N(C II*)/N(C II) ratio, we find $\log n_e = 0.25^{+0.2}_{-0.2}$ [cm^{-3}]. S1

only gives us a lower limit from C II, as the Si II* is contaminated by an intervening line and cannot give us a reliable ratio between N(Si II*) and N(Si II). Thus, we get a lower limit for the electron number density, $\log n_e > 2.0_{-0.45}$ [cm^{-3}].

2.5 Results

2.5.1 Distance and Kinetic Luminosity of the Outflows

In order to find the distance of the outflow systems, we use the definition for the ionization parameter

$$U_H \equiv \frac{Q_H}{4\pi R^2 n_H c} \tag{2.5}$$

where Q_H is the rate of ionizing photons, R is the distance of the outflow from the central source, and n_H is the hydrogen number density, which is estimated as $n_e \approx 1.2 n_H$ for highly ionized plasma [83]. Since we have a solution for U_H from our photoionization analysis, as well as the n_e for each outflow from the excited to resonance state ratios, we can find R after determining the value of Q_H. We determined Q_H by first scaling the HE0238 SED to match the continuum flux at observed wavelength $\lambda = 6500$ Å from the most recent SDSS observation ($F_\lambda = 1.4^{+0.14}_{-0.14} \times 10^{-16}$ erg s^{-1} cm^{-2} Å^{-1}), and integrating over the scaled SED for energies above 1 Ryd, yielding $Q_H = 1.21^{+0.11}_{-0.11} \times 10^{57}$ s^{-1}. The corresponding $L_{bol} = 1.93^{+0.18}_{-0.18} \times 10^{47}$ erg s^{-1} is larger than what would be expected from calculating the νL_ν at a specific wavelength via the method employed by [116], as the HE0238 SED shows a large peak at the UV range [$\lambda \approx 1000$ Å, 14]. Applying a bolometric correction appropriate to 1700 Å from [117] brings the νL_ν reported by [116] to within 20% of our calculated L_{bol}. The resulting outflow distances are shown in Table 2.3. Note that the distance of S2 (–1800 km s^{-1}, $R = 67^{+55}_{-31}$ kpc) is at least an order of magnitude larger than that of S3 (–3500 km

s^{-1}, $R = 1.2^{+0.8}_{-0.9}$ kpc) or S1 (–1200 km s^{-1}, $R < 5.4^{+7.3}$ kpc).

Once we have the distance of the outflow, we can find the mass flow rate [118]

$$\dot{M} \simeq 4\pi\Omega R N_H \mu m_p v \tag{2.6}$$

and the kinetic luminosity

$$\dot{E}_k \simeq \frac{1}{2}\dot{M}v^2 \tag{2.7}$$

assuming a partially filled shell, where Ω is the global covering factor (fraction of the total solid angle of the quasar that the outflow covers), $\mu = 1.4$ is the mean atomic mass per proton, m_p is the proton mass, and v is outflow velocity. For the global covering factor, we assume $\Omega = 0.2$, the portion of quasars from which C IV BALs are found [37]. As explained by [71], this is a reasonable assumption despite the relative rarity of quasars showing singly ionized absorption troughs such as Si II, due to the likelihood that such quasars are regular BAL quasars seen from specific lines of sight. The resulting kinetic luminosity calculations yield $\log \dot{E}_K[\mathrm{erg\ s^{-1}}] = 45.42^{+1.33}_{-0.64}, 45.82^{+0.37}_{-0.32}$ for S3 and S2 respectively, as well as an upper limit of $\log \dot{E}_K < 44.33^{+0.53}$ for S1. In addition, we calculate the momentum flux ($\dot{M}v$) of each outflow system (see Table 2.3) and compare it to the single-scattering limit of the quasar ($\frac{L_{bol}}{c} = 6.44^{+0.61}_{-0.61} \times 10^{36}$ erg $\mathrm{cm^{-1}}$). The single-scattering limit assumes the scenario in which absorption of photon momentum drives acceleration [119, 120]. The momentum flux of S1 is smaller than the single-scattering limit, while those of S2 and S3 are above the limit. As S2 has a momentum flux an order of magnitude higher than the single-scattering limit, this implies the possibility of a multiple-scattering scenario [121].

2.5.2 Changes in the High Velocity BAL Trough (S4)

Following up on the results reported by [98], we examine the velocity shift of the C IV BAL of S4. Using two Gaussian profiles, one broad and shallow, and the other narrow and deep, we modeled the absorption in each of the five epochs, as shown in Figure 2.5. We can see that the centroid velocity of the narrow Gaussian monotonically grows, while the equivalent width becomes smaller from epoch to epoch. Detailed information on the centroid velocities and equivalent widths per epoch can be seen in Table 2.4.

Assuming acceleration along the line of sight, based on the centroid velocities of the narrow Gaussian, the average acceleration between the observations in September 2001 and January 2017 would be $a = -0.25 \pm 0.13$ cm s^{-2} in the quasar's rest frame, which agrees within error with the acceleration $a = -0.154 \pm 0.025$ cm s^{-2} between September 2001 and September 2005 found by [98]. Due to the shrinking of the trough, we must take into consideration effects other than line of sight acceleration, such as changes in photoionization, as discussed by [122].

2.6 Discussion

2.6.1 AGN Feedback Contribution of Outflows

As previously mentioned in the introduction, the kinetic luminosity ($\dot{E}_k$) of the outflow systems must be at least $\sim 0.5\%$ [58] or $\sim 5\%$ [53] of the source quasar's Eddington luminosity (L_{Edd}) to contribute to AGN feedback. In order to find this ratio, we must first find the Eddington luminosity. We compute the mass of the black hole using the Mg II-based mass equation in [123], with the FWHM of the Mg II emission feature in the SDSS spectrum. To

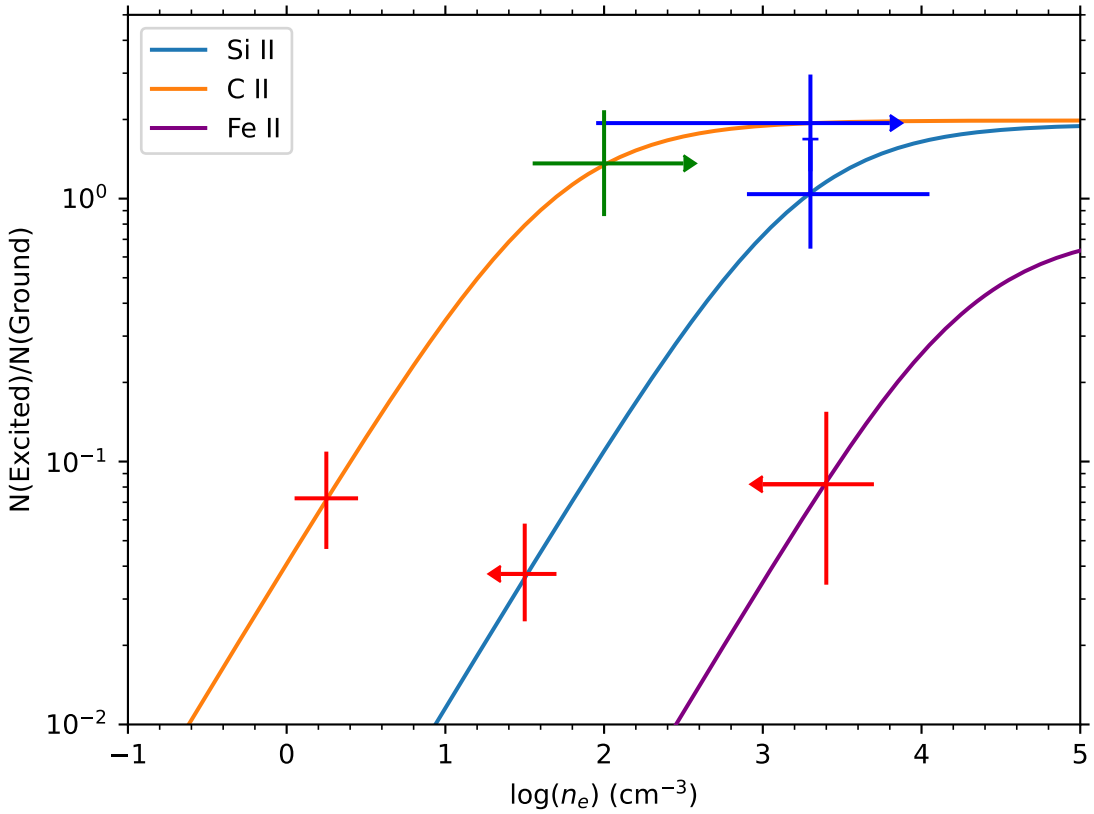

Figure 2.4 Ratio between excited and resonance state abundances of Si II, C II, and Fe II vs. $\log n_e$. The curves marked Si II, C II, and Fe II are the theoretical ratios modeled with CHIANTI, assuming a temperature of 10,000 K. The crosses on the curves show the ranges of the C II, Si II, and Fe II column density ratios, based on the measured AOD column densities. The green, red, and blue correspond to systems S1, S2, and S3 respectively. Arrows indicate either upper or lower limits in $\log n_e$ depending on the direction of the arrow. The upper limit of the N(Si II*)/N(Si II) ratio for S3 is marked with a tick, as it overlaps with the error bars of the C II ratio of the same system.

Table 2.3 Physical Properties J0242+0049 Outflow Systems

Outflow System	S1 = -1200 km s^{-1}	S2 = -1800 km s^{-1}	S3 = -3500 km s^{-1}
$log(N_{\rm H})$ [cm^{-2}]	$21.41^{+0.38}_{-0.70}$	$21.27^{+0.64}_{-0.58}$	$21.78^{+1.30}_{-0.24}$
$log(U_{\rm H})$ [dex]	$-0.86^{+0.33}_{-0.59}$	$-1.30^{+0.49}_{-0.48}$	$-0.83^{+0.95}_{-0.18}$
$log(n_{\rm e})$ [cm^{-3}]	$> 2.00_{-0.45}$	$0.25^{+0.20}_{-0.20}$	$3.30^{+0.75}_{-0.40}$
Distance [kpc]	$< 5.4^{+7.3}$	67^{+55}_{-31}	$1.2^{+0.8}_{-0.9}$
$\dot{M}$ [$M_{\odot}$yr^{-1}]	$< 480^{+300}$	6500^{+8900}_{-3400}	700^{+2900}_{-30}
$\dot{M}v$ [10^{36} erg cm^{-1}]	$< 3.6^{+2.3}$	74^{+100}_{-39}	$16^{+60}_{-0.7}$
$log(\dot{E}_K)$ [erg s^{-1}]	$< 44.33^{+0.21}$	$45.82^{+0.37}_{-0.32}$	$45.43^{+0.7}_{-0.02}$
$\dot{E}_K/L_{edd}$ [%]	$< 0.18^{+0.16}$	$5.5^{+8.8}_{-3.1}$	$2.3^{+9.9}_{-0.8}$

Note: Temperature of 10,000K assumed.

Table 2.4 Velocities of C IV BAL at Each Epoch

MJD	Date	Δt_{Rest} (days)	v_n (km s^{-1})	Δv_n (km s^{-1})	EW_n (km s^{-1})	v_w (km s^{-1})	Δv_w (km s^{-1})	EW_w (km s^{-1})
52177	Sep. 25, 2001	0	$-17,460 \pm 50$	0	1190	$-19,000$	0	1010
52199	Oct. 17, 2001	13.0	$-17,600 \pm 40$	-140 ± 70	1320	$-19,000$	0	2140
53619	Sep. 5, 2005	838.6	$-17,720 \pm 4$	-260 ± 50	920	$-20,000$	-1000	20
55455	Sep. 16, 2010	1922.8	$-17,870 \pm 40$	-400 ± 60	460	$-19,490$	-490	860
57758	Jan. 5, 2017	3282.7	$-18,180 \pm 380$	-720 ± 380	80	$-19,000$	0	260

Note: Table of the centroid velocity and equivalent width of the C IV BAL for each epoch. Δt_{Rest} is the elapsed time in the quasar's rest frame since the 52177 epoch. v_n and v_w are the centroid velocities of the narrow and wide best fit Gaussians in the quasar's rest frame, while Δv_n and Δv_w are the velocity shifts compared to that of the 52177 epoch. The equivalent widths (EW_n, EW_w) have been calculated by integrating over the Gaussians in velocity space. The parameters for the wider Gaussians are more affected by the continuum models for each epoch. Note that the uncertainty in the centroid velocity of the MJD=53619 epoch is significantly smaller than those of the other epochs, due to the higher S/N ratio and resolution of the data.

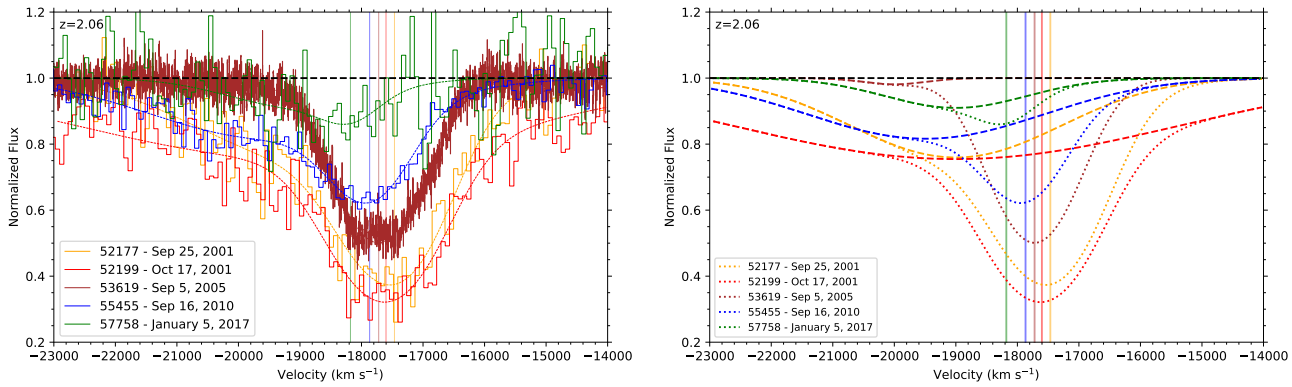

(a) (b)

Figure 2.5 Normalized flux vs. velocity of the S4 C IV BAL at different epochs. The trough has been modeled by employing a best fit of a profile of two Gaussians, one wide and one narrow. (a) shows Gaussian models of the troughs over the data, while (b) shows the Gaussian models independently. The colored vertical lines mark the centroid velocities at each epoch. Note that the centroid velocity increases through each epoch, while the EW decreases.

account for the Fe II emission throughout the spectrum, we use the Fe II template by [124], and run a best fit algorithm to match the features in the spectrum, as done by [125]. This yields a black hole mass of $M_{BH} = 9.7^{+4.9}_{-3.4} \times 10^8 M_\odot$, corresponding to an Eddington luminosity of $L_{Edd} = 1.2^{+0.6}_{-0.4} \times 10^{47}$erg s^{-1}. We expect the Fe II emission's effect on the absorption to be small, as the fitted emission template from [124] is $< 20\%$ of the continuum level of the SDSS spectrum of MJD=57758, leaving us with column densities that agree with our measured values within error.

Taking the ratio between the kinetic luminosity of each outflow system and the Eddington luminosity of the quasar, we find that S2 and S3 are well above the 0.5% threshold from [58], and S2 is above the 5% threshold by [53], while S1's kinetic luminosity is below 0.18 % of the Eddington luminosity, as seen in Table 2.3. We can thus conclude that S2 and S3 are energetic enough to contribute to AGN feedback.

Unlike in objects analyzed in other papers [e.g. 82, 86], we do not have lines from the very high ionization phase. Thus, while there may be a very high ionization phase, we cannot tell

from the information we have.

2.6.2 Time Variability of Troughs

Following the examination of the S4 C IV BAL at different epochs, we looked to systems S1, S2, and S3 for time variability. As shown in Figure 2.6, the Si IV trough depth becomes increasingly shallower over time, which may be explained by the same ionization effects that affect the S4 C IV BAL shown in Figure 2.5, discussed by [122]. As the ionization parameter U_H changes, ions of particular ionization states become more or less abundant over time. Since the C IV of S4, along with Si IV of S1, S2, and S3, decrease monotonically, this supports the assertion that the changes in the troughs are due to changes in the ionization parameter. Further observation and analysis will be required to confirm these effects.

2.6.3 SED and Metallitic Dependency, and Attenuation of the SED

An alternative to using the SED of HE 0238-1904 would be to use the theoretical SED as defined by [126], which is based on the He II line. The HE 0238-1904 SED is based on observation of a high quality spectrum which stretches into the far UV range, better representing a quasar spectrum [14]. Just like in other objects[e.g. 7, 82], higher metallicity drops the values of the energetics parameters. For instance, raising the metallicity to 4 times solar metallicity, using abundance ratios from [11], changes the photoionization solution of S2 to $\log U_H = -1.5^{+0.3}_{-0.3}$, and $\log N_H = 20.5^{+0.4}_{-0.4}[\mathrm{cm}^{-2}]$, lowering the mass flow rate and kinetic luminosity to $\dot{M} = 1300^{+600}_{-400} M_\odot \mathrm{yr}^{-1}$ and $\log \dot{E}_K = 45.13^{+0.17}_{-0.18}[\mathrm{erg\ s}^{-1}]$ respectively. Using the SED by [126] with solar metallicity changes the solution to $\log U_H = -1.5^{+0.4}_{-0.4}, \log N_H = 21.2^{+0.5}_{-0.5}$, which is in agreement with the values in Table 2.3 within error.

It is possible that the SED seen by one outflow system can be attenuated by another, resulting in a smaller Q_H, and by extension, a smaller distance R. In particular, as S2 is further out than the other mini-BAL system S3, it is likely that the SED seen by S2 is obscured by S3 [e.g., 3, 79, 127, 128]. We used the method described by [79] to test the effects of attenuation by S3. We used Cloudy to model the attenuated SED by S3 by inputting the relevant N_H and U_H values of S3 shown in Table 2.3. We then use that attenuated SED to find the resulting Q_H and R of S2. The reduced values for the parameters are $Q_H = 4.9^{+0.5}_{-0.5} \times 10^{56}$ s^{-1} and $R = 43^{+35}_{-20}$ kpc, which is a $\sim 30\%$ decrease in the distance of S2. We choose S3 as the attenuation source, as its stronger features compared to S1 suggest that the attenuation effect from S3 would be larger than that of S1. We are unable to calculate the attenuation by S4, as we cannot obtain N_H or U_H from its singular C IV absorption trough.

2.6.4 Comparison With Other Outflows

There have been several prior studies of quasar outflow acceleration, including that of the acceleration of the outflow of quasar SDSS J1042+1646 conducted by [122], based on the acceleration seen in the Ne VIII $\lambda\lambda 770, 780$. The bolometric luminosity of SDSS J1042+1646 is estimated at $\sim 1.5 \times 10^{47}$ erg s^{-1}, which is comparable to that of J0242+0049 (1.9×10^{47} erg s^{-1}). The average acceleration of S4 that we have found ($a \approx -0.25$ cm s^{-2}) is roughly an order of magnitude smaller than that by [122] ($a = -1.52$ cm s^{-2}), which suggests that if S4 is truly accelerating, the acceleration of quasar outflows can cover a wide range.

To give context to the study of outflow S2, we review a few outflows with similarly large R and/or $\dot{E}_K$. Analysis of a molecular outflow of quasar SDSS J1148+5251 at a distance $R \sim 15$ kpc conducted by [129] revealed a lower limit to the mass flow rate of $\dot{M} > 3500 M_\odot$ yr^{-1} as well as one for the kinetic luminosity $\dot{E}_K > 1.9 \times 10^{45}$ erg s^{-1}.

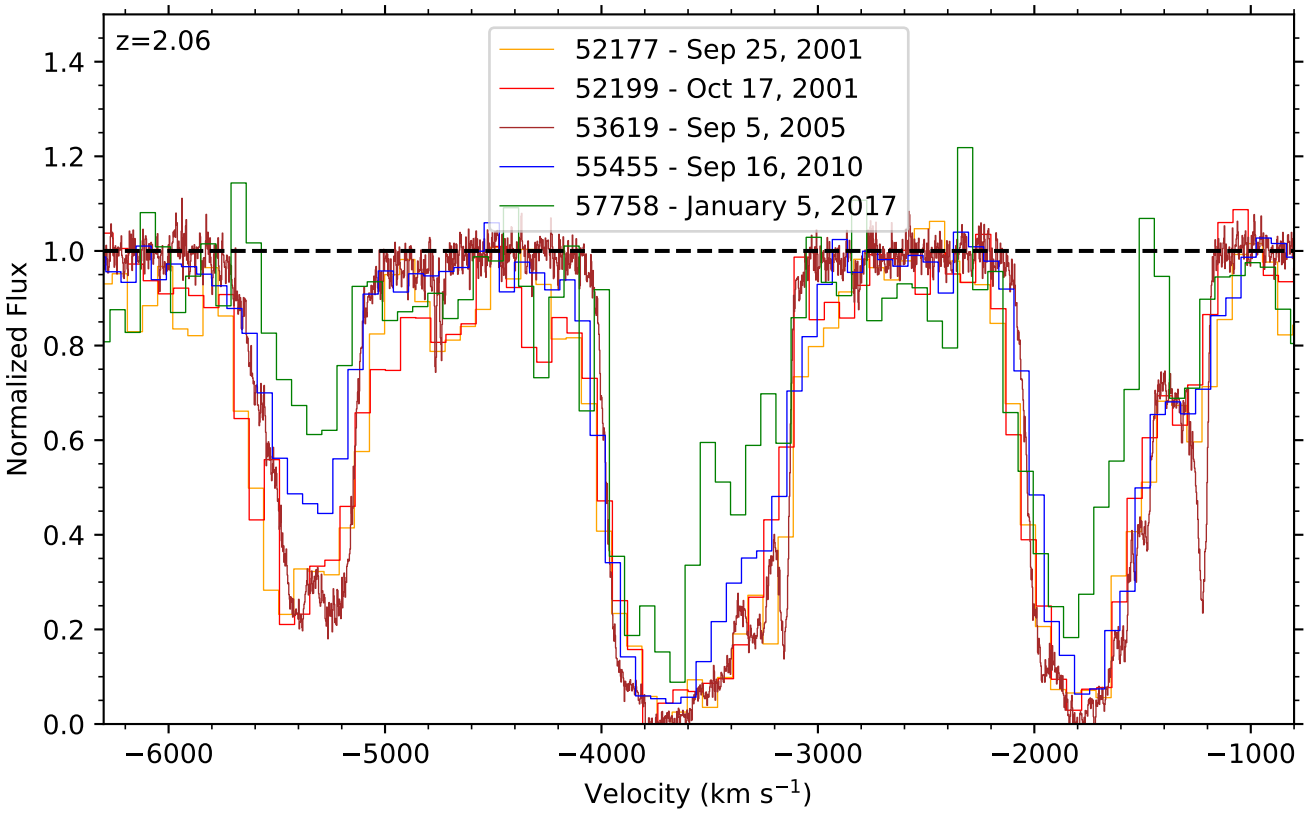

Figure 2.6 Normalized flux vs. velocity of Si IV troughs at different epochs. Note that the depth of the troughs becomes shallower over time.

[87] analyzed the ionized gas around 11 radio-quiet quasars via the [O III] λ5007Å emission. These outflows were found between $\sim 10 - 20$ kpc from the central source, had velocities of up to –1000 km s^{-1}, and had an estimated $n_e \sim 1.2$ cm^{-3}. The outflows had an estimated range of $\dot{E}_K$ from 4×10^{44} to 3×10^{45} erg s^{-1}, and $\dot{M}$ from 2×10^3 to $2 \times 10^4 M_\odot$ yr^{-1}. These numbers are within a factor of few of the values we find for S1, S2, and S3 (see Table 2.3), which suggests we may find similar outflows in absorption.

In their analysis of SDSS J1051+1247, [82] found an outflow system with $\dot{E}_K = 3 \times 10^{45}$ erg s^{-1}. The mass flow rate ($\dot{M} = 6500 M_\odot$ yr^{-1}) and kinetic luminosity ($\dot{E}_K = 6.6 \times 10^{45}$ erg s^{-1}) of S2 align with these values, and those of the objects mentioned above, within margin of error. [86] claim the most energetic quasar outflow measurement to date from quasar SDSS J1042+1646 ($\dot{E}_K = 5 \times 10^{46}$ erg s^{-1}), and this claim remains uncontested.

While the distance of S2 from the quasar is unprecedentedly large, there exists a theoretical model that may be supported by this observation. [48] provide an argument that FeLoBALs, absorption systems with signs of Fe II, may be formed in situ at distances of several kpc. They clarify that while their model focuses on the formation of FeLoBALs at large distances, other classes of outflows may form as described by it.

2.7 Summary and Conclusion

This paper has presented the analysis of three absorption systems of quasar SDSS J0242+0049, dubbed S1, S2, and S3, from VLT/UVES observational data, as well as the velocity shift of the S4 C IV BAL across five different epochs. From the absorption troughs we identified, we measured the column densities of 11 ions in each system as shown in Table 2.2. Through photoionization analysis using the measured column densities, we found the best fit solutions to U_H and N_H for each system.

The abundance ratios between the excited and resonance states of ions Si II and C II were used to find the electron number density n_e of the three systems S1, S2, and S3, as shown in Figure 2.4. Equations 2.5, 2.6, and 2.7 used to find the distance from the central source, the mass flow rate, and the kinetic luminosity of each system respectively. The ratios between the kinetic luminosities and the quasar's Eddington luminosity were found in order to evaluate their AGN feedback contribution, the results of which can be seen in Table 2.3. From this analysis, we have found that S2 and S3 have sufficient kinetic luminosity for AGN feedback contribution. Most notable in this result is the distance of S2 $R = 67$ kpc, further than the absorption system of 3C 191 found at R= 28 kpc by [95], making this the furthest reported distance of a mini-BAL absorption outflow from its central source.

Following the analysis of the three systems, we examined the change in velocity and equivalent width of the S4 C IV BAL, as shown in Figure 2.5, based on the UVES spectrum, as well as different SDSS observations. As seen in Table 2.4, there has been a monotonic increase in the line of sight velocity, as well as a decrease in equivalent width, with the trough being a factor of six weaker at the epoch of January 2017 compared to that of September 2001.

Through further observation and analysis, we expect to shed more light on the time variability of the S4 C IV BAL, as well as that of systems S1, S2, and S3.

Acknowledgments

NA and DB acknowledge support from NSF grant AST 2106249, as well as NASA STScI grants GO 14777, 14242, 14054, 14176, and AR-15786. DB acknowledges support from the Virginia Space Grant Consortium Graduate Research Fellowship Program.

Chapter 3

VLT/UVES Observation of the SDSS J2357-0048 Outflow

Foreword

This chapter is based on the published paper "*VLT/UVES Observation of the SDSS J2357-0048 Outflow*" [18]. I led the project by analyzing the data, doing calculations, creating the figures, and writing the paper.

3.1 Abstract

We found a broad absorption line (BAL) outflow in the VLT/UVES spectrum of the quasar SDSS J235702.54-004824.0, in which we identified four subcomponents. We measured the column densities of the ions in one of the subcomponents ($v = -1600$ km s^{-1}), which include O I and Fe II. We found the kinetic luminosity of this component to be at most $\sim 2.4\%$ of the quasar's Eddington luminosity. This is near the amount required to contribute to AGN feedback. We also examined the time-variability of a C IV mini-BAL found at $v = -8700$ km s^{-1}, which shows a shallower and narrower absorption feature attached to it in previous SDSS observations from 2000 and 2001, but not in the spectra from 2005 and

onwards.

3.2 Introduction

Quasar outflows are often seen as absorption troughs blueshifted relative to the quasar rest frame in $\lesssim 40\%$ of quasar spectra [37, 38, 88], often invoked as likely producers of AGN feedback [e.g., 34–36, 53, 130]. Theoretical estimates require these outflows to have a kinetic luminosity ($\dot{E}_k$) of $\sim 0.5\%$ [58] or $\sim 5\%$ [53] of the quasar Eddington luminosity (L_{Edd}) to significantly contribute to AGN feedback. We have reason to interpret the luminosity mentioned by [58] and [53] to be L_{Edd} and not the bolometric luminosity (L_{Bol}), as explained in Section 4 of [2]. Outflows satisfying these conditions have been found in previous studies [e.g., 9, 14, 16, 17, 77, 82, 86, 89–91, 131].

An outflow's kinetic luminosity depends on its distance from the quasar (R). One way to estimate this distance is by measuring the ionization parameter (U_H) and electron number density (n_e) [e.g., 92]. Several studies in the past have employed this method to find the distance of outflow systems [e.g., 2, 7, 9, 17, 82, 92–96]. The value of n_e can be determined by finding the ratio between the column densities of energy states of the same ion [e.g., 97].

This paper presents the determination of the R and n_e values, along with $\dot{E}_k$, of an outflow system found in the VLT/UVES spectrum of SDSS J235702.54-004824.0 (hereafter J2357-0048). The analysis in this paper has been conducted with data from the VLT/UVES Spectral Quasar Absorption Database (SQUAD) published by [10], from which data has been retrieved for a similar analysis of quasar outflows [17].

The UVES data of J2357-0048 is from program 075.B-0190(A), and has been added to SQUAD by [10] and examined by [103] for mini-BAL systems. [103] report the presence of

four absorption systems, which we independently identified as four sub-components of a BAL outflow. We found the lowest velocity system suitable for our analysis, as it shows troughs of excited states of Fe II, O I, and Si II. We also found a high velocity C IV mini-BAL, of which we report the time variability in comparison with SDSS spectra from different epochs.

This paper is structured as follows. Section 3.3 discusses the observation and data acquisition of J2357-0048. Section 3.4 shows the ionic column density measurements and the n_e and U_H. In Section 3.5, we present the analysis results and the energetics parameters. We also show the time variability analysis of the high velocity mini-BAL. In Section 3.6, we discuss the results and other features of the quasar's spectrum, and Section 3.7 summarizes and concludes the paper. For this analysis, we adopted a cosmology of $h = 0.696$, $\Omega_m = 0.286$, and $\Omega_\Lambda = 0.714$ [99], and used the Python astronomy package Astropy [100, 101] for cosmological calculations.

3.3 Observation and Data Acquisition

The quasar J2357-0048 (J2000: RA=23:57:02.54, DEC=-00:48:24.0; $z = 2.998$) was observed with the VLT/UVES on September 5, 2005 as part of the program 075.B-0190(A), with resolution $R \simeq 40,000$ and wavelength coverage from 3621 to 10429 Å [10].

[10] report a systemic redshift of $z = 2.998$, also reporting values of $z = 2.998$, $z = 3.012$, $z = 3.005$ from the SDSS, NED, and SIMBAD databases respectively. We found a discrepancy between these values and the redshifts that we found from the databases independently. From the SDSS data, we found redshifts ranging from $z = 3.006$ [ninth data release 132] to $z = 3.062$ [13th data release 133]. NED reports $z = 3.063$ citing the 13th SDSS data release, while in SIMBAD we found $z = 3.006$ from the ninth data release. While the literature reports a wide range of redshifts, we found that the systemic redshift $z = 2.998$ reported by

[10] is consistent with the C IV emission redshift $z = 2.97$, blueshifted relative to the systemic redshift, that we found based on the emission from the SDSS spectrum. We have also found a redshift of $z = 2.99$ with the C III] emission complex, consistent with the adopted redshift of $z = 2.998$.

[10] reduced and normalized the UVES data by its continuum and emission as part of the SQUAD database. In Fig. 3.1, we show the normalized spectrum multiplied by the emission model, scaled to match the continuum level at observed wavelength $\lambda = 6500$ Å of the SDSS spectrum at the epoch of MJD=25503. [134] report the detection of a damped Ly α (DLA) system at $z = 2.479$, and [103] have identified four outflow absorption systems, which we identify here as four subcomponents of a BAL outflow (S1 at $v = -1600$ km s^{-1}, S2 at $v = -2300$ km s^{-1}, S3 at $v = -2700$ km s^{-1}, and S4 at $v = -3100$ km s^{-1}). We also identified a high velocity C IV mini-BAL at $z = 2.8849$, which we call S5 in this paper.

The outflows show absorption of low ionization species such as Si II, Fe II, and O I, and others including S IV, C IV, Si IV, H I, and Al III. The focus of this paper's analysis is on S1, as it displays troughs of excited states of Si II, Fe II, and O I, which allowed us to find its n_e, and by extension, R. We converted the normalized spectrum from wavelength space to velocity space using the quasar's systemic redshift, as shown in the plots of Figs. 3.2 and 3.3.

For our time variability analysis, we have retrieved SDSS spectra from MJD=51791, 52203, 55477, 56956, and 57688. We corrected the spectra for galactic reddening and extinction with $E(B - V) = 0.0253$ [104] and the extinction model by [135]. The SDSS spectra have resolutions of $R \approx 2000$. More details on the SDSS spectra are in Table 3.1.

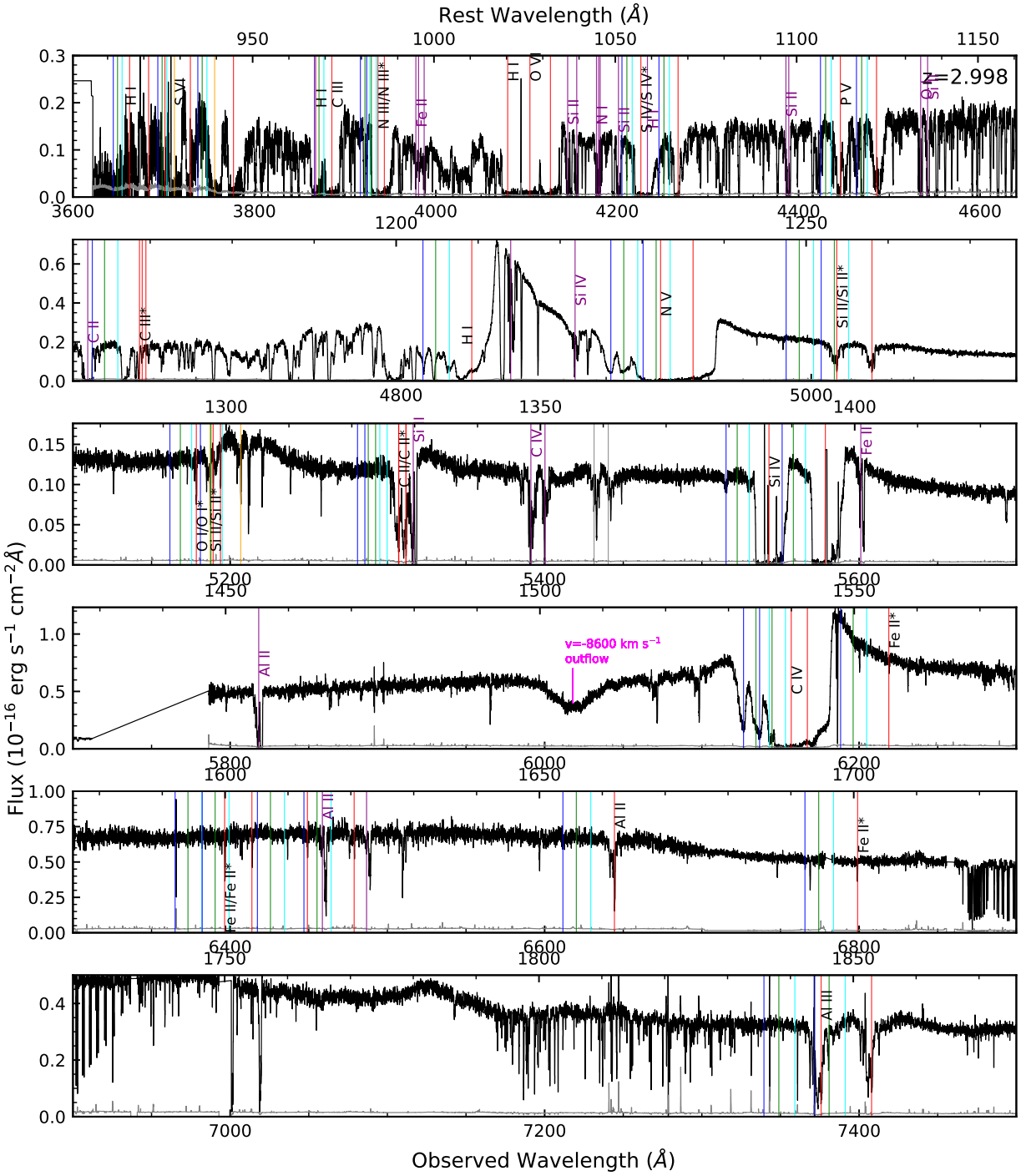

Figure 3.1 Normalized flux of J2357-0048 multiplied by the emission model by [10], based on the SQUAD data set. The flux has been scaled to match the BOSS spectrum from the epoch of MJD=52203 (Oct. 21, 2001) at observed wavelength $\lambda = 6500$ Å. The black curve represents the flux, and the gray shows the error in flux. The red, cyan, green, and blue vertical lines mark absorption troughs of outflow systems S1, S2, S3, and S4 respectively, while the S5 C IV mini-BAL is labeled in magenta. Absorption features of the DLA system are marked in dark purple, and other intervening features are marked in grey. The Si II $\lambda\lambda$1304 multiplet of S1 is marked in orange to avoid confusion with the O I multiplet troughs. The S VI doublet of S1 is also marked in orange to avoid confusion with the H I lines. We also marked where the absorption of the C III* multiplet near rest wavelength 1175Å would be found. Note that we cannot positively identify C III* due to the Lyman-α contamination.

Table 3.1 SDSS Spectra Information

MJD	Spectrograph	Plate	Fiber	Observed Date	Coverage (Å)
51791	SDSS	387	246	Sep. 4, 2000	3824–9215
52203	SDSS	685	317	Oct. 21, 2001	3820–9202
55477	BOSS	4216	410	Oct. 10, 2010	3565–10325
56956	BOSS	7850	555	Oct. 26, 2014	3604–10394
57688	BOSS	9208	969	Oct. 27, 2016	3608–10334

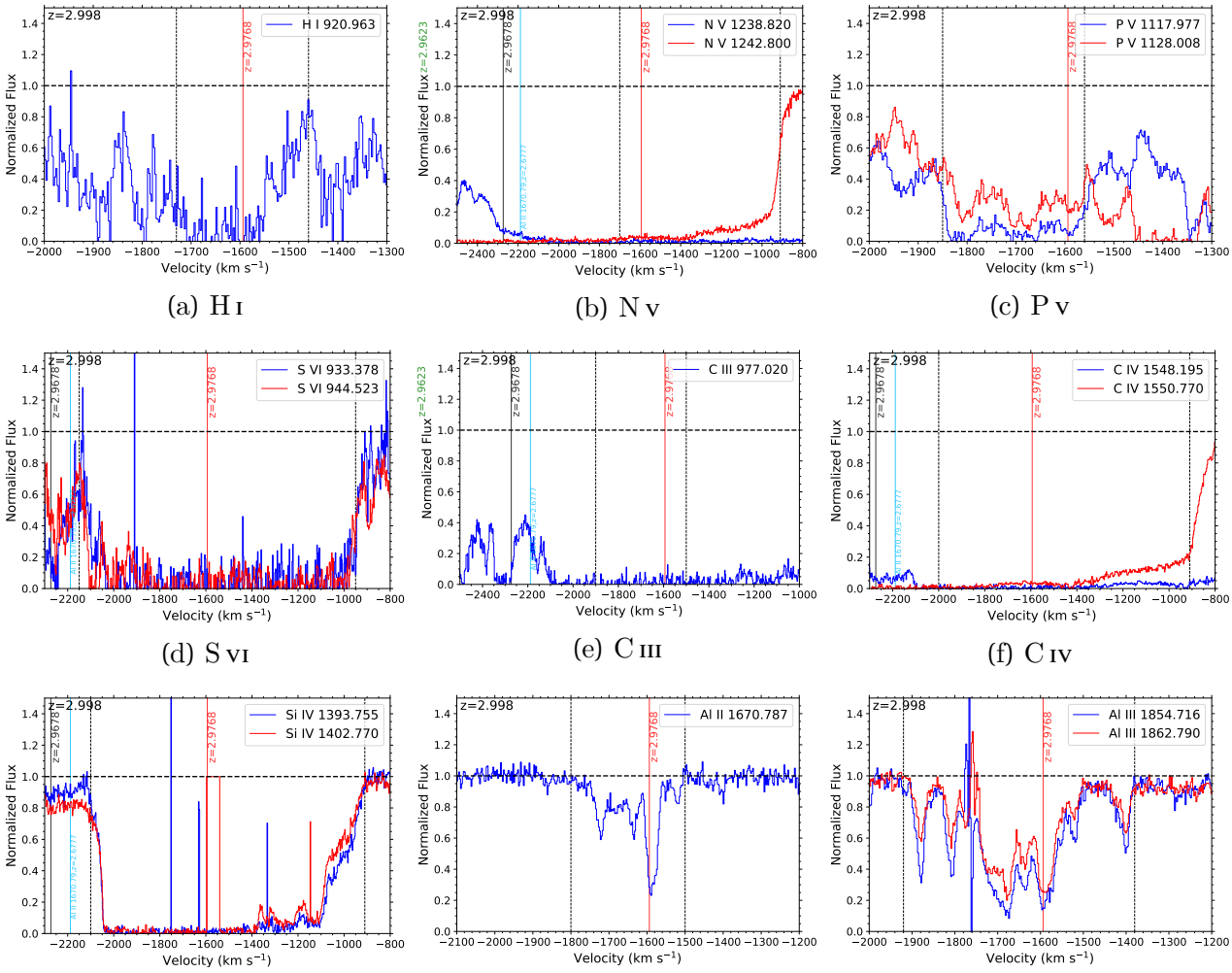

(a) H I (b) N V (c) P V

(d) S VI (e) C III (f) C IV

(g) Si IV (h) Al II (i) Al III

Figure 3.2 Normalized spectra plotted in velocity space for ions in S1. The velocities of S1 ($z = 2.9768$) and S2 ($z = 2.9678$) are marked with red and black vertical lines respectively. The dotted vertical lines show the integration ranges used for column density calculations, while the horizontal dashed line marks the continuum level. The light blue vertical lines mark the intervening absorption systems that contaminate the blue spectra.

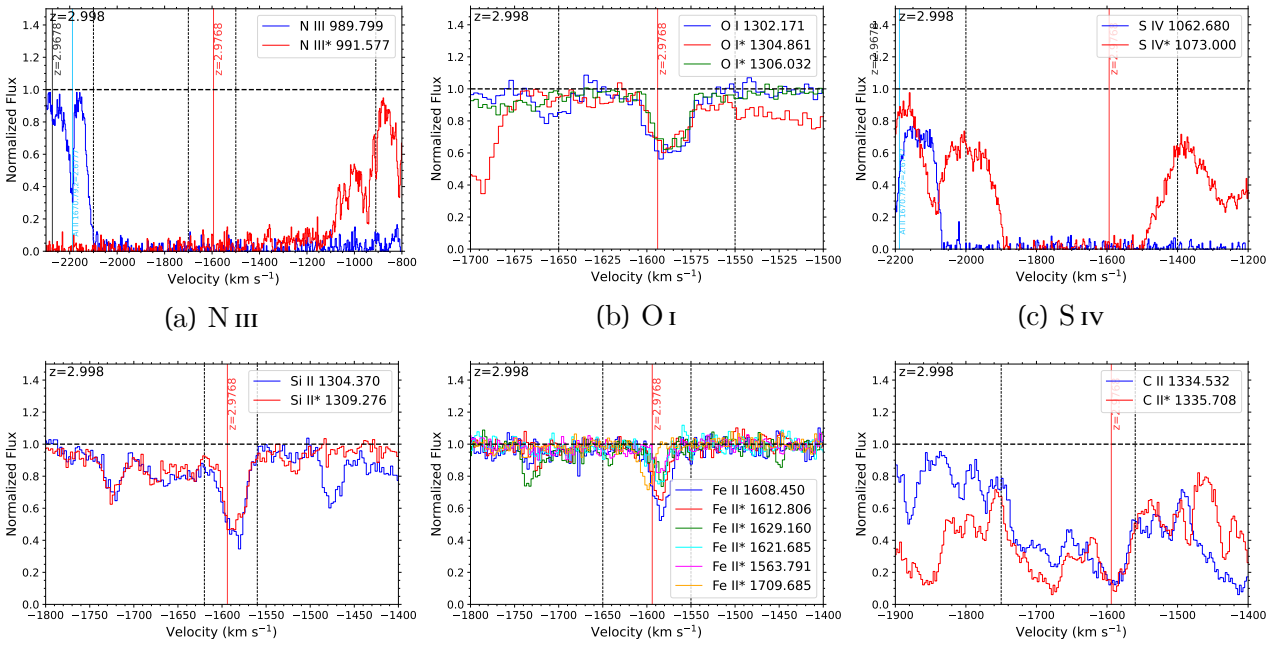

(a) N III (b) O I (c) S IV

(d) Si II (e) Fe II (f) C II

Figure 3.3 Normalized spectra plotted in velocity space for ions in S1 that display excited states. The format of the plots are the same as in Fig. 3.2.

3.4 Analysis

3.4.1 Ionic Column Density

We found the ionic column densities (N_{ion}) of S1 as our first step in finding the physical characteristics of the outflow. We employed two different methods in measuring the column densities: assuming the apparent optical depth (AOD) of a uniform outflow covering a homogeneous source [107]; and the partial covering (PC) method assuming a partially covered source [108–110].

While the AOD method is convenient in its simplicity, the PC method can provide us with more accurate measurements of ions with doublets of transition lines, taking into account effects such as non-black saturation [e.g., 113, 118]. This is done by finding a velocity

dependent covering factor for each ion [111, 112]. A more detailed description of these methods can be found in [17] Section 3.1, which used the same methods to analyze the UVES spectrum of the quasar J024221.87+004912.6. We also used an inhomogeneous power law (PL) covering factor for the P V and Al III doublets to improve column density measurements, as done in previous work [e.g., 7, 111, 118]. We incorporated the difference between the PL and PC values as the lower or upper errors for the adopted column density, depending on whether the PL result was smaller or larger than that from the PC method.

For each ion, we chose an integration range covering a visible absorption feature (see Figs. 3.2, 3.3). Some ions, such as N V and C IV, exhibit blending between the red and blue troughs of their doublets (see plots b and f of Fig. 3.2). To minimize the effects of blending, we selected an integration range that avoids an overlap of the red and blue features, and in this paper report a lower limit of the column density based on the AOD assumption. While we show both ground and excited state troughs of S IV in Fig. 3.3, since S IV λ1062 is contaminated by the damped Lyman-α trough, we only measured the column density of S IV* λ1073 and thus report a lower limit. While C II absorption is visibly present as seen in Fig. 3.1, the blending between the excited and resonance troughs, as well as contamination from intervening absorption, made it difficult to isolate the troughs. As such, while we computed a lower limit of the total column density of C II, we have excluded it from the electron number density calculation in Subsection 3.4.3.

The column density measurements are shown in Table 3.2. Note that the high column density of H I comes from a measurement based on the Lyman 9 line, which has a wavelength of $\lambda = 920.963$ Å (see plot a of Fig. 3.2). The errors in column density have been propagated from the error in normalized flux, binned in $\Delta v = 10\text{km s}^{-1}$ wide bins. A conservative 20% error has been added in quadrature to the adopted values used for photoionization analysis to take into account the uncertainty in the modeled continuum [7]. Note that most

of the adopted values are lower limits, as we have used the AOD method for most of the ions in the system. We also took AOD measurements of the visible absorption features of S2–S5. The lower limits of H I column densities of S2–S4, measured from the Lyman-α lines, range between $\sim 400 - 500 \times 10^{12}$ cm^{-2}, which is several orders of magnitude smaller than the measured H I column density of S1. The C IV of S5 has a lower limit of $N(\mathrm{C\,IV}) > 520 \times 10^{12}$ cm^{-2}.

Table 3.2 J2357-0048 column densities from UVES observations

Troughs	Wavelength(Å)	AOD	PC	PL	Adopted	$Z_\odot$-1	$Z_\odot$-2	4.68$Z_\odot$-1	4.68$Z_\odot$-2
			S1, $v = -1600$ km s^{-1}						
H I	920.963	$141,700^{+18400}_{-7700}$			$141,700^{+29,400}_{-33,800}$	16.4	3.50	8.0	2.92
N III total		$14,390^{+830}_{-140}$			$> 14,390_{-2040}$	10.0	1.74	23.87	10.45
N III 0	989.799	7220^{+700}_{-110}							
N III* 174	991.577	7270^{+450}_{-90}							
N V	1238.820 & 1242.800	8640^{+30}_{-30}			$> 8640_{-1730}$	1.85	10.41	0.62	2.92
O I total		260^{+7}_{-7}			$> 260_{-30}$	0.03	0.75	0.20	0.85
O I 0	1302.171	100^{+4}_{-4}							
O I* 158	1304.861	90^{+4}_{-4}							
O I* 227	1306.032	70^{+4}_{-4}							
P V	1117.977 & 1128.008	677^{+7}_{-6}	740^{+10}_{-10}	510^{+60}_{-10}	510^{+230}_{-100}	0.37	1.10	0.17	0.32
S IV*	1073.000	$14,330^{+1710}_{-180}$			$> 14,330_{-2870}$	2.67	1.65	3.75	3.44
S VI	933.378 & 944.523	6870^{+360}_{-120}			$> 6870_{-1380}$	0.66	1.85	0.39	1.16
C II total		1100^{+10}_{-10}			$> 1100_{-220}$	5.27	1.48	11.66	3.18
C II 0	1334.532	490^{+5}_{-5}							
C II* 63	1335.708	610^{+6}_{-6}							
C III	977.020	790^{+100}_{-10}			$> 790_{-160}$	815	173	498	293
C IV	1548.195 & 1550.770	8770^{+530}_{-20}			$> 8770_{-1750}$	60.1	115	7.01	12.39
Si II total		230^{+4}_{-4}			$> 230_{-50}$	4.46	1.03	128	21.04
Si II 0	1304.370	120^{+3}_{-3}							
Si II* 287	1309.276	110^{+3}_{-2}							
Si IV	1393.755 & 1402.770	3320^{+260}_{-20}			$> 3320_{-660}$	18.0	3.75	43.2	41.29
Al II	1670.787	$10^{+0.2}_{-0.2}$			$> 10_{-2}$	8.3	2.0	51.2	6.16
Al III	1854.716 & 1862.790	$163^{+1.4}_{-1.4}$	218^{+57}_{-3}	391^{+76}_{-3}	390^{+110}_{-170}	1.97	0.22	5.46	2.37
Fe II total		260^{+10}_{-10}			$> 260_{-50}$	0.01	0.44	0.40	1.27
Fe II 0	1608.450	60^{+3}_{-3}							
Fe II* 385	1621.685	40^{+5}_{-4}							
Fe II* 668	1629.160	36^{+5}_{-4}							
Fe II* 1873	1612.806	70^{+6}_{-5}							
Fe II* 2430	1563.791	17^{+2}_{-2}							
Fe II* 13474	1709.685	35^{+3}_{-2}							

Note. — Column densities have been calculated via numerical integration over $\Delta v = 10$km s^{-1} bins. Energy states of ions are noted with energies in units of cm^{-1}. The wavelengths listed for each ion are the transition rest wavelengths in Å. Most of the adopted values are lower limits due to being AOD measurements. The four rightmost columns show the ratios between modeled and adopted column densities, for the solar one-phase, solar two-phase, supersolar one-phase, and supersolar two-phase solutions, respectively. Units of column density are in 10^{12}cm^{-2}.

3.4.2 Photoionization Analysis

We followed the method of previous works to find the ionization parameter (U_H) and the Hydrogen number density (N_H) of the outflow [16, 17, 77, 82]. Using Cloudy [21, version c17.00], we created a grid of photoionization models in order to find the values of N_H and U_H that best fit the ionic column density measurements. Assuming the spectral energy distribution (SED) of quasar HE0238-1904 (hereafter HE0238) [14], we created a grid of models with varying values of N_H and U_H. The N_H and U_H values used for each model determines the column density of each ion, which we compared with the measured values in Table 3.2. A χ^2 analysis has given us the closest matching model to the measurements, as shown in Fig. 3.4.

We assumed solar metallicity and searched for a one-phase solution (see plot a of Fig. 3.4), and here report the best fitting N_H and U_H in Table 3.3. The solution displays a poor fit to the constraints given by ions such as P v, S vi, and N v. To improve the models' fit with the data, we have calculated one-phase (plot a of Fig. 3.4) and two-phase (plot b of Fig. 3.4) solutions with both solar and supersolar [$Z = 4.68 Z_\odot$, 3, 11] metallicities, and computed the physical parameters as shown in Table 3.3. The ratios between modeled and measured column densities can be found in Table 3.2.

For the two-phase solutions, we attributed the column densities of Fe ii and O i to the low-ionization phase, as it was more in line with the constraints given by the measured column densities. The $\log n_e$ values (as estimated in Section 3.4.3) for the high-ionization phase were calculated assuming that the low and high-ionization phases shared the same distance from the central source. Note that the two-phase solutions, both for solar and supersolar metallicity, yield better fits to the column density measurements (see Fig. 3.4).

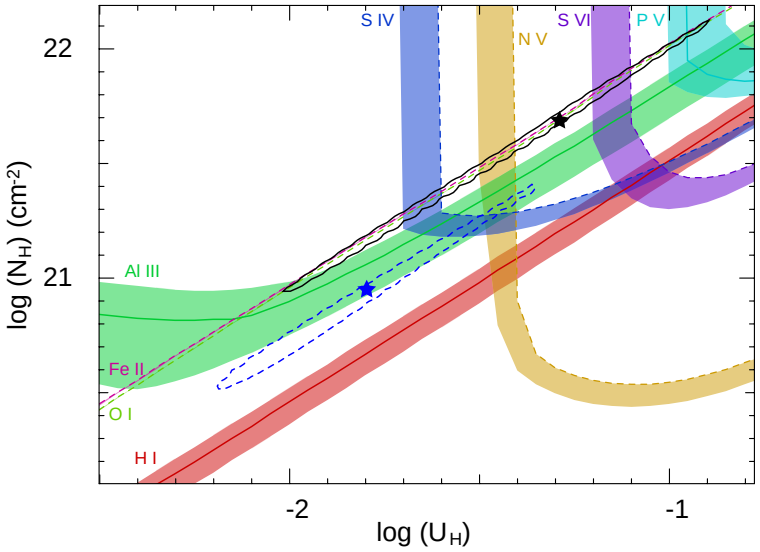

(a) One-phase solution

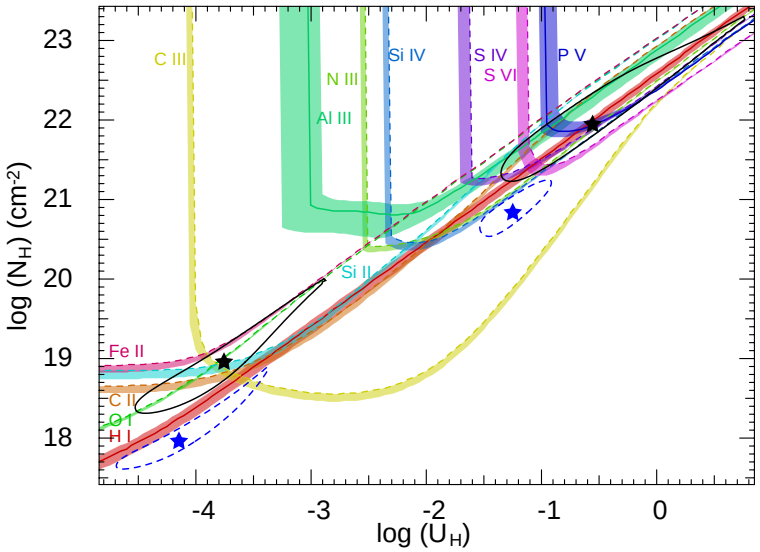

(b) Two-phase solution

Figure 3.4 Plot of $\log N_H$ vs. $\log U_H$ for S1. The colored lines represent the N_H and U_H values allowed by the measured column densities of ions. Solid and dashed lines represent measurements and lower limits, respectively. The colored bands attached to the lines show the uncertainties in ionic column densities. The black stars and ellipses represent the N_H and U_H solutions, and the 1σ range, assuming solar metallicity. The blue stars and blue dashed ellipses represent the solutions and 1σ range assuming supersolar metallicity [$Z = 4.68 Z_\odot$, 3, 11]. Note that the lower limits of ions such as C IV and N V are satisfied by any point above their respective colored bands. The high-ionization phase of the two-phase solution in plot b satisfies the lower limits from S IV, S VI, C IV, and N V, making the two-phase solution a better fit to the constraints than the one-phase solution shown in plot a. The HE0238 SED is assumed.

3.4.3 Electron Number Density

The electron number density (n_e) of the outflow can be found through comparing the column densities of different energy states of ions [e.g., 89]. S1 has absorption troughs of the resonance and excited states of Si II, O I, and Fe II, which we could potentially use for our n_e measurement. We used the CHIANTI 9.0.1 Database [12, 13] for this task, as it models the ratio between energy states dependent on n_e based on collisional excitation.

The Si II ground and excited states display troughs that are nearly identical in depth (See plot d in Fig. 3.3), suggesting non-black saturation. As it is difficult to find a concrete constraint on the ratio between the two states, we excluded Si II from this process. Finding the ratios between excited and ground states of Fe II and O I gave unphysical values, suggesting saturation of the ground states of Fe II and O I as well. Thus, we found the ratios between excited states instead, as shown in Fig. 3.5. We then found the weighted mean of the $\log n_e$ values from the different ratios, following the linear model method described by [136]. The resulting value of $\log n_e$ can be seen in Table 3.3.

While we excluded Si II from the process of finding $\log n_e$, we confirmed that the lower limit of the Si II column density was satisfied by the combination of the N_H, U_H, and n_e parameters found by using Cloudy models. The solar one-phase solution estimates $\log N(\text{Si II}) \approx 15.01$, while the low ionization phase of the solar two-phase solution predicts $\log N(\text{Si II}) \approx 14.37$, both of which are above the lower limit reported in Table 3.2. While a comparison with an analysis of C III* would have been helpful for additional confirmation of n_e [e.g. 92, 96, 131, 137], we were unable to identify the absorption troughs of the C III* 1175 Å multiplet, due to their indistinguishability with the Lyman-alpha forest lines (See Figure 3.1). We modeled the column densities of the different energy levels with Cloudy using the N_H, U_H, and n_e values corresponding to each solution (See Table 3.4). The ratio between the J=2 energy

state and the J=0 state ranges between 0.003 and 1.86.

3.5 Results

3.5.1 Distance and Kinetic Luminosity of the Outflow

The electron number density allows us to find the distance of the outflow from its central source, based on the following definition of the ionization parameter:

$$U_H \equiv \frac{Q_H}{4\pi R^2 n_H c} \tag{3.1}$$

where Q_H is the rate of Hydrogen ionizing photons, R is the distance of the outflow from the quasar, and n_H is the Hydrogen number density. Since $n_e \approx 1.2 n_H$ for highly ionized plasma [83], and we found the values of both U_H and n_e in Section 3.4 (See Table 3.3), we could solve the equation for R once the value of Q_H was determined.

Following the method of previous works [e.g. 17, 82], we scaled the HE0238 SED to match the continuum flux at rest wavelength $\lambda = 1350$ Å from the SDSS observation on October 21, 2001 ($F_\lambda = 7.27^{+0.82}_{-0.82} \times 10^{-17}$ erg s^{-1} cm^{-2}Å^{-1}), and integrated over the scaled SED for energies above 1 Ryd, finding bolometric luminosity $L_{Bol} = 1.8^{+0.2}_{-0.2} \times 10^{47}$ erg s^{-1} and $Q_H = 1.13^{+0.13}_{-0.13} \times 10^{57}$ s^{-1}. The outflow distance calculated from these values is shown in Table 3.3.

Assuming an outflow with the geometry of an incomplete spherical shell, we calculated the mass flow rate and kinetic luminosity with the following equations [118]:

$$\dot{M} \simeq 4\pi \Omega R N_H \mu m_p v \tag{3.2}$$

$$\dot{E}_k \simeq \frac{1}{2}\dot{M}v^2 \tag{3.3}$$

where Ω is the global covering factor (fraction of the solid angle covered by the outflow), $\mu = 1.4$ is the mean atomic mass per proton, m_p is the proton mass, and v is the outflow velocity. We assumed $\Omega = 0.2$, which is the portion of quasars from which C IV BALs are detected [37]. Calculating the kinetic luminosity yielded values ranging from $\log \dot{E}_K = 43.06^{+0.21}_{-0.36}$ [erg s^{-1}] for the one-phase solution assuming solar metallicity, to $\log \dot{E}_K = 45.55^{+0.90}_{-0.32}$ [erg s^{-1}] for the two-phase solution assuming solar metallicity. Results based on the other solutions can be found in Table 3.3.

3.5.2 Changes in the High Velocity Mini-BAL Trough (S5)

We examined the time-variability of the C IV mini-BAL of S5. We adopted the method of [17], fitting two Gaussian profiles, one broad and one narrow, with the absorption. We added a constraint to the centroid velocity of the narrow Gaussian (-7900 km s^{-1} $< v_c <$ -7600 km s^{-1}), as there was a distinct absorption feature found at $v \approx -7800$km s^{-1}. As shown in Fig. 3.6, the smaller absorption feature grows between the observations in 2000 and 2001, but nearly vanishes by 2005. The larger feature becomes gradually shallower. More information of the Gaussian fits can be found in Table 3.5.

3.6 Discussion

3.6.1 AGN Feedback Contribution of the Outflow

The kinetic luminosity ($\dot{E}_K$) of the outflow must be at least $\sim 0.5\%$ [58] or $\sim 5\%$ [53] of the quasar's Eddington luminosity (L_{Edd}) to be a significant contributor to AGN feedback. To

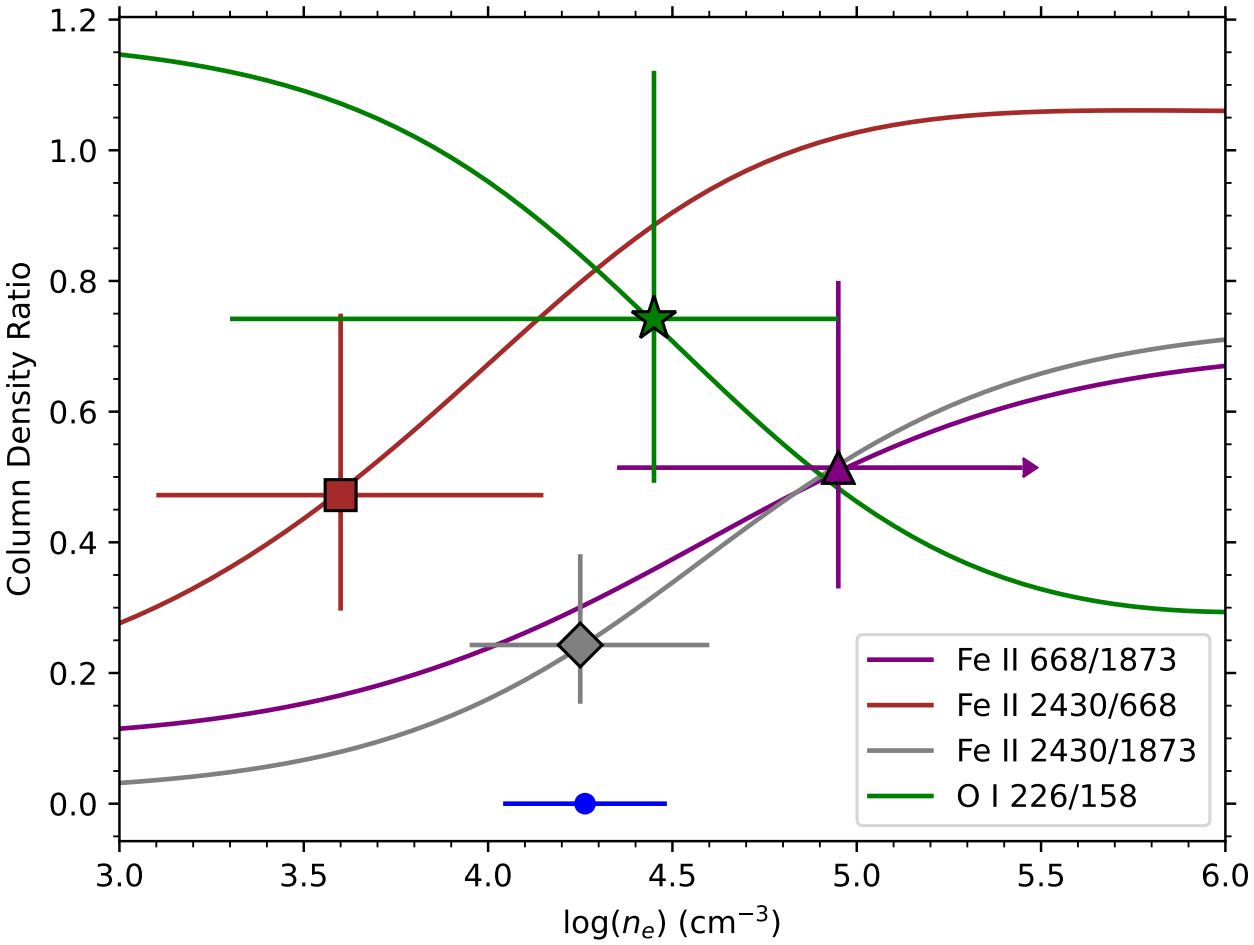

Figure 3.5 The ratio between the abundances of different energy states of O I and Fe II in S1, assuming a temperature of 10,000 K. The curves represent the theoretical ratios modeled with CHIANTI. The crosses on the curves represent the upper and lower limits of the ratios based on the measured column densities, along with the associated $\log n_e$ values.The ratios are color coded and marked with shapes: Fe II* 668/1873 with a triangle, Fe II* 2430/668 with a square, Fe II* 2430/1873 with a diamond, and O I* 226/158 with a star. The rightward arrow on the purple cross of the Fe II* 668/1873 ratio shows that the data point is a lower limit, as the upper limit of the ratio exceeds the highest point of the curve. The blue dot and error bars show the weighted average of $\log n_e$ based on the four measured ratios, which we adopted for our analysis.

Table 3.3 Physical Properties of J2357-0048 Outflow. Note that the high-ionization and low-ionization phases of the two-phase solutions are assumed to be co-spatial (at the same distance from the central source). The kinetic luminosity to bolometric luminosity ratios are included for comparison.

Solution	Solar, one-phase	Solar, two-phase		Supersolar, one-phase	Supersolar, two-phase	
Phase	One-phase	Low	High	One-phase	Low	High
$log(N_{\rm H})$ [cm^{-2}]	$21.69^{+0.44}_{-0.75}$	$18.96^{+1.05}_{-0.64}$	$21.95^{+1.36}_{-0.72}$	$20.95^{+0.46}_{-0.43}$	$17.96^{+0.93}_{-0.35}$	$20.84^{+0.41}_{-0.30}$
$log(U_{\rm H})$ [dex]	$-1.29^{+0.39}_{-0.73}$	$-3.76^{+0.88}_{-0.77}$	$-0.56^{+1.32}_{-0.80}$	$-1.80^{+0.44}_{-0.39}$	$-4.15^{+0.77}_{-0.54}$	$-1.25^{+0.34}_{-0.29}$
$log(n_{\rm e})$ [cm^{-3}]	$4.3^{+0.2}_{-0.2}$	$4.3^{+0.2}_{-0.2}$	$1.1^{+1.2}_{-1.5}$	$4.3^{+0.2}_{-0.2}$	$4.3^{+0.2}_{-0.2}$	$1.4^{+0.9}_{-0.7}$
Distance [pc]	640^{+890}_{-260}	10900^{+16600}_{-7100}		1140^{+780}_{-500}	17100^{+16600}_{-10300}	
$\dot{M}$ [$M_\odot$yr^{-1}]	14^{+9}_{-8}	4400^{+30700}_{-2270}		47^{+29}_{-18}	540^{+1190}_{-370}	
$\dot{M}v$ [10^{34} ergs cm^{-1}]	14^{+9}_{-8}	4400^{+30800}_{-2280}		47^{+29}_{-18}	540^{+1190}_{-370}	
$log(\dot{E}_K)$ [erg s^{-1}]	$43.06^{+0.21}_{-0.36}$	$45.55^{+0.90}_{-0.32}$		$43.57^{+0.21}_{-0.21}$	$44.63^{+0.51}_{-0.50}$	
$\dot{E}_K/L_{Edd}$ [%]	$0.008^{+0.006}_{-0.004}$	$2.35^{+16.80}_{-1.27}$		$0.025^{+0.019}_{-0.011}$	$0.29^{+0.67}_{-0.20}$	
$\dot{E}_K/L_{Bol}$ [%]	$0.006^{+0.004}_{-0.004}$	$1.96^{+13.68}_{-1.02}$		$0.021^{+0.013}_{-0.008}$	$0.24^{+0.53}_{-0.16}$	

Table 3.4 Modeled C III* column densities of the J2357-0048 outflow, in units of cm^{-2}, along with the ratio between the energy states of J=2 and J=0.

Energy level	Solar,one-phase	Solar,two-phase	Supersolar,one-phase	Supersolar,two-phase
J=0	3.66×10^{13}	9.92×10^{12}	1.25×10^{11}	4.48×10^{9}
J=1	2.96×10^{9}	1.21×10^{6}	1.26×10^{7}	1.81×10^{3}
J=2	5.98×10^{13}	3.14×10^{10}	2.33×10^{11}	2.74×10^{7}
J=2/J=0	1.63	0.003	1.86	0.006

Table 3.5 Gaussian Fits of C IV mini-BAL at Each Epoch

MJD	Date	Δt_{Rest} (days)	v_n (km s^{-1})	Δv_n (km s^{-1})	EW_n (km s^{-1})	v_w (km s^{-1})	Δv_w (km s^{-1})	EW_w (km s^{-1})
51791	Sep. 4, 2000	0	-7770 ± 40	0	45	-8650 ± 40	0	690
52203	Oct. 21, 2001	193.9	-7710 ± 50	$+60 \pm 60$	180	-8650 ± 70	0 ± 80	500
53619	Sep. 5, 2005	860.6	-7760 ± 14	-10 ± 40	12	-8577 ± 6	$+70 \pm 40$	515
55477	Oct. 10, 2010	1735.4	-7830 ± 60	-60 ± 70	15	-8650 ± 50	$+0 \pm 70$	500
56956	Oct. 26, 2014	2431.7	-7900 ± 5180	-130 ± 5180	6	-8600 ± 50	$+50 \pm 70$	470
57688	Oct. 27, 2016	2776.3	-7900 ± 200	-10 ± 200	15	-8590 ± 80	$+60 \pm 90$	500

Note. — Table of the centroid velocity and equivalent width of the Gaussian profiles fit to the C IV absorption of S5. v_n and v_w are the centroid velocities of the narrow and wide Gaussians. EW_n and EW_w are the equivalent widths of the Gaussians in velocity space. Δv_n, Δv_w, and Δt_{Rest} are the changes in velocity and time in the quasar's rest frame from the MJD=51791 epoch.

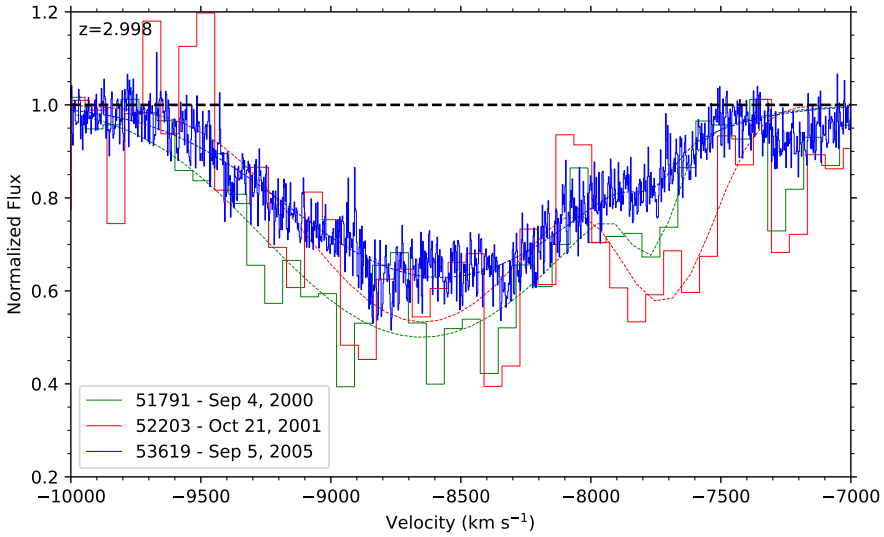

(a)

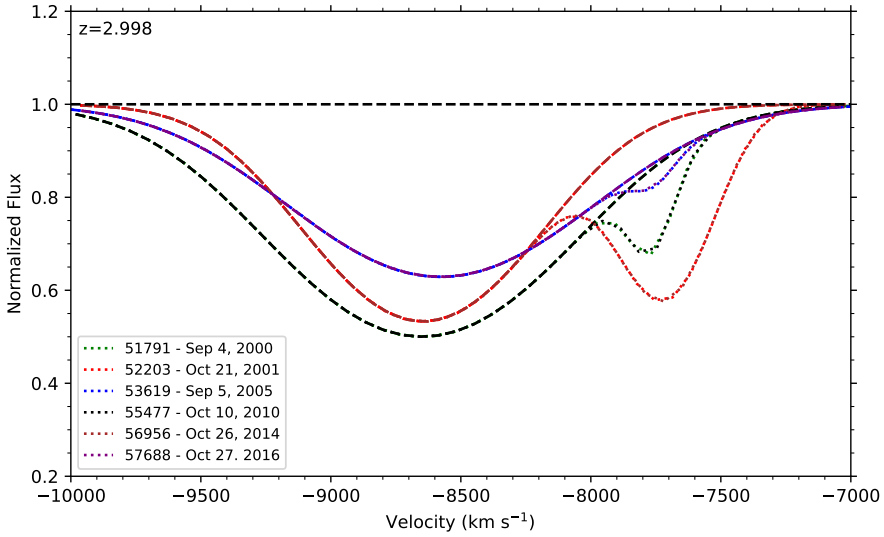

(b)

Figure 3.6 Normalized flux vs. velocity of the S5 C IV mini-BAL at three observational epochs. A best fit of two Gaussians was used to model the absorption. (a) shows the models over the data of three epochs, and (b) shows the Gaussians of all six epochs.

find the ratio, we first found the mass and the Eddington luminosity of the quasar. Following the method demonstrated by [138], we computed the mass of the black hole based on the FWHM of the C IV emission in the SDSS spectrum. To account for the blueshift of C IV, we adopted the correction method by [139]. This yields a mass of $M_{BH} = 1.16^{+0.40}_{-0.30} \times 10^9 M_\odot$, corresponding to an Eddington luminosity of $L_{Edd} = 1.5^{+0.5}_{-0.4} \times 10^{47}$ erg s^{-1}. Our one-phase solutions yield $\dot{E}_K/L_{Edd} = 0.008^{+0.006}_{-0.004}\%$ for solar metallicity and $\dot{E}_K/L_{Edd} = 0.025^{+0.019}_{-0.011}\%$ for supersolar metallicity, while the two-phase solutions yield $\dot{E}_K/L_{Edd} = 2.35^{+16.80}_{-1.27}\%$ for solar metallicity and $\dot{E}_K/L_{Edd} = 0.29^{+0.67}_{-0.20}\%$ for supersolar metallicity (See Table 3.3). All but the two-phase solar metallicity solution are insufficient to contribute to AGN feedback. The 2.35% ratio from the two-phase solar metallicity solution is above the $\sim 0.5\%$ cutoff by [58]. This is in contrast with the outflow of SDSS J024221.87+004912.6, another SQUAD quasar analyzed by [17], which exceeded 5% of the quasar's Eddington luminosity. Other quasar absorption outflows in the literature have $\dot{E}_k/L_{Edd}$ values ranging from 0.001% [140] to an upwards of $\sim 10\%$ [90]. A larger sample size of analyzed objects may be needed for a statistical analysis.

3.6.2 The Time Variability of S5

The most notable change in S5 over time has been of the width and depth of the narrow feature at $v = -7800$ km s^{-1}, which disappeared in the spectrum of September 2005. The variability of the broader feature afterwards has been minimal, with the equivalent width staying at ~ 500 km s^{-1}.

One possible explanation for the variability is that there has been a change in photoionization over the different epochs, affecting the depth of the narrow subcomponent [e.g. 17, 122]. While other works involve the acceleration of outflow systems due to significant velocity

shifts [e.g. 141], the velocity changes in S5 have been minimal, mostly staying within the margin of error through each epoch.

3.7 Summary and Conclusion

From the VLT/UVES spectrum of the quasar SDSS J2357-0048, we have identified a BAL outflow with four subcomponents, S1, S2, S3, and S4, as well as a high-velocity C IV mini-BAL, which we label as S5. This paper has presented the analysis of S1, based on the column densities of 14 ions shown in Table 3.2. We have found estimates of N_H and U_H through photoionization analysis.

We used the abundance ratios between different energy states of O I and Fe II to find the electron number density n_e of S1, as shown in Fig. 3.5. We have also found other physical parameters of S1 such as distance from the quasar, mass flow rate, and kinetic luminosity, using Equations (3.1), (3.2), and (3.3). Based on the ratio between the kinetic luminosity $\dot{E}_k$ and the Eddington luminosity L_{Edd} (see Table 3.3), the outflow's ability to contribute to AGN feedback has been found to be dependent on the model.

We also examined the time-variability of the S5 C IV mini-BAL, based on the SDSS and UVES spectra (see Fig. 3.6). The small absorption feature at $v = -7700$ km s^{-1} became deeper between the 2000 and 2001 epochs, and nearly vanished in the 2005 epoch. The mini-BAL itself appears to have become gradually shallower over time.

Acknowledgements

NA and DB acknowledge support from NSF grant AST 2106249, as well as NASA STScI grants GO 14777, 14242, 14054, 14176, and AR-15786. DB acknowledges support from the Virginia Space Grant Consortium Graduate Research Fellowship Program. We also thank the anonymous referee for their constructive comments that helped improve this paper.

Data Availability

The normalized UVES spectrum of J2357-0048 is part of the SQUAD database made available by [142] and described by [10]. The SDSS spectra used for the time variability analysis can be found in the SDSS archive [132, 133, 143, 144].

Chapter 4

VLT/UVES Observation of the Outflow in Quasar SDSS J1439-0106

Foreword

This chapter is based on the published paper "*VLT/UVES Observation of the Outflow in Quasar SDSS J1439-0106*" [19]. I led the project by analyzing the data, doing calculations, creating the figures, and writing the paper.

4.1 Abstract

We analyze the VLT/UVES spectrum of the quasar SDSS J143907.5-010616.7, retrieved from the UVES Spectral Quasar Absorption Database. We identify two outflow systems in the spectrum: a mini broad absorption line (mini-BAL) system and a narrow absorption line (NAL) system. We measure the ionic column densities of the mini-BAL ($v = -1550$ km s^{-1}) outflow, which has excited state absorption troughs of Fe II. We determine that the electron number density $\log n_e = 3.4^{+0.1}_{-0.1}$ based on the ratios between the excited and ground state abundances of Fe II, and find the kinetic luminosity of the outflow to be $\lesssim 0.1\%$ of the quasar's Eddington luminosity, making it insufficient to contribute to AGN feedback.

4.2 Introduction

Quasar outflows are often found in the spectra of quasars ($\lesssim 40\%$) as blueshifted absorption troughs relative to the rest frame of the quasars [37, 38, 88]. Often invoked as potential contributors to AGN feedback, analysis of these outflows can provide us with insight into galaxy evolution [e.g. 34–36, 145]. The outflows must have a kinetic luminosity ($\dot{E}_k$) of at least $\sim 0.5\%$ [58] or perhaps as much as $\sim 5\%$ [53] of the quasar's Eddington luminosity ($L_{\rm Edd}$), depending on the theoretical model, to be contributors of AGN feedback. Several outflows with sufficient $\dot{E}_k$ have been found in past studies [e.g. 14, 17, 77, 82, 85, 89, 90, 131].

Crucial to the process of finding a quasar outflow's kinetic luminosity is finding its mass flow rate ($\dot{M}$), which is dependent on its hydrogen column density (N_H), ionization parameter (U_H), and electron number density (n_e) [92]. Analysis using this method has been conducted in the past (e.g. [7, 9, 23, 93, 95]). The value of n_e can be found by calculating the ratios between the excited and resonance state column densities of ions [97]. This paper presents the determination of $\dot{E}_k$ of one of the outflow components of the quasar SDSS J143907.50-010616.7 (hereafter J1439-0106), based on the normalized VLT/UVES spectrum acquired from the Spectral Quasar Absorption Database (SQUAD) published by [10]. Similar analysis using data from this database has been conducted in previous studies ([17, 18, 23]).

The UVES data of J1439-0106 was collected as part of the programs 081.B-0285(A) and 083.B-0604(A), and has been added to the SQUAD database complied by [10]. From the normalized spectrum, we identify two distinct absorption outflow systems, which we label here as the mini broad absorption line (mini-BAL) system S1, and the narrow absorption line (NAL) system S2, of which we find S1 suitable for our analysis thanks to the presence of excited state absorption troughs.

This paper is structured as follows. Section 4.3 describes the observation of J1439-0106, as

well as the method we used to retrieve its spectral data. Section 4.4 discusses the measurement of ionic column densities of S1, as well as the determination of N_H, U_H, and n_e. Section 4.5 shows the resulting calculation of $\dot{M}$ and $\dot{E}_k$, as well as its ratio with $L_{\rm Edd}$. Section 4.6 provides a discussion of these results, as well as a comparison with previous work. Section 4.7 summarizes and concludes the paper. We adopt a cosmology of $h = 0.696$, $\Omega_m = 0.286$, and $\Omega_\Lambda = 0.714$ [99]. We use the Python astronomy package Astropy [100, 101] for cosmological calculations.

4.3 Observation and Data Acquisition

J1439-0106 (J2000: RA=14:39:07.5, DEC=01:06:16.7, z=1.819) was observed with VLT/UVES on 1 May, 2008 as part of the program 081.B-0285(A), and on 16 April, 2009 as part of 083.B-0604(A), with minimal variability between the two epochs. The combined spectral data, covering wavelengths between 3284–9466Å, was normalized by the quasar's continuum and emission, and added to the SQUAD database by [10]. The spectrum is shown in Fig. 4.1. The object was also observed in 15 May, 2002 as part of the Sloan Digital Sky Survey (SDSS), the spectrum of which we use to calibrate the flux shown in Fig. 4.1, as well as find the bolometric and Eddington luminosities of the quasar.

From the UVES spectrum, we identify two different absorption outflow systems, mini-BAL S1 ($v \approx -1550\,{\rm km\ s^{-1}}$) and NAL S2 ($v \approx -2750\,{\rm km\ s^{-1}}$). We focus on S1 in the analysis of this paper, as it shows troughs of several Fe II excited lines, allowing us to find the outflow distance from the source, and by extension, the mass flow rate.

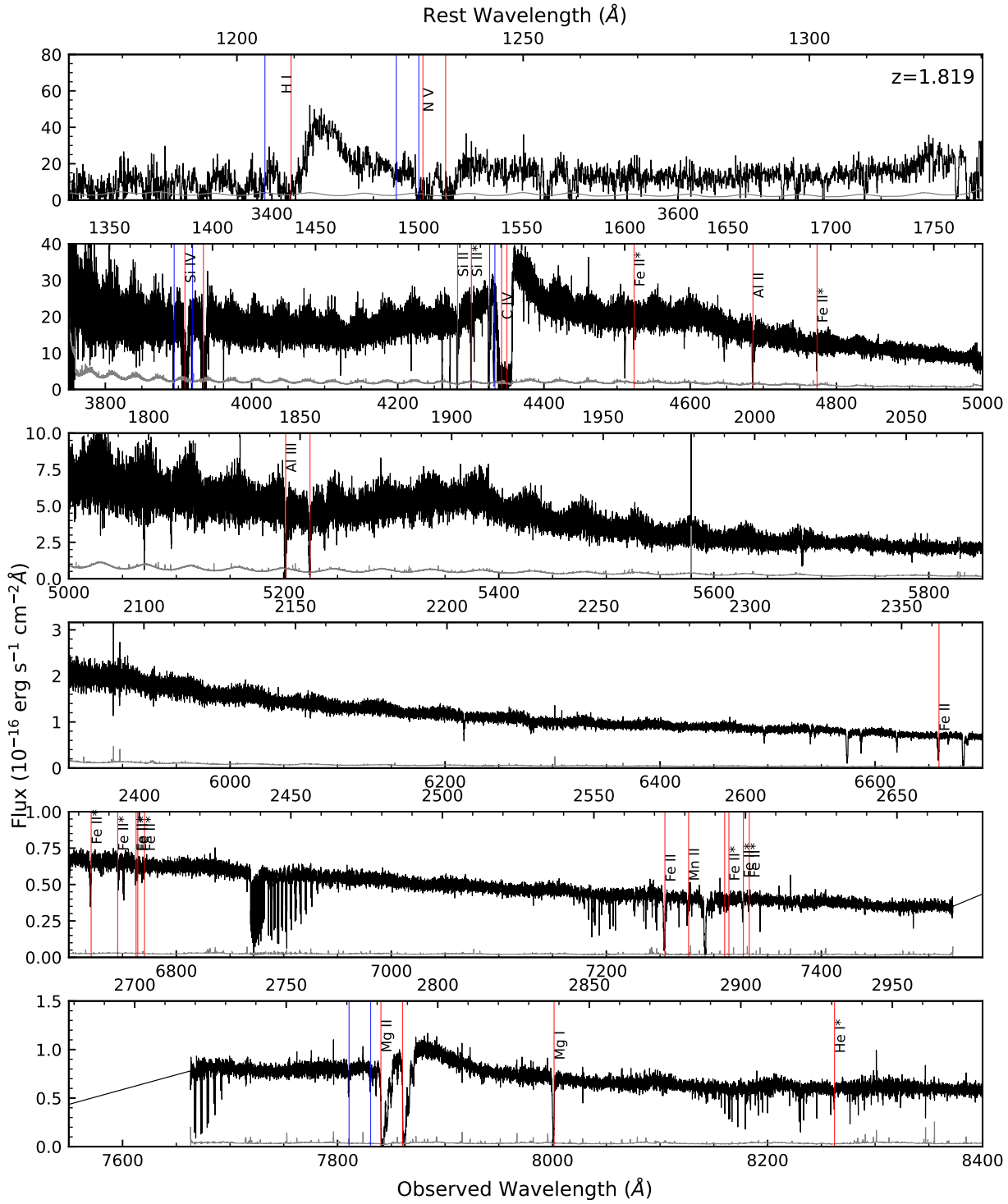

Figure 4.1 The UVES spectrum of J1439-0106. The normalized spectrum was multiplied by the continuum model by [10], and scaled to match the flux of the SDSS spectrum at observed wavelength 6500Å. Red vertical lines mark the absorption features of S1, and the blue vertical lines mark the features of S2. While in S2, troughs of C IV, Si IV, Mg II, H I, and N V are detected, they are shallower and narrower than those of S1. The first panel has been binned by 10 pixels for clarity.

4.4 Analysis

4.4.1 Ionic Column Densities

Finding the ionic column densities (N_{ion}) of S1 is crucial to determining the energetics parameters of the outflow system. In order to measure the column densities, we use the systemic redshift of the quasar to convert the spectrum from wavelength space to velocity space, as shown in Fig. 4.2. We then use two different methods to find the ionic column densities, assuming either an apparent optical depth (AOD) of a uniform outflow [107], or partial covering (PC) based on a velocity dependent covering factor [108–110].

The AOD method and PC method have different advantages over one another, with the PC method being particularly more helpful in finding more accurate column densities for ions with absorption doublets or multiplets, while the AOD method yields lower limits to the column densities [111–113, 118]. The differences between the two methods is explained in further detail in Section 3.1 of [17].

We choose our integration range for each ion based on the visibility of absorption troughs, as shown in Fig. 4.2. In cases were the red and blue troughs of a doublet are blended (e.g. C IV), we choose a range in which the red and blue troughs are not overlapping, in order to gain a lower limit of the column density. The measured column densities are shown in Table 4.1. Note that we add a 20% error in quadrature to account for the uncertainty in the continuum model [7].

4.4.2 Photoionization Analysis

With the ionic column densities found, we can use these measurements to find the hydrogen column density (N_H) and ionization parameter (U_H) of S1 [e.g. 17, 77, 82, Walker et al.

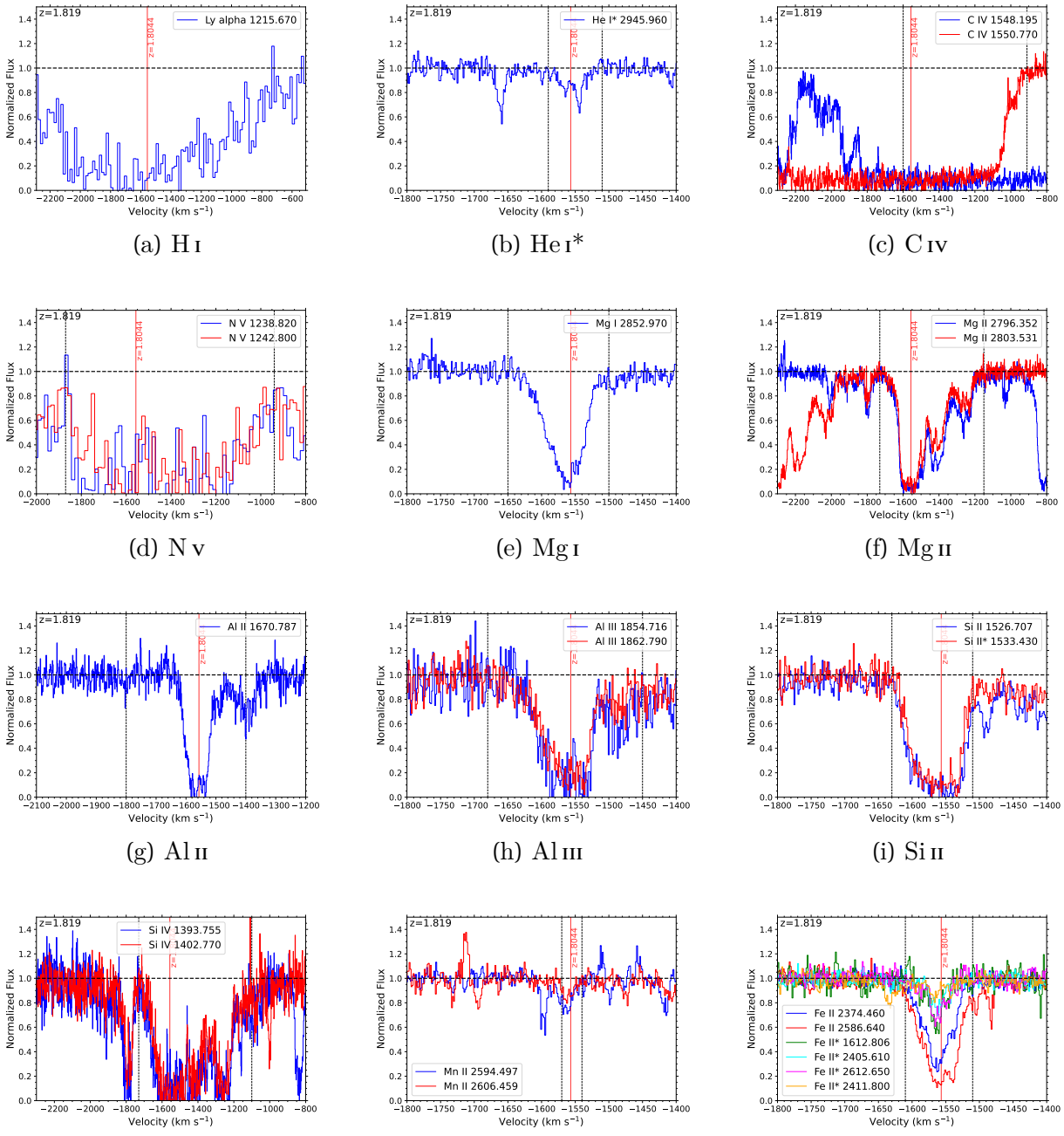

(a) H I (b) He I* (c) C IV

(d) N V (e) Mg I (f) Mg II

(g) Al II (h) Al III (i) Si II

(j) Si IV (k) Mn II (l) Fe II

Figure 4.2 Absorption troughs of the outflow system S1 plotted in velocity space. The horizontal dashed line indicates the continuum level, while the vertical red line shows the velocity of S1. The vertical dotted lines show the integration range used to find the column densities.

Table 4.1 J1439-0106 outflow column densities from UVES observations. The values are in units of 10^{12} cm^{-2}.

Troughs	AOD	PC	Adopted
S1, $v = -1550$ km s^{-1}			
H I	1450^{+80}_{-40}		$> 1450_{-290}$
He I*	100^{+6}_{-6}		$> 100_{-20}$
C IV	3440^{+50}_{-40}		$> 3440_{-690}$
N V	3370^{+220}_{-140}		$> 3370_{-690}$
Mg I	$7.8^{+0.2}_{-0.2}$		$> 8_{-1.6}$
Mg II	196^{+4}_{-3}	250^{+70}_{-4}	250^{+80}_{-50}
Al II	25^{+2}_{-1}		$> 25_{-5}$
Al III	96^{+3}_{-3}		$> 100_{-20}$
Si II total	720^{+30}_{-20}		$> 720_{-100}$
Si II 0	410^{+25}_{-15}		
Si II*	310^{+15}_{-10}		
Si IV	850^{+40}_{-20}		$> 850_{-170}$
Mn II	$2.7^{+0.3}_{-0.3}$	$2.8^{+0.2}_{-0.2}$	$2.8^{+0.6}_{-0.6}$
Fe II total			$> 430_{-60}$
Fe II 0	230^{+4}_{-4}	270^{+5}_{-5}	270^{+50}_{-50}
Fe II* 385	16^{+3}_{-3}	21^{+3}_{-1}	21^{+5}_{-4}
Fe II* 668	14^{+4}_{-4}	18^{+6}_{-4}	18^{+7}_{-6}
Fe II* 862	7^{+1}_{-1}		$7^{+1.5}_{-1.6}$
Fe II* 977	$3.8^{+0.4}_{-0.3}$		$3.8^{+0.8}_{-0.8}$
Fe II* 1873	100^{+10}_{-10}	110^{+10}_{-10}	110^{+20}_{-20}

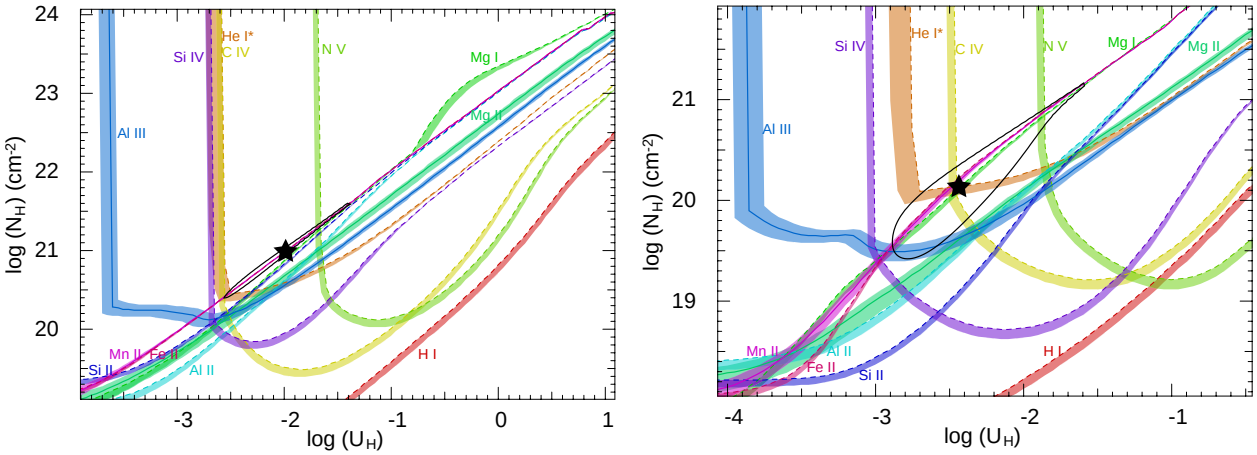

(a) Solar metallicity

(b) Super-solar metallicity (see text)

Figure 4.3 Plots of $\log N_H$ vs. $\log U_H$ based on the ionic column densities of S1. The colored lines show the values of N_H and U_H allowed by the measured column density of each ion. Solid lines indicate measurements, while the dashed lines show lower limits from using the AOD method. The shaded bands attached to the lines represent the uncertainties in column density. The black stars indicate the solutions found via χ^2 analysis, and the black ellipses represent the 1σ error.

submitted]. We use the spectral synthesis code Cloudy [21, version c17.00] to create a grid of simulated models based on varying values of N_H and U_H, using the spectral energy distribution (SED) of quasar HE0238-1904 (hereafter HE0238) [14]. Via χ^2 analysis, we find the model with ionic column densities that best match the measured values, as shown in Fig. 4.3. We use two different grids based on metallicity values, solar and super-solar [$Z = 4.68 Z_\odot$ 3, 11], to find two different solutions, as previous studies show that the metallicities of outflows are between $Z_\odot$ and $5Z_\odot$ [e.g. 3, 115, 146]. The values of N_H and U_H are shown in Table 4.2.

4.4.3 Electron Number Density

Finding the distance of the outflow from its source is crucial to finding the mass flow rate, and by extension, the kinetic luminosity. This is done by finding the electron number density (n_e),

which is measured by taking the ratios between excited and ground state column densities of ions [e.g. 17, 89]. The CHIANTI 9.0.1 Database [12, 13] models the n_e dependent ratios between different energy states based on collisional excitation, and can be used to find the value of n_e from measured column densities. S1 shows absorption lines of five different excited states, as well as the ground state, of Fe II, and we find n_e by finding the ratios between these excited states and the resonance state (N(Fe II*)/N(Fe II)), as shown in Fig. 4.4. While we find troughs of Si II and Si II*, they are unreliable for finding n_e due to the saturation of the troughs (see plot i in Fig. 4.2). We find the weighted mean of the $\log n_e$ values measured using the different excited states via the linear model method described by [136]. This yields a value of $\log n_e = 3.4^{+0.1}_{-0.1}$.

4.5 Results

The distance of the outflow from the quasar can be found based on the definition of the ionization parameter:

$$U_H \equiv \frac{Q_H}{4\pi R^2 n_H c} \tag{4.1}$$

where Q_H is the emission rate of hydrogen ionizing photons, R is the distance from the source, c is the speed of light, and n_H is the hydrogen number density. Once we find Q_H, we can use the values of U_H and n_e found in Section 4.4 to find R, as $n_e \approx 1.2 n_H$ in highly ionized plasma [83].

We find the value of Q_H as follows, as per previous works [e.g. 17, 82, Byun et al. 2022, submitted; Walker et al. 2022, submitted]. We scale the SED of HE0238 to match the continuum flux of J1439-0106 at observed wavelength $\lambda = 6500$ Å, from the SDSS observation of 15 May, 2002 ($F_\lambda = 8.49^{+0.64}_{-0.64} \times 10^{-17}$ erg s^{-1} cm^{-2} Å^{-1}). We then integrated over the SED for energies over 1 Ryd, resulting in $Q_H = 5.3^{+0.4}_{-0.4} \times 10^{56}$ s^{-1}.

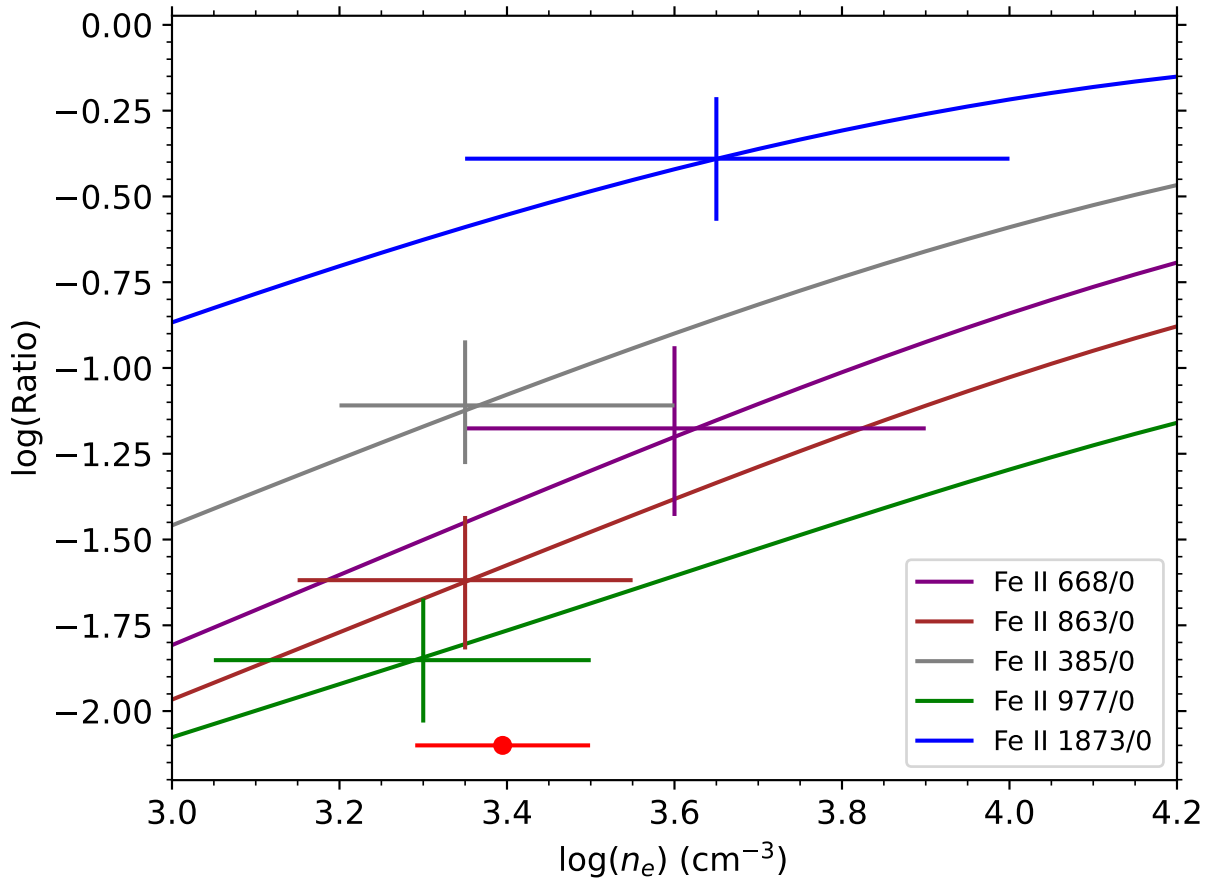

Figure 4.4 Log-log plot of the ratios between excited state Fe II and resonance state Fe II vs. electron number density. The curves show the theoretical relationship between the ratios and n_e values, while the crosses show the measured ratios and their associated n_e. The red dot with error bars indicates the weighted mean of $\log n_e$. A temperature of 10,000 K is assumed.

Once the distance is found, we can find the mass flow rate ($\dot{M}$) and kinetic luminosity ($\dot{E}_k$) as shown in the following [118]:

$$\dot{M} \simeq 4\pi\Omega R N_H \mu m_p v \tag{4.2}$$

$$\dot{E}_k \simeq \frac{1}{2}\dot{M}v^2 \tag{4.3}$$

where Ω is the fraction of the solid angle covered by the outflow, $\mu = 1.4$ is the molecular weight, m_p is the mass of a proton, and v is the outflow velocity. We assume $\Omega = 0.2$ based on ratio of quasars with C IV BALs reported by [37]. When propagating the uncertainties of the parameters, we take into account the positive correlation between U_H and N_H in the photoionization solutions (see Fig. 4.3) to avoid overestimating our errors (see Walker et al. (2022, submitted) for a detailed explanation). The values found for $\dot{M}$ and $\dot{E}_k$ are in Table 4.2.

4.6 Discussion

4.6.1 AGN Feedback Contribution

In order to be a major contributor to AGN feedback, S1 needs to have a kinetic energy of at least $\sim 0.5\%$ [58] or perhaps as much as $\sim 5\%$ [53] of the quasar's Eddington luminosity (L_{Edd}), depending on the theoretical model. To find L_{Edd}, we follow the method by [17], finding the full-width half max (FWHM) of the Mg II emission in the SDSS spectrum, and using the Mg II-based equation by [123] to find the mass of the black hole. As there is Fe II emission in the region of Mg II emission, we use the Fe II template by [124] and run a best fit algorithm to match the template to the spectrum, following [125].

Table 4.2 Physical Properties of J1439-0106 Outflow.

Solution	Solar	Super-solar
$log(N_{\rm H})$ [cm^{-2}]	$20.99^{+0.61}_{-0.59}$	$20.13^{+1.03}_{-0.71}$
$log(U_{\rm H})$ [dex]	$-1.99^{+0.60}_{-0.58}$	$-2.44^{+0.85}_{-0.45}$
$log(n_{\rm e})$ [cm^{-3}]	$3.4^{+0.1}_{-0.1}$	$3.4^{+0.1}_{-0.1}$
Distance [pc]	2600^{+2500}_{-1300}	4400^{+3100}_{-2800}
$\dot{M}$ [$M_{\odot}$yr^{-1}]	110^{+120}_{-60}	30^{+80}_{-20}
$\dot{M}v$ [10^{36} ergs cm^{-1}]	$1.1^{+1.2}_{-0.6}$	$0.27^{+0.82}_{-0.18}$
$log(\dot{E}_K)$ [erg s^{-1}]	$43.94^{+0.31}_{-0.32}$	$43.32^{+0.49}_{-0.61}$
$\dot{E}_K/L_{Edd}$ [%]	$0.099^{+0.12}_{-0.05}$	$0.023^{+0.053}_{-0.018}$

The resulting black hole mass is $M_{BH} = 7.05^{+2.68}_{-2.03} \times 10^8 M_{\odot}$, with a corresponding Eddington luminosity of $L_{Edd} = 8.89^{+3.38}_{-2.56} \times 10^{46}$ erg s^{-1}. The Eddington ratio of the outflow ranges from $0.099^{+0.12}_{-0.05}$% (for solar metallicity) to $0.023^{+0.053}_{-0.018}$% (for super-solar metallicity), which is below the threshold for AGN feedback contribution.

4.6.2 Comparison with Previous Work

We have found the value of n_H of S1 based on the ratios between the column densities of excited state and resonance state Fe II. This has notably done by [70] for the outflow of the quasar NVSS J235953-124148. The $\log n_e$ values from the different energy states in Fig. 4.4 are in agreement within ~ 0.2 dex, which is comparable to the agreement shown in Fig. 3 of [70], showing that the ratios between Fe II energy states can be consistently used to probe

the n_e value and the distance of an outflow from its source.

4.7 Summary and Conclusion

We have identified two outflow systems from the VLT/UVES spectrum of the quasar SDSS J1439-0106, the mini-BAL S1 and the NAL S2. After measuring the column densities of the ions identified in S1, we used these measurements to find the N_H and U_H values of S1 via photoionization analysis, using models of both solar and super-solar metallicity (see Fig. 4.3).

With the abundance ratios between five different excited states of Fe II and the resonance state, we found the electron number density of S1 (see Fig. 4.4). We have also found its distance from the quasar, the mass flow rate, and kinetic luminosity. Based on the ratio between the kinetic luminosity of S1 and the Eddington luminosity of the quasar, we conclude that it is insufficient for the outflow system to contribute to AGN feedback.

Acknowledgements

NA, DB and AW acknowledge support from NSF grant AST 2106249, and NASA STScI grants AR-15786, AR-16600, and AR-16601.

Data Availability

The normalized UVES spectrum of J1439-0106 is part of the SQUAD database made available by [142] and described by [10]. The SDSS spectrum is available in the SDSS database.

Chapter 5

Extreme FeLoBAL outflow in the VLT/UVES spectrum of quasar SDSS J1321-0041

Foreword

This chapter is based on the published paper "*Extreme FeLoBAL outflow in the VLT/UVES spectrum of quasar SDSS J1321-0041*" [20]. I led the project by analyzing the data, doing calculations, creating the figures, and writing the paper.

5.1 Abstract

5.1.1 Context

Quasar outflows are often analyzed to determine their ability to contribute to active galactic nucleus (AGN) feedback. We identified a broad absorption line (BAL) outflow in the VLT/UVES spectrum of the quasar SDSS J1321-0041. The outflow shows troughs from Fe II, and is thus categorized as an FeLoBAL. This outfow is unusual among the population of FeLoBAL outflows, as it displays C II and Si II BALs.

5.1.2 Aims

Outflow systems require a kinetic luminosity above $\sim 0.5\%$ of the quasar's luminosity to contribute to AGN feedback. For this reason, we analyzed the spectrum of J1321-0041 to determine the outflow's kinetic luminosity, as well as the quasar's bolometric luminosity.

5.1.3 Methods

We measured the ionic column densities from the absorption troughs in the spectrum and determined the Hydrogen column density and ionization parameter using those column densities as our constraints. We also determined the electron number density, n_e, based on the ratios between the excited-state and resonance-state column densities of Fe II and Si II. This allowed us to find the distance of the outflow from its central source, as well as its kinetic luminosity.

5.1.4 Results

We determined the kinetic luminosity of the outflow to be $8.4^{+13.7}_{-5.4} \times 10^{45}$ erg s^{-1} and the quasar's bolometric luminosity to be $1.72 \pm 0.13 \times 10^{47}$ erg s^{-1}, resulting in a ratio of $\dot{E}_k/L_{Bol} = 4.8^{+8.0}_{-3.1}\%$. We conclude that this outflow has a sufficiently high kinetic luminosity to contribute to AGN feedback.

5.2 Introduction

Active galactic nucleus (AGN) feedback is a process in which an AGN affects the evolution of its host galaxy, including the regulation of the star formation rate and the correlation

between the black hole and host galaxy mass [e.g., 34, 47, 147]. In quasars, AGN feedback is often attributed to outflows, which are found in $\lesssim 40\%$ quasar spectra as blueshifted absorption troughs [e.g., 36–38, 88, 145]. Outflow systems require a kinetic luminosity ($\dot{E}_k$) above $\sim 0.5\%$ of the quasar's luminosity [58], which [2] interpreted to be the Eddington luminosity (L_{Edd}). Outflow analyses have been conducted in past works, reporting quasar outflows with a sufficient value of $\dot{E}_k$ [e.g., 17, 18, 22, 23, 82, 90, 131].

The process of finding $\dot{E}_k$ involves measuring the ionization parameter (U_H) and electron number density (n_e) of the outflow, which leads to the distance from the central source (R) and mass outflow rate ($\dot{M}$) [92]. For the analysis of ionized outflow, the spectral synthesis code Cloudy [21] can be used to compare measured ionic column densities with simulated values from models created from a range of U_H and hydrogen column density (N_H) values [e.g., 19, 22, 23, 82].

A category of BAL quasars is known as iron low-ionized BAL (FeLoBAL) quasars, due to the identification of Fe II absorption troughs in their spectra. Recent studies of FeLoBALs include (but are not limited to) the study of a powerful FeLoBAL outflow in the quasar SDSS J135246.37+423923.5 [148]; the analysis of the FeLoBAL quasar Q0059-2735, whose outflow has shown signs of broad Si II absorption [80]; and a systematic study of the properties of FeLoBAL quasars using spectral synthesis code SimBAL [84, 85, 149].

We present the analysis of the UVES spectrum of the quasar SDSS J132139.86-004151.9 (hereafter, J1321-0041), which was retrieved from the Spectral Quasar Absorption Database (SQUAD) published by [10]. The data from SQUAD have 20 times higher spectral resolution than SDSS spectra, therefore lending themselves to a more detailed analysis. We conducted our analysis through the method described above in order to find $\dot{E}_k$ and to determine the outflow's potential ability to contribute to AGN feedback. Similar analyses of quasar outflows have been conducted in past works using spectra from SQUAD [e.g., 17, 18, 23].

This paper is structured as follows. Section 5.3 describes the observation of J1321-0041, as well as our data acquisition process. Section 5.4 describes the process through which we have found the outflow's ionic column densities, N_H, U_H, and n_e values. Section 5.5 presents the resulting energetics parameters R and $\dot{E}_k$. Section 5.6 discusses the outflow's potential ability to contribute to AGN feedback and compares it to other outflows that have been analyzed in the past. Section 5.7 summarizes and concludes the paper. For our analysis, we adopted a cosmology of $h = 0.696, \Omega_m = 0.286$, and $\Omega_\Lambda = 0.714$ [99].

5.3 Observations and data acquisition

J1321-0041 [J2000: RA=13:21:39.86, DEC: -00:41:51.9, z=3.119, 150] was observed with VLT/UVES on February 13, 2008, with a total exposure time of 22,800 seconds, as part of program 080.B-0445(A). [10] normalized the spectrum by the quasar's continuum and emission and added it to SQUAD. The quasar was also observed on 4 February 2000, 1 May 2000, and 16 March 2001 as part of the Sloan Digital Sky Survey (SDSS), with little to no time variability between observations. We co-added the SDSS spectra to scale the flux of the UVES spectrum shown in Figure 5.1 and to find the bolometric luminosity of the quasar. The co-added SDSS spectrum can be seen in Figure 5.2.

We have identified broad absorption line (BAL) outflow traveling at $v \approx -4100$ km s^{-1} with troughs of multiple ionic transitions in the UVES spectrum of J1321-0041, including C IV, Si IV, Si II, and Fe II. The velocity of the outflow was determined based on the deepest part of the Si II λ1808 absorption. The detection of Fe II absorption features puts this outflow in the class of FeLoBALs. The outflow is unusual, as its C II trough by itself adheres to the definition of a BAL [76], as its width is ~ 2300 km s^{-1}. Only relatively few such objects are described in the literature[80, 84]. The presence of multiple energy states of Fe II and Si II

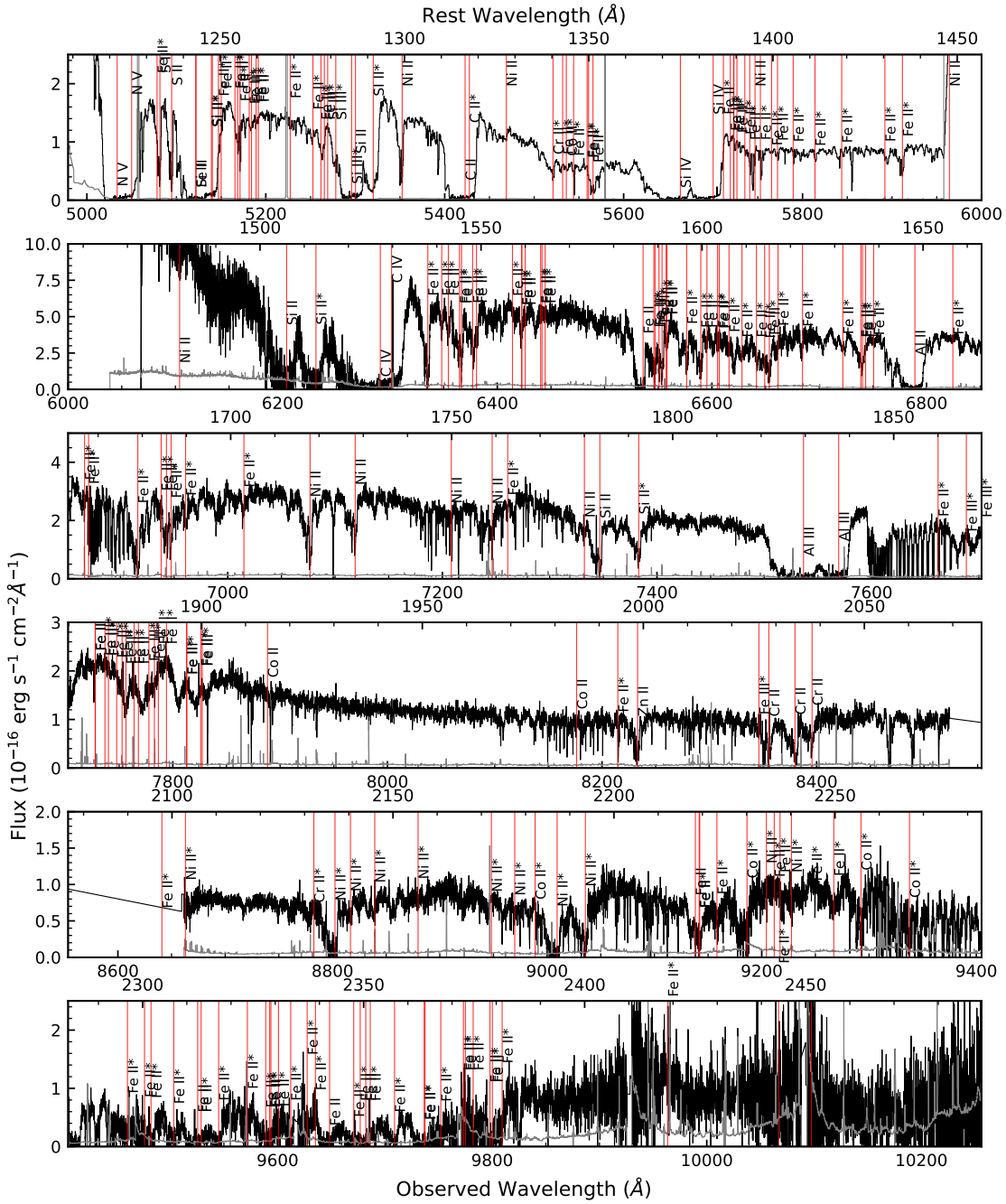

Figure 5.1 UVES spectrum of J1321-0041. Located absorption troughs and expected locations of absorption troughs from an outflow system, at $v \approx -4100$ km s^{-1}, are marked with red vertical lines. The flux has been scaled to match the flux of the SDSS spectrum at observed wavelength $\lambda = 6850$ Å.

Table 5.1 Fe II* lines that were used for the n_e analysis.

λ (Å)	Energy (cm^{-1})	$\log n_{crit}$ [cm^{-3}]
1628.160	667	4.4
1623.093	2430	4.5
1570.245	2837	4.6
1726.393	3117	4.6
1562.270	7955	4.7

* Columns show transition wavelengths, energies, and critical densities, $\log n_{crit}$.

have enabled us to estimate the outflow's n_e, R, and $\dot{M}$ values, and by extension, $\dot{E}_k$. The Fe II* transition lines used for this paper's analysis, and their associated energies, are shown in Table 5.1.

5.4 Analysis

5.4.1 Ionic column densities

The first step of our analysis was to find the column densities (N_{ion}) of the ions found in the outflow system. We converted the normalized UVES spectrum from wavelength space to velocity space using the systemic redshift of the quasar (see Figure 5.3), and measured the ionic column densities assuming an apparent optical depth (AOD) of a uniform and homogeneously covering outflow [107, 151].

The AOD method relates the intensity and optical depth as follows:

$$I(\lambda) = I_0(\lambda)e^{-\tau(\lambda)}, \tag{5.1}$$

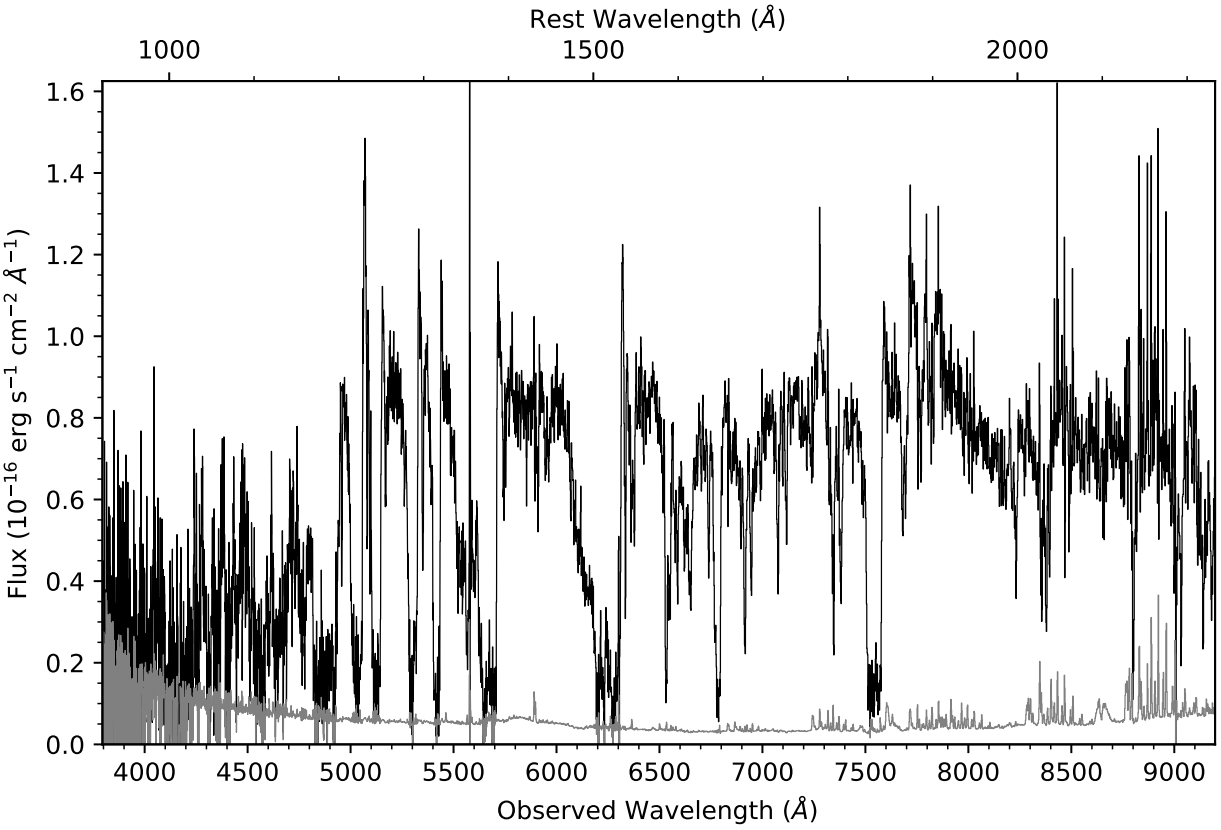

Figure 5.2 SDSS spectrum of J1321-0041 that was used to scale the continuum flux of the UVES spectrum and to calculate the quasar's bolometric luminosity. The flux is plotted in black and the error is plotted in gray.

where $I(\lambda)$ is intensity as a function of wavelength, $I_0(\lambda)$ is what the intensity would be without absorption, and $\tau(\lambda)$ is the optical depth. Normalizing a spectrum makes the process of finding the optical depth relatively easier, as it becomes a matter of relating the normalized intensity $I(\lambda)/I_0(\lambda)$ to $e^{-\tau(\lambda)}$. Finding the optical depth allows us to find the column density, as they are related as follows [151]:

$$\tau(v) = \frac{\pi e^2}{m_e c} f \lambda N(v), \tag{5.2}$$

where e is elementary charge (C), m_e is electron mass (kg), f is the oscillator strength of the ionic transition (unitless), λ is the wavelength of the transition (Å), and $N(v)$ is column density per unit velocity ($\mathrm{cm}^{-2}/\mathrm{km\ s}^{-1}$). The column density of an ion can be found by integrating $N(v)$ over the velocity range of the absorption trough. While this is a simple and straightforward method to estimating the ionic column density, it is limited to finding the lower limits when measuring column densities from saturated lines.

We identified the velocity range of the Fe II absorption to be $-4200\ \mathrm{km\ s}^{-1} \lesssim v \lesssim -4000\ \mathrm{km\ s}^{-1}$ (see bottom panel of Figure 5.3) and integrated over that range to find the ionic column densities of the outflow, as shown in Table 5.2. The red boundary was determined based on the red wing of the deepest absorption trough of Si II. The integration range was kept consistent among the different ions to allow direct comparison of different column densities. The Cr II lines that we identified are those of Cr II* λ1358.71 and λ2161.38. Despite the oscillator strength of the latter being three orders of magnitude larger ($f = 0.014$ vs. 2.3×10^{-5}), the depth of the former trough is deeper, suggesting that the absorption features may be contaminated (See Figure 5.3). Thus, we determined that we would be unable to reliably measure the column density of Cr II. We have identified two visible Co II* troughs, Co II* λ2260 and 2286, from which we have determined a lower limit of Co II column density. We note the reported column densities in Table 5.2 of ions with multiple energy states, such as

Table 5.2 Ionic column densities of the outflow of J1321-0041.

Ion	AOD	Adopted
C II	$31.8^{+0.9}_{-0.7}$	$> 31.8_{-4.5}$
C IV	$16.2^{+.3}_{-.2}$	$> 16.2_{-3.2}$
N V	$29.6^{+.5}_{-.5}$	$> 29.6_{-5.9}$
Al II	$.90^{+.02}_{-.02}$	$> .9_{-.2}$
Al III	$4.4^{+.1}_{-.1}$	$> 4.4_{-.9}$
Si II	486^{+5}_{-5}	$> 486_{-69}$
Si IV	$7.0^{+.2}_{-.1}$	$> 7.0_{-1.4}$
S II	131^{+2}_{-2}	$> 131_{-26}$
S IV	44^{+21}_{-4}	44^{+22}_{-8}
Fe II	590^{+30}_{-30}	590^{+110}_{-110}
Ni II	170^{+5}_{-4}	170^{+34}_{-34}
Co II	$1.16^{+.07}_{-.05}$	$> 1.2_{-0.2}$

* Column densities are shown in units of 10^{14} cm^{-2}.

Fe II and Ni II, which are the sum of several energy states. The column densities of both Fe II and Ni II are dominated by their resonance states. We also note that the Fe III transitions are marked in Figure 5.1 for completion, but they do not have associated discernible troughs. For the photoionization analysis to be described in Section 5.4.2, we added 20% of the column densities to their errors in quadrature to take into account systemic uncertainties, such as that of the modeling of the continuum, following the methodology of [7]. We note that the majority of the adopted values are lower limits, largely due to saturation of the absorption lines.

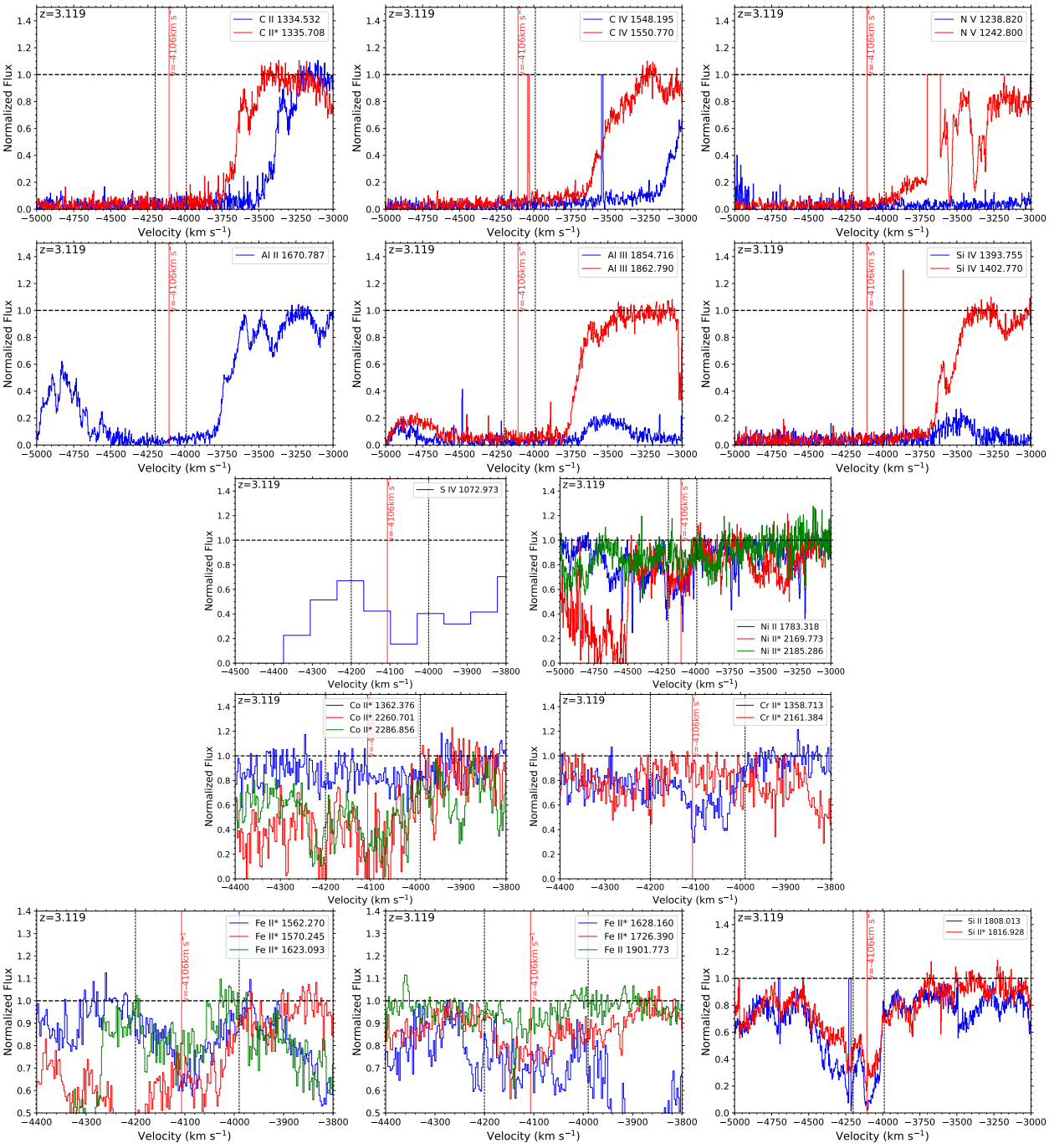

Figure 5.3 Normalized spectrum of J1321-0041, converted into velocity space. Troughs of individual ionic transitions are color coded, and the integration ranges used for column density calculations are marked by vertical dotted lines. The continuum is represented by a horizontal dashed line. All spectra shown are UVES spectra, except for that of the S IV absorption, which is based on the SDSS spectra due to wavelength range limitations. We note the stark contrast in the signal-to-noise ratio. The bottom three panels show the Fe II and Si II absorption, which were used to estimate n_e.

5.4.2 Photoionization analysis

We used the spectral synthesis code Cloudy [21] to find the best fitting values of the hydrogen column density (N_H) and the ionization parameter (U_H), by comparing modeled values of ionic column densities to the measured values shown in Table 5.2. Analyses using this method have been carried out in previous works as well [e.g., 17, 23]. As shown in Figure 5.4, Cloudy was used to create a grid of outflow models using a range of N_H and U_H values, with the measured ionic column densities serving as constraints to the parameters. Assuming solar metallicity and the spectral energy distribution (SED) of the quasar HE0238-1904 [hereafter, HE0238, 14], this results in the best fitting solution of $\log N_H = 21.73^{+0.39}_{-0.26}[\mathrm{cm}^{-2}]$ and $\log U_H = -1.74^{+0.69}_{-0.27}$. The SED of HE0238-1904 is the best empirically determined SED in the extreme UV, which most of the ionizing photons come from [14]. We note that this solution depends on the assumption that the column density of S IV is a measurement, an assumption we make as we find S IV to be relatively unsaturated. Setting the column density of S IV to be a lower limit results in an unbound lower limit of U_H. We note that the S IV trough is from the SDSS spectrum, as it was outside the wavelength range of the SQUAD spectrum.

5.4.3 Electron number density

Assuming collisional excitation (an assumption verified by Cloudy simulations), an outflow's electron number density can be found from the column density ratios between different energy states of ions [e.g., 89]. We used the troughs of Si II and Fe II that we found to be relatively unsaturated and free of contamination (see bottom panel of Figure 5.3) and overlaid the ratios between resonance and excited states of the ions with the relation between column density ratio and n_e calculated using the Chianti atomic database [version 9.0.1,

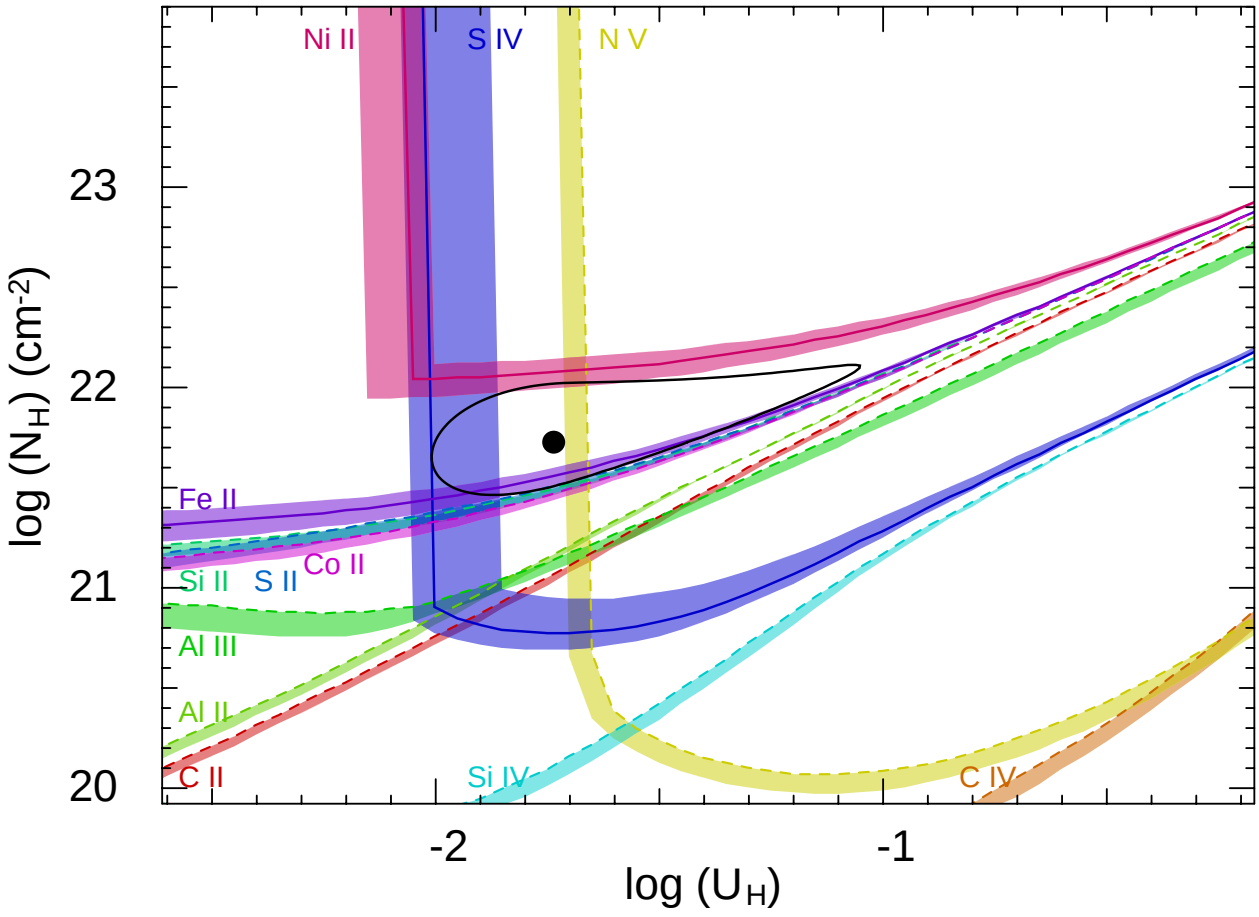

Figure 5.4 Plot of hydrogen column density ($\log N_H$) vs. ionization parameter ($\log U_H$), with constraints based on the measured ionic column densities shown in Table 5.2. Measurements are shown as solid curves, while the dashed curves show lower limits. The colored shades indicate the uncertainties in the constraints of the parameters based on the uncertainties in column density. The black dot shows the solution of $\log N_H$ and $\log U_H$ that best matches the column densities, while the black ellipse indicates the 1-σ error.

12, 13]. The Si II states were those with energies of $E(\mathrm{cm}^{-1}) = 0, 287$ and those of Fe II had $E(\mathrm{cm}^{-1}) = 0, 667, 2430, 2837, 3117, 7955$. The resulting $\log n_e$ values ranged from 2.9 to 4.2 (see Figure 5.6). We calculated the weighted mean of $\log n_e$, following the linear method described by [136]. For the uncertainty, we used:

$$\Delta \log n_e = \frac{|\log n_{e,ex} - \langle \log n_e \rangle|}{\sqrt{N}}, \tag{5.3}$$

where $\langle \log n_e \rangle$ is the weighted mean, $\log n_{e,ex}$ is the maximum (minimum) measured $\log n_e$ used when calculating the upper (lower) error, and N is the number of measured $\log n_e$ values. This resulted in $\log n_e = 3.45^{+0.26}_{-0.20}$. We note that the range of $\log n_e$ values is within 2-σ of the weighted mean.

We were also able to find troughs of Fe II* of energies $E = 385, 13474, 22637$, and 27620, which had smaller oscillator strengths than the troughs that had been used for this analysis (See Table 5.3). Despite the smaller oscillator strength values, the troughs are as deep as (or even deeper than) the troughs that have been used for the number density calculation (see bottom panels of Figures 5.3 and 5.5 for comparison.) This suggests that the troughs may have been contaminated by unidentified absorption features, making them unreliable indicators of Fe II* column density. Thus, we have excluded them from this calculation.

5.5 Results

With N_H, U_H, and n_e found (see Table 5.4), we could determine the distance of the outflow from the source based on the definition of U_H:

$$U_H \equiv \frac{Q_H}{4\pi R^2 n_H c}, \tag{5.4}$$

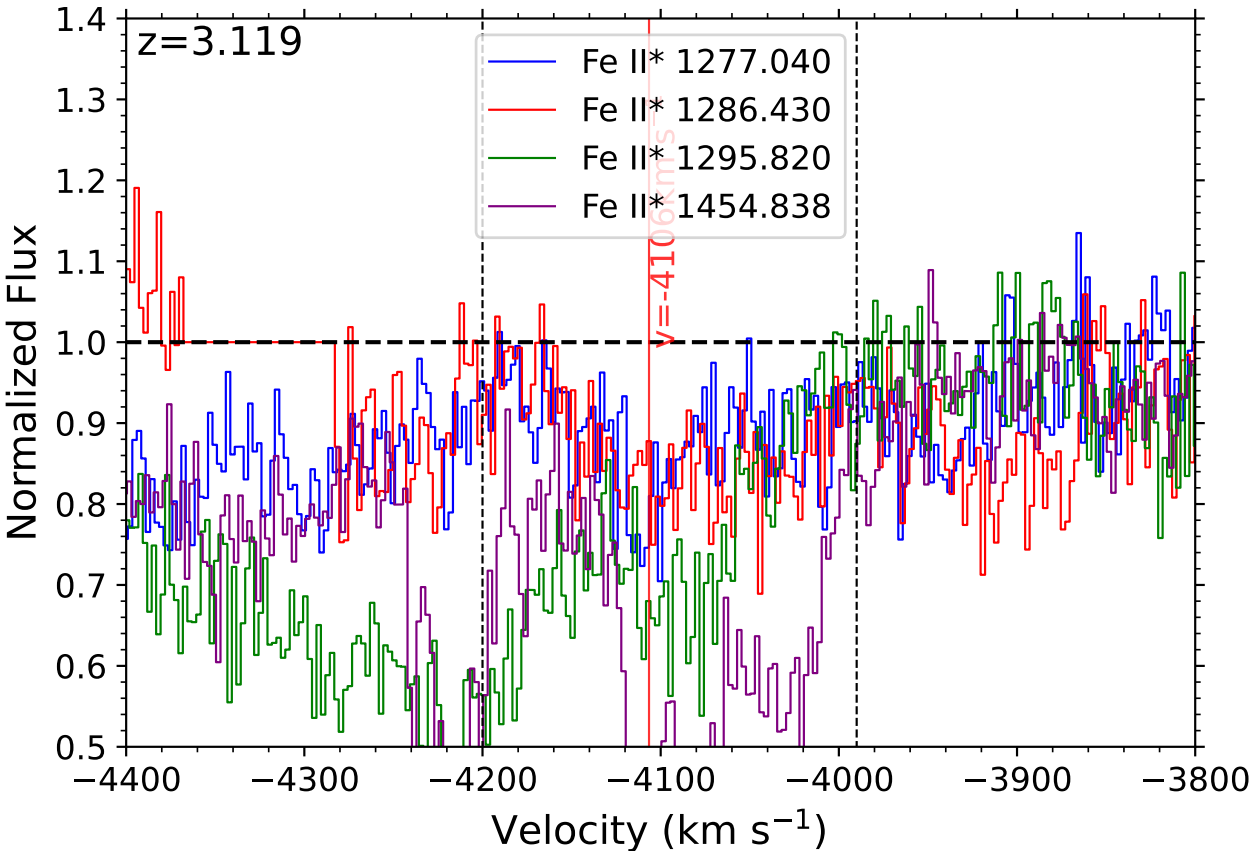

Figure 5.5 Fe II* absorption troughs that have been excluded from the calculation of $\log n_e$.

Table 5.3 Oscillator strengths of Fe II lines found in the spectrum.

Energy (cm^{-1})	λ (Å)	f
0	1901.773	6.0×10^{-5}
667	1628.160	1.8×10^{-2}
2430	1623.093	8.8×10^{-3}
2837	1570.245	4.0×10^{-2}
3117	1726.393	2.2×10^{-2}
7955	1562.270	5.2×10^{-2}
385	1277.040	2.7×10^{-6}
13474	1286.430	3.1×10^{-4}
22637	1295.820	4.0×10^{-5}
27620	1454.838	2.1×10^{-3}

* The transitions used in the analysis and those that are not are divided by the horizontal line.

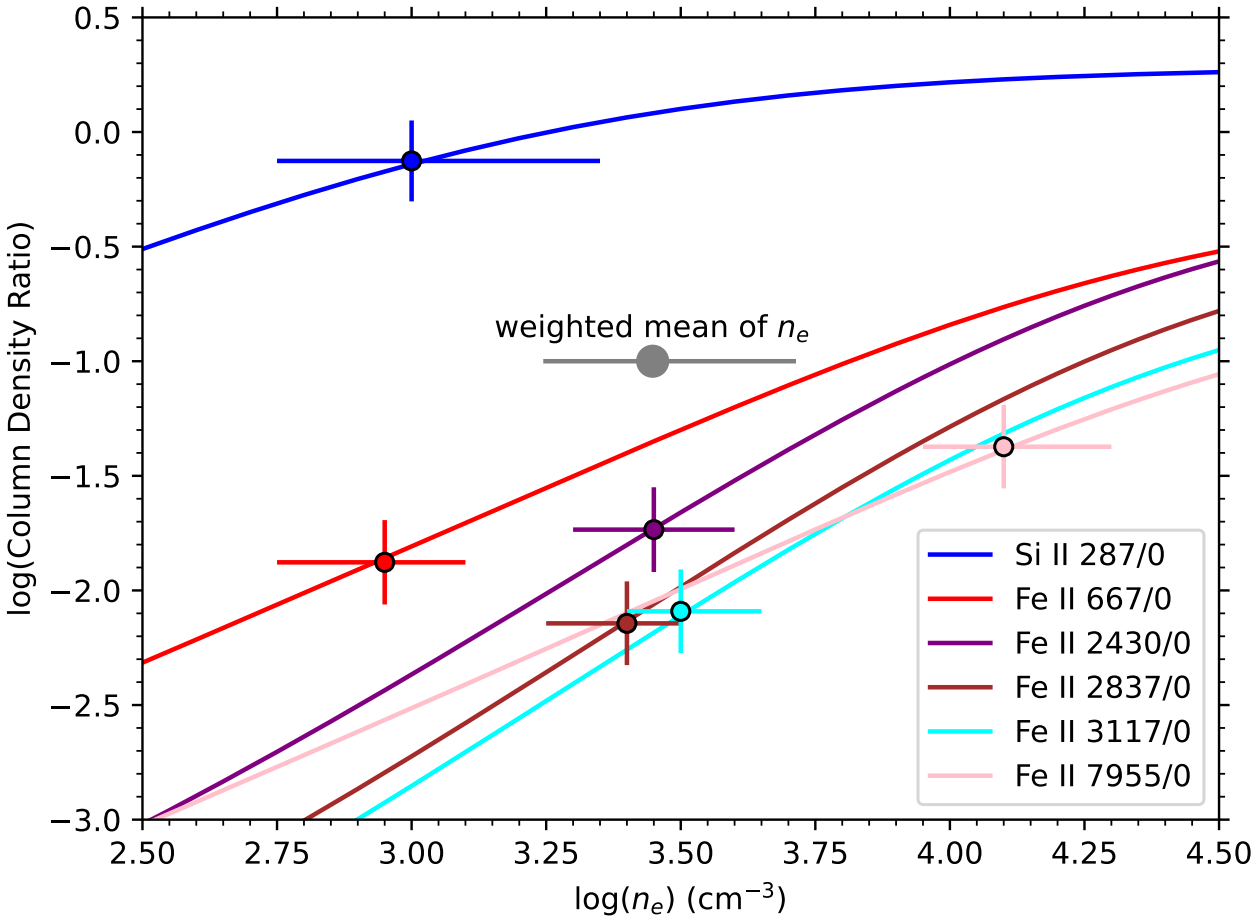

Figure 5.6 Measured column density ratios of different energy states of Si II and Fe II versus electron number density ($\log n_e$), calculated using CHIANTI[12, 13]. The color-coded curves are the theoretical relationships between ratio vs. n_e, while the dots indicate the measured ratios and associated $\log n_e$ values. The weighted mean of $\log n_e = 3.45^{+0.26}_{-0.20}$ is indicated with a gray dot.

Table 5.4 Physical parameters of the outflow of J1321-0041.

Parameter	Value
$\log U_H$	$-1.74^{+0.69}_{-0.27}$
$\log N_H$ [cm^{-2}]	$21.73^{+0.39}_{-0.26}$
$\log n_e$ [cm^{-3}]	$3.45^{+0.26}_{-0.20}$
R (pc)	2500^{+1000}_{-1400}
$\dot{M}$ ($M_\odot$ yr^{-1})	1600^{+2600}_{-1000}
$\dot{E}_k$ (10^{45} erg s^{-1})	$8.4^{+13.7}_{-5.4}$
$\log \dot{E}_k$ [erg s^{-1}]	$45.92^{+0.42}_{-0.45}$
$\dot{E}_k/L_{Bol}$ (%)	$4.8^{+8.0}_{-3.1}$

* n_e calculation has been done with Chianti, assuming temperature T=10,000 K.

where Q_H is the emission rate of Hydrogen ionizing photons, R is the outflow's distance from the quasar, and n_H is the Hydrogen number density. Following the approximation of $n_e \approx 1.2 n_H$ for highly ionized plasma [83], we could calculate the value of R once Q_H was found.

In order to find Q_H, and by extension, the bolometric luminosity L_{Bol}, we scaled the SED of HE0238 to match the continuum flux at observed wavelength $\lambda = 5850$ Å, $F_\lambda = 8.25 \pm 0.64 \times 10^{-17}$ erg s^{-1} cm^{-2}. We then integrated the SED for energies above 1 Ryd, resulting in $Q_H = 9.6 \pm 0.7 \times 10^{56}$ s^{-1}, and $L_{Bol} = 1.72 \pm 0.13 \times 10^{47}$ erg s^{-1}. The resulting outflow distance was $R = 2.5^{+1.0}_{-1.4}$ kpc.

5.6 Discusssion

5.6.1 AGN Feedback Contribution

An outflow's kinetic luminosity must be at least $\sim 0.5\%$ of the quasar's Eddington luminosity in order to contribute to AGN feedback [2, 58]. Finding this ratio requires both the kinetic luminosity, $\dot{E}_k$, and Eddington luminosity, L_{Edd}. A quasar's L_{Edd} value is typically found by measuring the width of an emission feature, such as that of C IV or Mg II, and estimating the mass of the black hole [123, 138, 139]. However, as can be seen in Figure 5.1, the spectrum of J1321-0041 lacks a prominent emission feature which we could use to make such an estimate. Therefore, we used L_{Bol} as described in Section 5.5 as a substitute metric, assuming that $L_{Edd} \approx L_{Bol}$, as this has been the case for several quasars that have been analyzed via this method [e.g., 17, 18]. We advise caution in taking this assumption at face value, as it has shown to not always be the case for FeLoBALQs [e.g. 149].We assumed that the geometrical shape of the outflow was that of an incomplete spherical shell, and found the mass flow rate:

$$\dot{M} \simeq 4\pi\Omega R N_H \mu m_p v, \tag{5.5}$$

where $\Omega = 0.2$ is the global covering factor, $\mu = 1.4$ is the mean atomic mass per proton, m_p is proton mass, and v is outflow velocity [6, 114]. The global covering factor 0.2 is adopted based on the $\sim 20\%$ ratio of quasars in which C IV BALs are found [37]. Despite the relative rarity of low-ionized BALs with troughs such as Si II or C II, it is likely that quasars with such LoBALs are BALQSOs at a specific line of sight (See [71] for a full discussion). We then calculated the kinetic luminosity ($\dot{E}_k = \frac{1}{2}\dot{M}v^2$), resulting in $\dot{E}_k = 8.4^{+13.2}_{-5.3} \times 10^{45}$ erg s^{-1}. The ratio between the kinetic luminosity and bolometric luminosity is $\dot{E}_k/L_{Bol} = 4.8^{+7.7}_{-3.1}\%$, which would be sufficient to contribute to AGN feedback (see Table 5.4 for a full summary

of the parameters).

5.6.2 Comparison with other outflows

The n_H value of the J1321-0041 outflow was found mainly by examining the ratios between the Fe II excited and resonance state column densities. This has been done in past studies as well [e.g., 19, 38]. The n_e values from the different ratios agree within ~ 0.5 dex with the mean (see Figure 5.6) and combined with the previous outflow analyses, this demonstrates that Fe II is an effective probe for n_H and outflow distance.

In previous analyses of FeLoBALs based on high resolution VLT/UVES data, the distance R has been measured to be within the range of 1 kpc $\lesssim R \lesssim$ 67 kpc [e.g., 17, 19, 23]. The distance of the J1321-0041 outflow from its source is $R \approx 2500$ pc, which is well within this range.

As previously mentioned, there have been studies analyzing extreme FeLoBALs in the past. [80] analyzed the physical conditions of the FeLoBAL of the quasar Q0059-2735, which had a C IV width of $\sim 25,000$ km s^{-1}, roughly twice as wide as the C IV width of J1321-0041 ($\sim 10,000$ km s^{-1}) found in its SDSS spectrum. [84] studied a larger sample of FeLoBALs, some of which have extreme blending in their absorption troughs. The presence of unblended absorption features in the J1321-0041 spectrum enabled us to conduct a precise analysis of the physical parameters of the outflow system.

5.7 Summary and conclusion

We have identified an FeLoBAL outflow system in the VLT/UVES spectrum of the quasar SDSS J1321-0041. Through the measurement of ionic column densities and photoioniza-

tion analysis, we determined the Hydrogen column density and ionization parameter of the outflow (see Figure 5.4 and Table 5.4).

The presence of Fe II and Si II absorption trough enabled us to find the electron number density n_e by using CHIANTI to relate their column density ratios to estimates of n_e. This allowed us to determine the outflows distance from its central source, kinetic luminosity, and the ratio between kinetic luminosity and the quasar's bolometric luminosity ($\dot{E}_k/L_{Bol} = 4.8^{+8.0}_{-3.1}$). Assuming $L_{Bol} \approx L_{Edd}$, the value of $\dot{E}_k$ is above the required threshold to contribute to AGN feedback.

Acknowledgements

We acknowledge support from NSF grant AST 2106249, as well as NASA STScI grants AR-15786, AR-16600, and AR-16601.

Chapter 6

BAL Outflow in Quasar B0254-3327B: Analysis and Comparison with Other Extreme UV Outflows

Foreword

This chapter is based on the published paper "*BAL Outflow in Quasar B0254-3327B: Analysis and Comparison with Other Extreme UV Outflows*" [22]. I led the project by analyzing the data, doing calculations, creating the figures, and writing the paper.

6.1 Abstract

We have identified a broad absorption line (BAL) outflow in the HST/STIS spectrum of the quasar QSO B0254-3327B at velocity $v = -3200$ km s^{-1}. The outflow has absorption troughs from ions such as Ne VIII, Na IX, Si XII, and Ne V. We also report the first detection of S XIV absorption troughs, implying very high ionization. Via measurement of the ionic column densities, photoionization analysis, and determination of the electron number density of the outflow, we found the kinetic luminosity of the outflow system to be up to $\sim 1\%$ of the

quasar's Eddington luminosity, or $\sim 5\%$ of the bolometric luminosity, making it a potential contributor to AGN feedback. A solution with two ionization phases was needed, as a single phase was not sufficient to satisfy the constraints from the measured ionic column densities. We find that the ionization parameter of the very high-ionization phase of the outflow is within the expected range of an X-ray warm absorber. We also examined the physical properties of the outflow of Q0254-334 along with previously studied extreme UV outflows, with a total sample of 24 outflow systems, finding a weak negative correlation between outflow velocity and distance from the central source, with larger distances corresponding to slower velocities. The very high-ionization phase of the Q0254-334 outflow has one of the highest ionization parameters of UV absorption outflows to date, which we attribute to the presence of S XIV.

6.2 Introduction

Quasar absorption outflows are often invoked as likely contributors to active galactic nucleus (AGN) feedback [e.g. 34–36, 53, 145]. They are detected via blueshifted absorption troughs in the rest frame of $\lesssim 40\%$ of quasars [e.g., 37, 38, 88, 116, 152]. In order to contribute to AGN feedback, outflow systems theoretically require a kinetic luminosity ($\dot{E}_k$) of at least $\sim 0.5\%$ [58] or $\sim 5\%$ [53] of the quasar's luminosity, which we interpret to be the Eddington luminosity (L_{Edd}) following the reasoning described by [2], as opposed to the bolometric luminosity (L_{Bol}). Past studies have found outflows that fit one or both of these criteria [e.g. 6, 17, 18, 23, 82, 84, 89, 90, 131, 148].

In order to find the value of $\dot{E}_k$, it is important to find the mass flow rate ($\dot{M}$), a method for which involves finding the electron number density (n_e) and ionization parameter (U_H) to measure the distance (R) of the outflow from the central source [92]. Multiple quasar

outflows have been analyzed via this method [e.g. 19, 23, 93, 95]. For ionized outflows, the ionization parameter can be determined by measuring the column densities of ions, and comparing them with simulated values based on a range of U_H and hydrogen column density (N_H). Multiple outflow analysis studies have been conducted using the spectral synthesis code Cloudy [21] for this method. [e.g. 7, 19, 23, 82].

This paper presents the analysis of the absorption outflow of the quasar QSO B0254-3327B (hereafter Q0254-334), using the method described above, based on HST/STIS observational data, ultimately finding the ratio between $\dot{E}_k$ and L_{Edd}.

The paper is structured as follows. Section 6.3 describes the observation and data acquisition of Q0254-334; section 6.4 discusses the process of finding the ionic column densities, N_H, U_H, and n_e of the outflow; section 6.5 shows our analysis results of whether the outflow's kinetic luminosity is sufficient to contribute to AGN feedback, and compares our results with studies of other outflows; and section 6.6 concludes and summarizes the paper. In our analysis, we adopted a cosmology of $h = 0.696, \Omega_m = 0.286$, and $\Omega_\Lambda = 0.714$ [99]. We used the Python astronomy package Astropy [100, 101] for our cosmological calculations. We also used Scipy [153], Numpy [154], and Pandas [v1.2.4, 155, 156] for the majority of our numerical computations, as well as Matplotlib [157] for plotting our figures.

6.3 Observation and Data Acquisition

Q0254-334 (J2000; RA=02:56:47.84, DEC=-33:15:26.16, z=1.863) was observed with HST/STIS on 17 February, 2001 as part of the program SNAP 8681, and on 4 March, 2001 as part of the program GO 8569, with the G230L and G140L gratings respectively. Prior to this, it was also observed with HST/FOS in 1994. Due to the limited wavelength range of the FOS data relative to that of STIS, we have focused on the STIS data for the

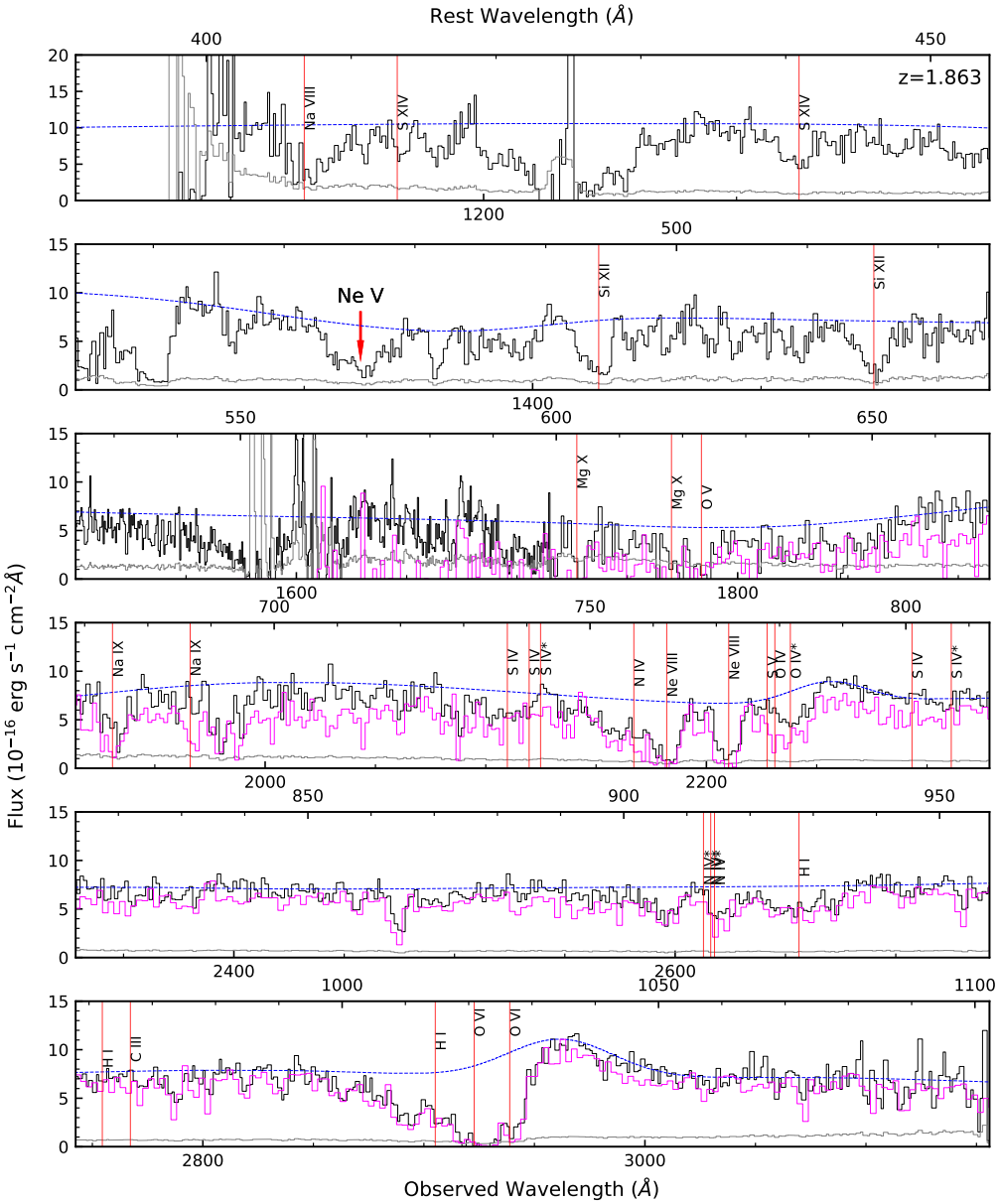

Figure 6.1 Co-Added STIS spectrum (black) and FOS spectrum (purple) of Q0254-334. The absorption features of the outflow system ($v \approx -3200$ km s^{-1}) are marked with red vertical lines, with the Ne V multiplet emphasized with a red arrow. The continuum and emission model is plotted as a blue dashed curve. Note that the continuum flux has risen between 1993 and 2001 in observed wavelengths up to $\sim$ 2100Å, while at longer wavlengths, the variability is nearly indistinguishable.

purpose of this analysis. After retrieving the data from the Mikulski Archive for Space Telescopes, we have co-added the two STIS spectra, and corrected the combined spectrum for galactic reddening and extinction with $E(B-V) = 0.0205$ [104], and the extinction model by [135]. The co-added and dereddened spectrum of the two observations, covering observed wavelengths 1138.6–3156.6Å, along with the FOS spectrum, is shown in Figure 6.1.

We have identified a broad absorption line (BAL) outflow system at $v = -3200$ km s^{-1}, with its ionic absorption troughs marked by red vertical lines in Figure 6.1. Troughs exist of species such as Ne VIII, Na IX, and Si XII, as well as excited state transitions such as O IV* and Ne V*. [9] define a BAL in the extreme UV range as a continuous absorption feature with normalized flux $I \leq 0.9$ over a width of $\Delta v \gtrsim 1500$ km s^{-1}, at least -3000 km s^{-1} blueward of the center of emission. We have verified that the outflow is a BAL outflow by confirming the width of the Si XII λ499.406 and Ne VIII λ780.324 troughs (see Figure 6.2). The normalized flux was found by modeling the quasar's continuum via a spline model that gave the minimum possible continuum above the absorption, and the most prominent emission features (e.g. O VI) with Gaussians. The presence of the Ne V* feature allowed us to find the value of n_e, as shown in Section 6.4.2.

6.4 Analysis

6.4.1 Ionic Column Densities

As the ionic column densities (N_{ion}) of the outflow are crucial in finding the physical properties of the outflow, we used two different methods to find them based on the absorption troughs: the apparent optical depth (AOD) method in which we assume uniform and homogeneous covering [107]; and the partial covering (PC) method in which we include a covering

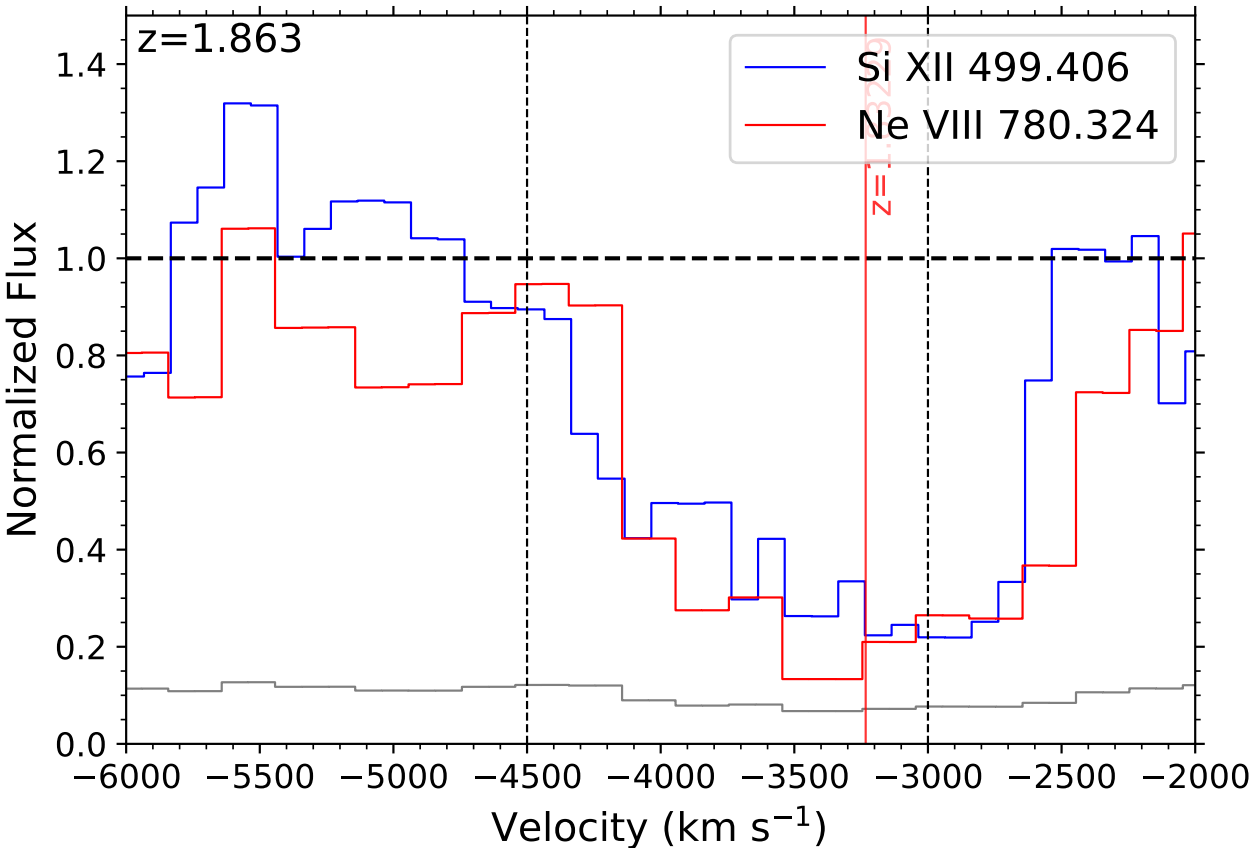

Figure 6.2 Normalized flux in the region of the Si XII λ499.406 and Ne VIII λ780.324 absorption. The dashed horizontal line shows the continuum level, and the dotted vertical lines show the region between $v = -4500$ and -3000 km s^{-1}, which represents the range for the EUV BAL criteria, as defined by [9]. The normalized flux for Si XII falls below 0.9 in this region. While the Ne VIII normalized flux lies above 0.9 at -4500 km s^{-1}, it is within uncertainty range to fall below the threshold. To demonstrate, the error in the Ne VIII flux is shown in gray.

factor $C < 1$ [108–110].

The AOD method allows us to find upper limits and lower limits of ionic column densities with its relative simplicity, while the PC method lets us find more accurate measurements of ions with doublet features [e.g. 18, 111, 112, 118]. As done by [17] for the quasar J024221.87+004912.6, we selected the appropriate method for computing the column density of each ion.

The AOD method involves the following relation between intensity and optical depth [107, 151]:

$$I(\lambda) = I_0(\lambda)e^{-\tau(\lambda)} \tag{6.1}$$

where $I(\lambda)$ is the intensity as a function of wavelength, $I_0(\lambda)$ is the intensity without absorption, and τ is the optical depth. Finding the optical depth enables computation of the column density, as they have the following relation:

$$\tau(v) = \frac{\pi e^2}{m_e c} f\lambda N(v) \tag{6.2}$$

where $\tau(v)$ is the optical depth as a function of velocity, e is the elementary charge, m_e is the mass of an electron, and $N(v)$ is the column density per unit velocity. Integrating $N(v)$ over the velocity range of an ion's absorption trough results in the ion's column density.

As mentioned above, the PC method involves a covering factor $C < 1$, which follows the relation shown in the equations below [112]:

$$I_R(v) - [1 - C(v)] = C(v)e^{-\tau(v)} \tag{6.3}$$

$$I_B(v) - [1 - C(v)] = C(v)e^{-2\tau(v)} \tag{6.4}$$

where $I_R(v)$ and $I_B(v)$ are the intensities at the red (longer wavelength) and blue (shorter

wavelength) troughs of a doublet transition, $C(v)$ is the covering factor as a function of velocity, and τ is the optical depth.

For each ion, we converted the spectrum from wavelength space to velocity space, using the redshift of the quasar and the wavelengths of the ionic transition lines (see Figures 6.3,6.4). We then chose integration ranges for each ion that covered visible absorption features and minimized blending effects with other lines. For instance, the O VI doublet had heavy blending between the red and blue troughs (see Figure 6.3f). We thus chose a range where the overlap between the red and blue troughs would be minimized and computed a lower limit to the column density with the AOD method. As there were no discernible absorption troughs of Ly γ, C III, and S IV*, we measured their AOD column density with integration range $v \approx -4500$ to -2000 km s^{-1} to match the Ne VIII width, and treated them as upper limits. Due to the severe blending in the multiplet of S IV $\lambda\lambda 744.904, 748.393$ and S IV* $\lambda 750.221$ (see panel 4 of Figure 6.1), we were unable to pinpoint the column density of the resonance state S IV 0 from this trough. However, as there was no discernible absorption trough of S IV $\lambda 809.656$, we were able to find an upper limit of its column density. Similarly, the trough of O IV $\lambda 787.711$ blended with O IV* $\lambda 790.190$, and potentially with the neighboring S V $\lambda 786.468$. As such, we were unable to find the column density of the resonance state O IV 0, and could only find a lower limit of the O IV* column density. We were also limited to finding a lower limit of the Ne VIII column density based on an AOD measurement due to the saturation of the doublet troughs. In the doublet of S XIV, we determined the red trough of S XIV $\lambda 446$ to be contaminated, due to the visible blue-ward absorption compared to the blue trough $\lambda 418$ (see Figure 6.4 plot c). Due to this limitation, we measured the AOD column density of S XIV based on the blue trough. We determined that it was safe to treat this column density as a measurement, due to its shallower depth relative to similarly ionized troughs with comparable oscillator strengths (e.g. Si XII).

The integrated column densities are shown in Table 6.1. The rightmost column shows the values adopted for the photoionization solution described in Section 6.4.3. The errors have been propagated from the error in the flux, and a conservative 20% error has been added in quadrature to the adopted column density errors to account for the uncertainty in the continuum level due to the subjectivity of the model [7]. This uncertainty is demonstrated in the column density calculation of O IV* based on the different continuum models shown in Figure 6.5. The maximum, minimum, and intermediate continuum fits in the region are shown as blue, red, and purple dashed lines respectively. The O IV* absorption is marked with a gray vertical line. The AOD measurement of the O IV* column density is $28.0^{+2.8}_{-2.0} \times 10^{14}$ cm^{-2} for the intermediate continuum, while the higher and lower continuum levels yield results of $32.6^{+2.8}_{-2.0} \times 10^{14}$ cm^{-2} and $24.4^{+2.8}_{-2.0} \times 10^{14}$ cm^{-2}. This indicates a $\pm$15% difference in column density depending on continuum level, and a 20% difference when including the individual errors. Note that the column density of Ne V was based on a Gaussian fit of the troughs of its different energy states, which we further describe in Section 6.4.2.

6.4.2 Ne V Gaussian Fitting

As seen in Figure 6.6 (top panel), the Ne V multiplet of the outflow is blended into a singular trough. The involved transitions are Ne V 0 (λ = 480.415 Å), Ne V* 411 (λ = 481.227, 481.366, 481, 371 Å), and Ne V* 1109 (λ = 482.990, 482.994 Å). To remedy the blending, we modeled the individual energy states of Ne V by fitting Gaussian profiles for each of the expected absorption features, and running a best fit algorithm to best match the data. The free parameters used were the optical depth of the ground state Ne V trough, the width of the trough, and $\log n_e$. We assumed the AOD scenario, and adjusted the depths of the excited state troughs to match the oscillator strengths of the transition lines, as well as the abundance ratios N(Ne V*)/N(Ne V 0) from the Chianti 9.0.1 atomic database [12, 13].

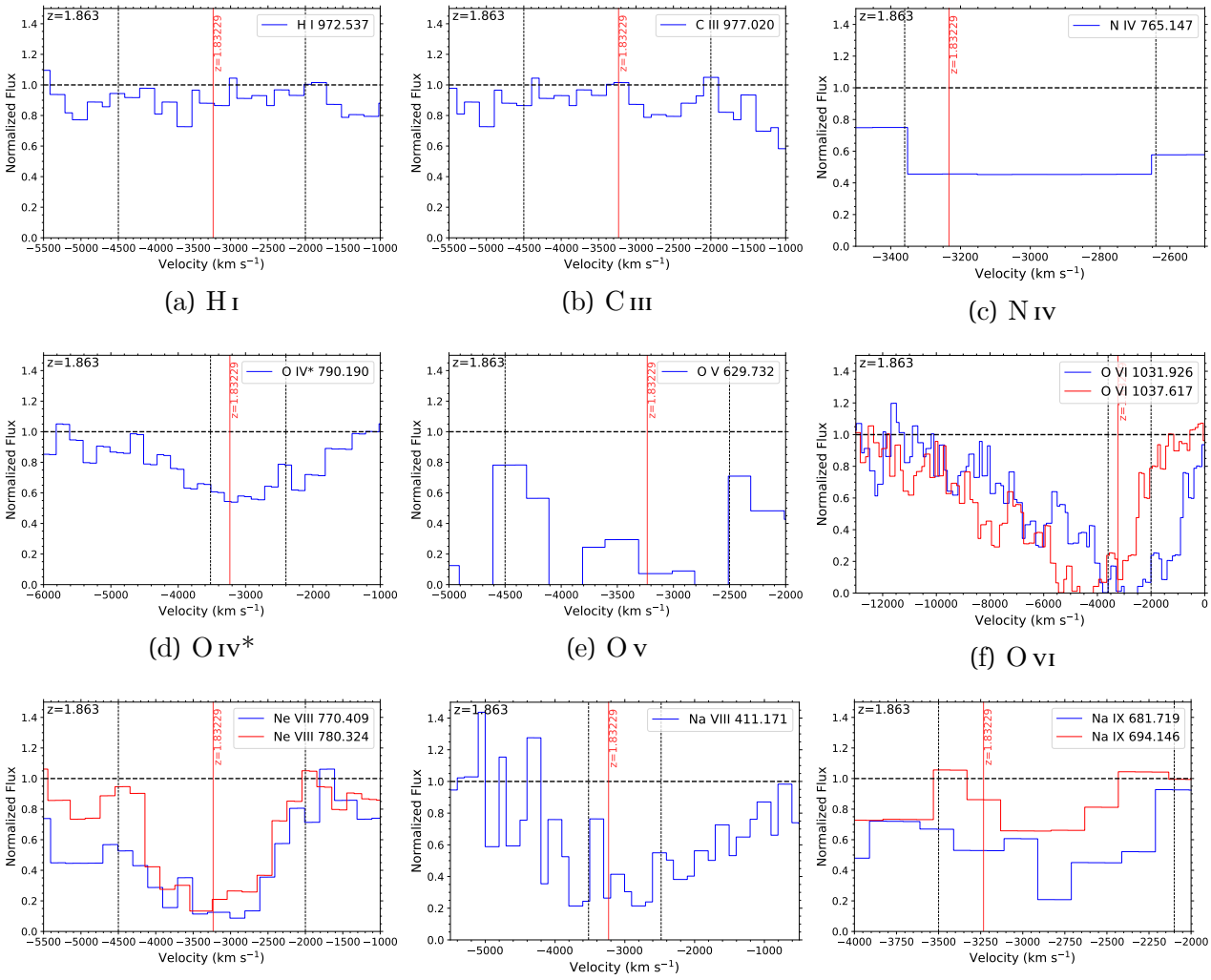

(a) H I (b) C III (c) N IV

(d) O IV* (e) O V (f) O VI

(g) Ne VIII (h) Na VIII (i) Na IX

Figure 6.3 Absorption troughs of the Q0254-334 outflow plotted in velocity space. The velocity of the outflow at $z = 1.89229$ is marked with red vertical lines. The integration range used to calculate the column densities is marked with dotted vertical lines, while the continuum level is indicated by the dashed horizontal line.

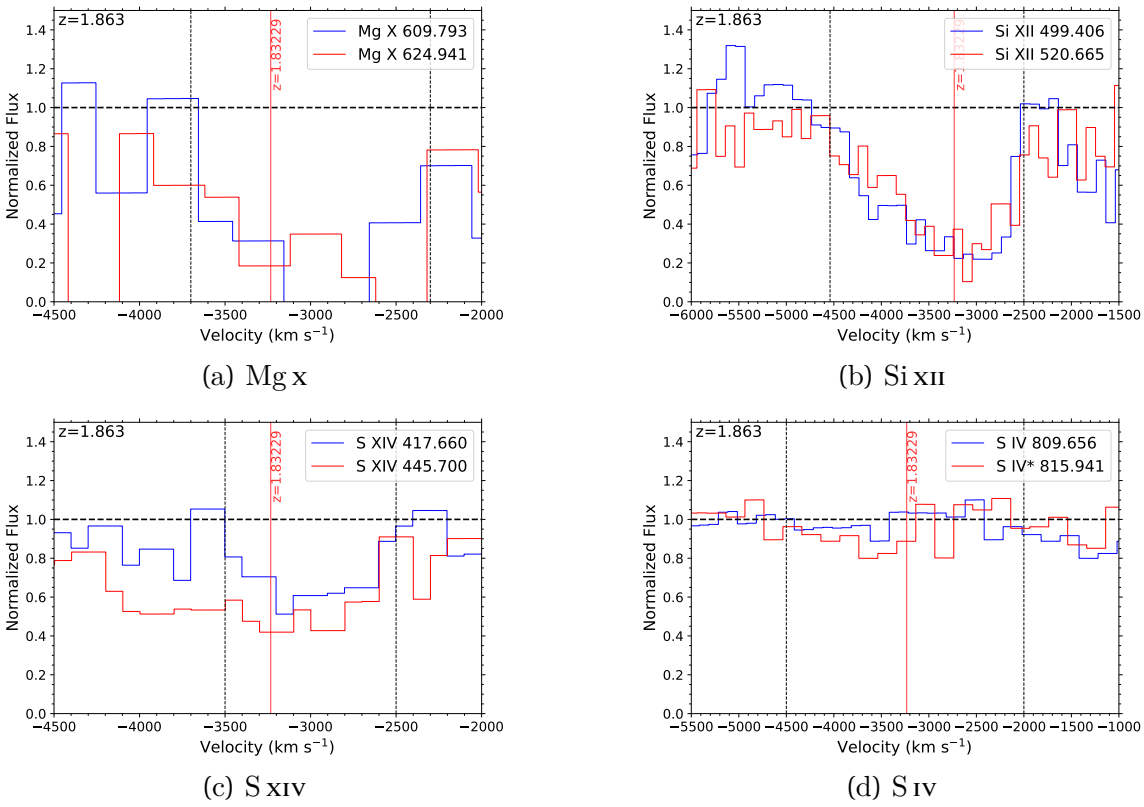

(a) Mg x (b) Si xii

(c) S xiv (d) S iv

Figure 6.4 Absorption troughs of Mg x, Si xii, S xiv, and S iv* in the outflow of Q0254-334. Format and notation are identical to those of Figure 6.3.

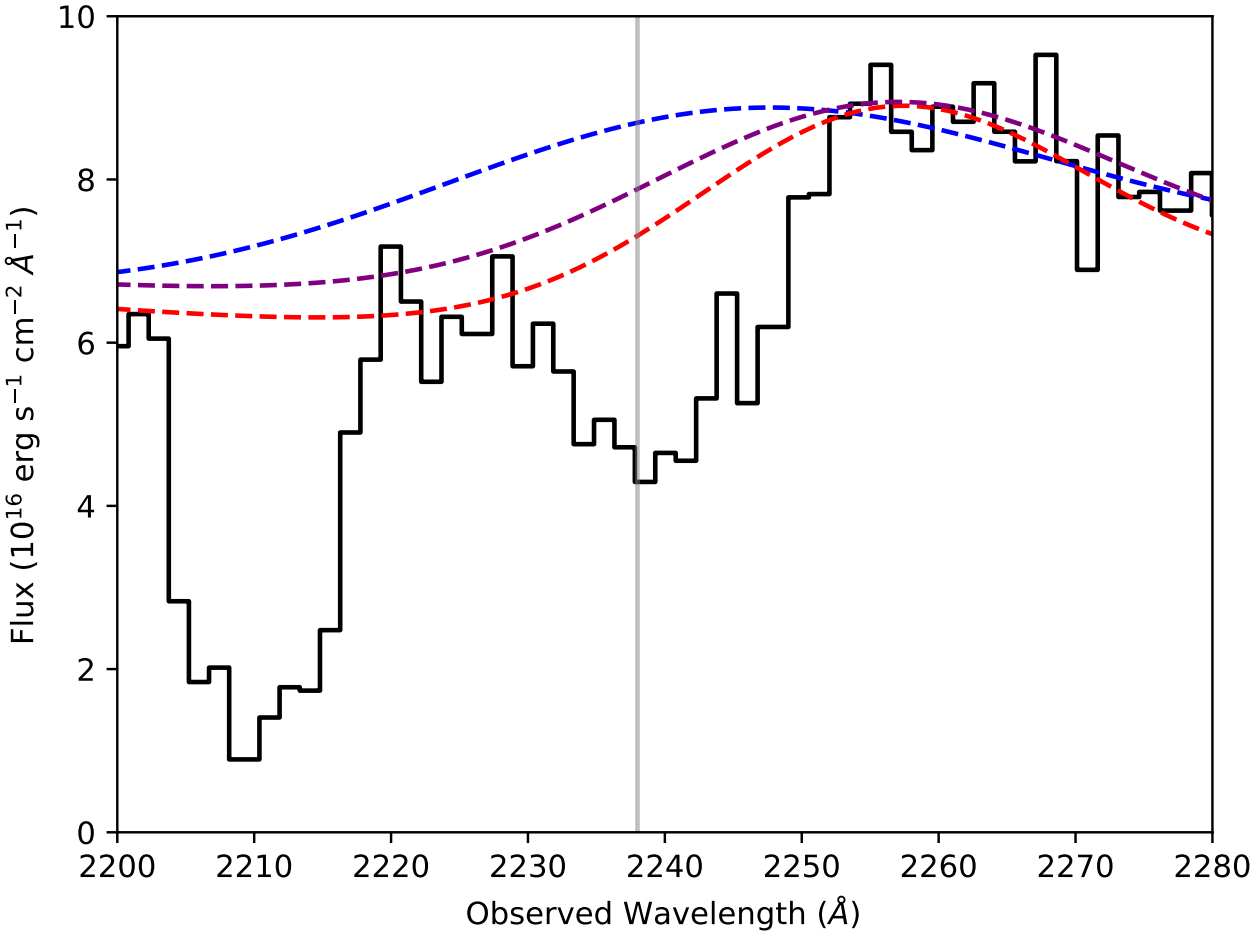

Figure 6.5 The O IV region of the Q0254-334 spectrum showing the possible continuum fits which lead us to use 20% error bars on the column densities (See text).

Table 6.1 Q0254-334 outflow column densities from STIS observations. The numbers next to the Ne v* excited states denote the energies in cm^{-1}. The values are in units of 10^{14} cm^{-2}.

Ion	AOD	PC	Adopted
H I	38^{+7}_{-4}		$< 38^{+11}$
C III	$1.8^{+0.3}_{-0.2}$		$< 1.8^{+0.4}$
N IV	$4.6^{+0.6}_{-0.4}$		$> 4.6_{-1.0}$
O IV*	$28.0^{+2.8}_{-2.0}$		$> 28.0{-}6.0$
O V	50^{+8}_{-5}		$> 50_{-11}$
O VI	114^{+10}_{-4}		$> 114_{-23}$
Ne V total	196^{+22}_{-22}		196^{+45}_{-45}
Ne V 0	106^{+18}_{-18}		
Ne V* 411	72^{+12}_{-12}		
Ne V* 1109	18^{+3}_{-3}		
Ne VIII	229^{+25}_{-10}		$> 229_{-47}$
Na VIII	$29^{+11.6}_{-2.9}$		$> 29_{-6.6}$
Na IX	$38.2^{+8.4}_{-7.2}$	$48.2^{+6.2}_{-6.1}$	$48.2^{+11.5}_{-11.3}$
Mg X	366^{+87}_{-46}		$> 336_{-87}$
Si XII	360^{+57}_{-22}		$> 360_{-75}$
S IV total	27^{+2}_{-2}		$< 27^{+5}$
S IV 0	$7.2^{+0.9}_{-0.6}$		
S IV*	20^{+3}_{-2}		
S XIV	198^{+20}_{-13}		198^{+45}_{-42}

We assumed a temperature of 10,000 K in our CHIANTI computations. A similar process of finding n_e via the ratios between the different energy states of Ne V is demonstrated by [82], and is especially illustrated in their Figure 3.

We have found that the optical depth $\tau = 0.69 \pm 0.11$, FWHM $= 2360 \pm 170$ km s^{-1} and $\log n_e = 3.6 \pm 0.1$ [cm $^{-3}$]. Using the modeled troughs, we have calculated the column densities of each energy state of Ne V, as shown in Table 6.1. Since the value of n_e is crucial in finding the distance of the outflow from the central source (as described in Section 6.5.1), we later ran a simulation with the spectral synthesis code CLOUDY [version c17.00, 21] in order to verify the temperature of the outflow. With the two-phase high-ionization solution later described in Section 6.4.3 as our input parameters, the simulation yielded a temperature of $T \approx 27,000$ K. Calculating the electron number density with this temperature yielded $\log n_e = 4.0^{+0.1}_{-0.1}$. As such, we adopted this value of $\log n_e$ for the purpose of our analysis. The total column density of Ne V based on this computation is in agreement with the value based on the $T = 10,000$ K assumption.

As an alternate method of modeling the blended trough of the Ne V multiplet, we used the trough of Si XII λ499 as a template to create a profile of two blended Gaussians (see Figure 6.7). We then ran a best fit algorithm to model the absorption of each energy state, leaving the width of the profile as a fixed parameter (see Figure 6.6 bottom panel). This resulted in an electron number density of $\log n_e = 4.3 \pm 0.1$ [cm^{-3}], which is only ~ 0.3 dex higher than the simple Gaussian fitting shown in Section 6.4.2. We report the physical properties calculated based on this value of n_e in Table 6.5.

While the difference in the electron number density shifts the kinetic luminosity to lower values relative to those shown in Table 6.3, the kinetic luminosities remain in agreement within error. We thus focus on the results based on the Gaussian model throughout the paper. The parameters are described in further detail in Sections 6.5.1 and 6.5.

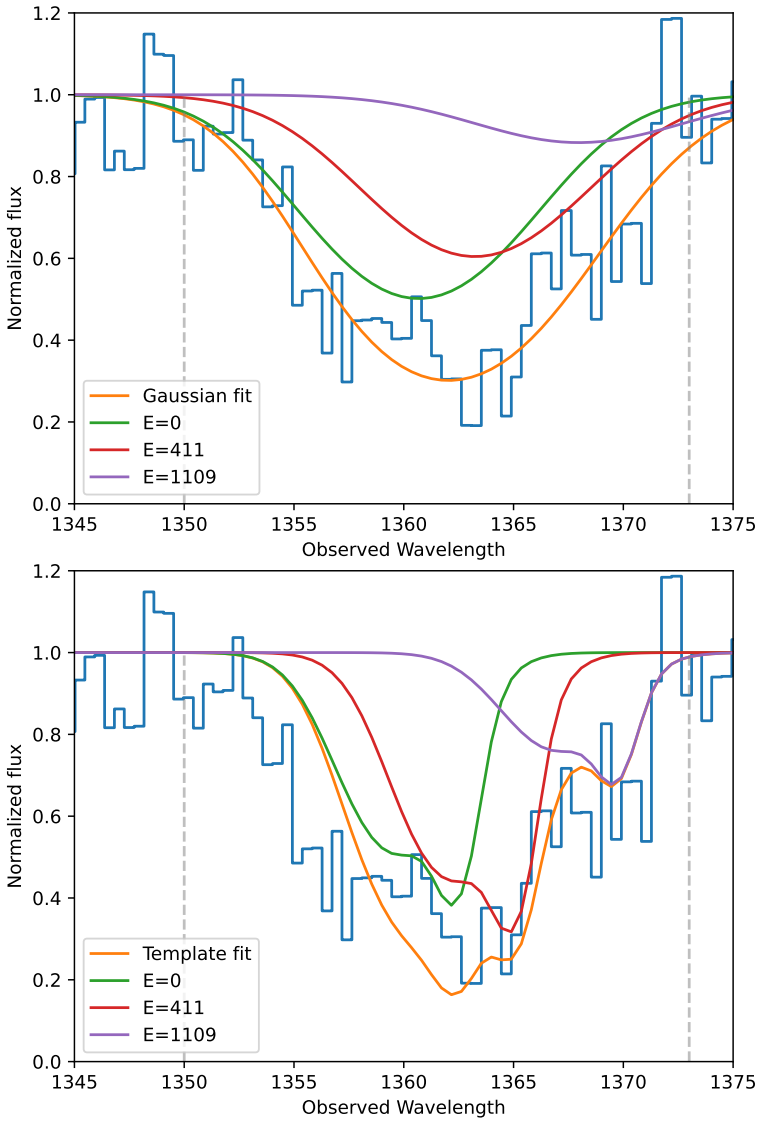

Figure 6.6 Modeling of the Ne v absorption troughs, created by fitting Gaussians (top) and by using Si xii as a template (bottom). The vertical dashed lines represent the range of data used for our fitting. The green curve is the modeled absorption of the resonance state of Ne v. The red curve shows combined absorption of the $E = 411$ cm^{-}1 level lines, and the purple curve shows the absorption of the $E = 1109$ cm^{-1} level lines. The absorption features from multiple lines of the same excited states have been combined within the figure. The orange curve represents the total combined modeled absorption of the Ne v multiplet.

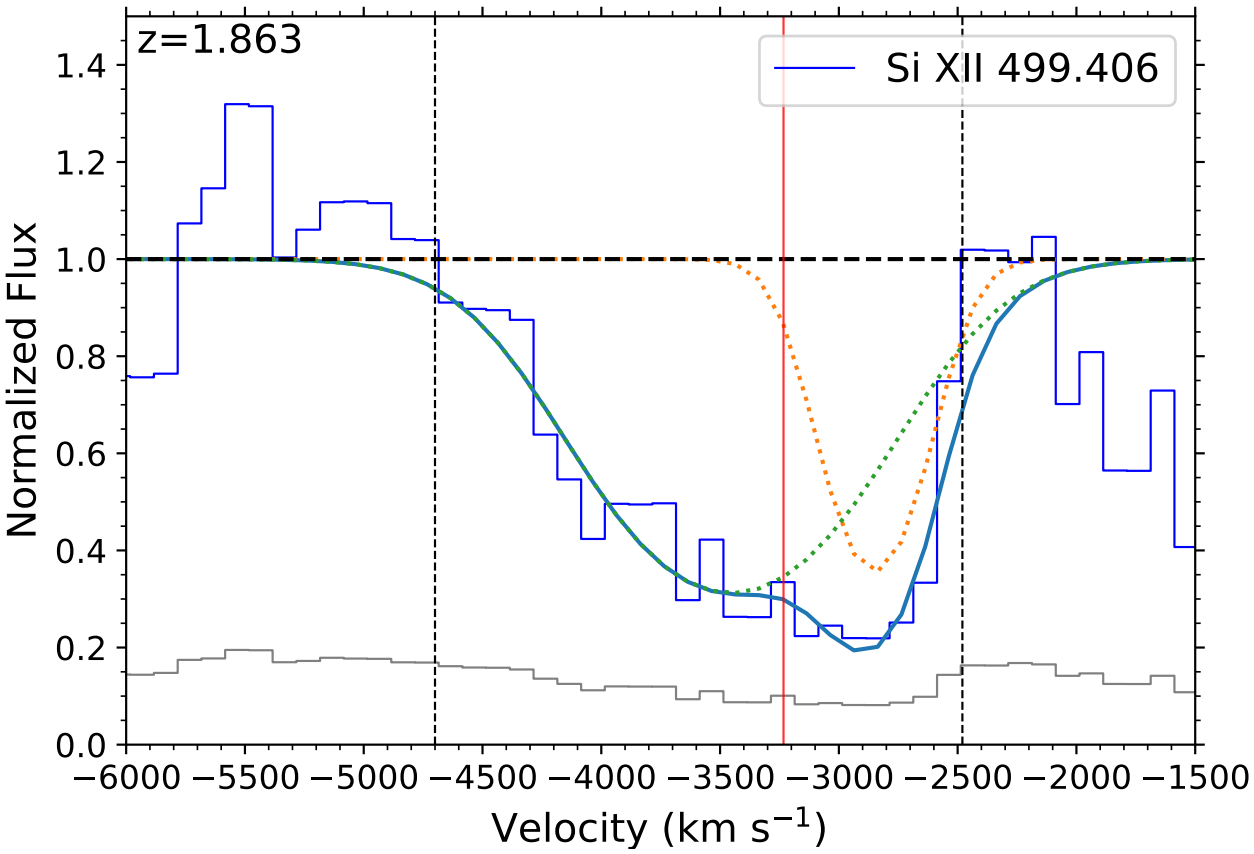

Figure 6.7 Fitting of a two-Gaussian profile to the absorption trough of Si XII. The dotted curves show the individual Gaussians in the profile, while the blue curve shows the blended profile of both Gaussians. The dotted vertical lines represent the range of data that was used for fitting the Gaussians.

6.4.3 Photoionization Solution

We used the measured ionic column densities to constrain the values of the hydrogen column density (N_H) and ionization parameter (U_H), as done in previous works [e.g 17–19, 23, 77]. For this purpose, we used a grid of simulated models produced with Cloudy [21] with a range of N_H and U_H values as input parameters, modeling the ionic abundances at different N_H and U_H. We used the ionic column densities shown in Table 6.1 to set upper and lower limits to these parameters, as shown in Figure 6.9, assuming solar metallicity. We adopted a spectral energy distribution (SED) that would match the V-band flux of Q0254-334 found on NED, the UV continuum flux measured at three separate points, as well as the X-Ray fluxes observed with Chandra at energy ranges from 0.5–7 keV (see Figure 6.8). Note that there are limitations to this SED due to potential variability between the different observations that were referenced for its construction. [15] report a V band magnitude of 16 and cite [158], who in turn discuss observations made with the 3.9 m Anglo-Australian telescope on 28 November, 1978 and on 5 December 1978. Chandra observations of Q0254-334 were made on 2 January, 2000 and 15 February 2000. We have also calculated the α_{ox} spectral index based on our SED, using the following equation [159, 160]:

$$\alpha_{ox} = 0.3838 \log \frac{L(2 \text{ kev})}{L(2500 \text{ Å})} \tag{6.5}$$

which yielded a result of $\alpha_{ox} = -1.58$. This is somewhat higher than the range of α_{ox} values of LBQS broad absorption line quasars which were reported by [161] (–2.58 to –1.65).

A single phase solution was insufficient to satisfy the constraints from the ionic column densities. To remedy this issue, we formulated a two-phase solution, in which a high- and very high-ionization phase exist co-spatially. We deduced that the two phases would be co-spatial based in the kinematic similarity between the high-ionization troughs and the

very high-ionization troughs. Specifically, Figure 6.6 shows that we get a very good fit for Ne V (a high-ionization line), using the velocity template of Si XII (a very high-ionization line, see Figure 6.7). We find that the two-phase solution satisfies more of the constraints set by the measured ionic column densities (reduced $\chi^2 = 5.1$, as opposed to 22.3 for the one-phase solution). To cover the range of possible metallicities, we have also applied models of metallicity $Z \approx 4.68 Z_{\odot}$ [3, 11], which are shown in the lower panel of Figure 6.9. The results are favorable towards the super-solar metallicity solution, of which the reduced χ^2 values are 16.0 and 0.5, for the one-phase and two-phase solutions respectively. As discussed by [14], the inability for a one-phase ionization solution to reasonably fit the measurements and limits of N_{ion} necessitates the adoption of a two-phase solution. This is further demonstrated by comparing the modeled column densities of H I, Na IX, and S XIV from supersolar one-phase and two-phase solutions to the observed ones, as shown in Table 6.2. Note that the reported measured column density of H I is an upper limit based on Ly γ. Due to the larger discrepancy between modeled and measured column densities in the solar abundance solutions (e.g. model H I column density upwards of ~ 20 times larger than measured), they have been excluded from the table. As can be seen in the table, the two-phase solution yields modeled column densities with a maximum 2σ difference between modeled and measured column densities, while the one-phase solution yields a $4 - 8\sigma$ difference. As such, the comparison of modeled column densities favors the two-phase solution. The U_H and N_H values found using χ^2 analysis are shown in Table 6.3.

We compared the N_H and U_H values found using the Q0254-334 SED with those found using the SED of the quasar HE0238-1904 [hereafter HE0238, 14], as the latter SED has been adopted for quasar outflow analysis in several past papers [e.g., 17–19, 23, 82]. We report the $\log N_H$ and $\log U_H$ values derived from the HE0238 SED in Table 6.4. Comparing these values with those found in Table 6.3 shows that while the one-phase solutions are in

Table 6.2 The measured and modeled column densities of H I, Na IX, and S XIV of the Q0254-334 outflow. The second and third columns denote the supersolar one-phase solution and the σ difference between modeled and measured values; the fourth and fifth columns show the same for the two-phase solution. The values are in units of 10^{14} cm^{-2}.

Ion	Measured	$4.68Z_{\odot}$1-p	$\Delta\sigma$	$4.68Z_{\odot}$2-p	$\Delta\sigma$
H I	$< 38^{+11}$	123	8	59	2
Na IX	48^{+12}_{-11}	96	4	55	0.6
S XIV	200^{+40}_{-40}	40	–4	190	–0.3

agreement within error, the two-phase solutions show a discrepancy in the $\log U_H$ values that range up to ~ 0.5 dex.

6.4.4 Black Hole Mass Calculation

Black hole masses of AGN are often found using the emission features of Mg II [123] or C IV [138, 139]. However, as the STIS spectrum of Q0254-334 lacked both features, we looked to the O VI emission to compute the mass of the central black hole. We referred to the method described by [162], measuring the O VI FWHM to find the mass.

Although [162] specify the use of two Gaussians to fit each line of the emission doublet, we opted to fit one Gaussian per line instead, as the lower signal to noise ratio of the STIS spectrum did not warrant the more detailed modeling method. We employed a best fit algorithm adjusting the amplitude of the blue emission line, the ratio between the blue and red lines, and the FWHM of the blue line. The ratio between the blue and red line amplitudes was constrained between 1–1.5, and the widths of the two features were fixed to be equal to each other. For the resulting fit, we found a ratio of 1, normalized amplitude $A = 0.23 \pm 0.11$, and FWHM $= 4800 \pm 900$ km s^{-1}. This, along with the measured flux of $F_\lambda = 7.7^{+1.0}_{-1.0} \times 10^{-16}$ erg s^{-1} cm^{-2} Å^{-1} at rest wavelength 1050Å, resulted in a black hole mass

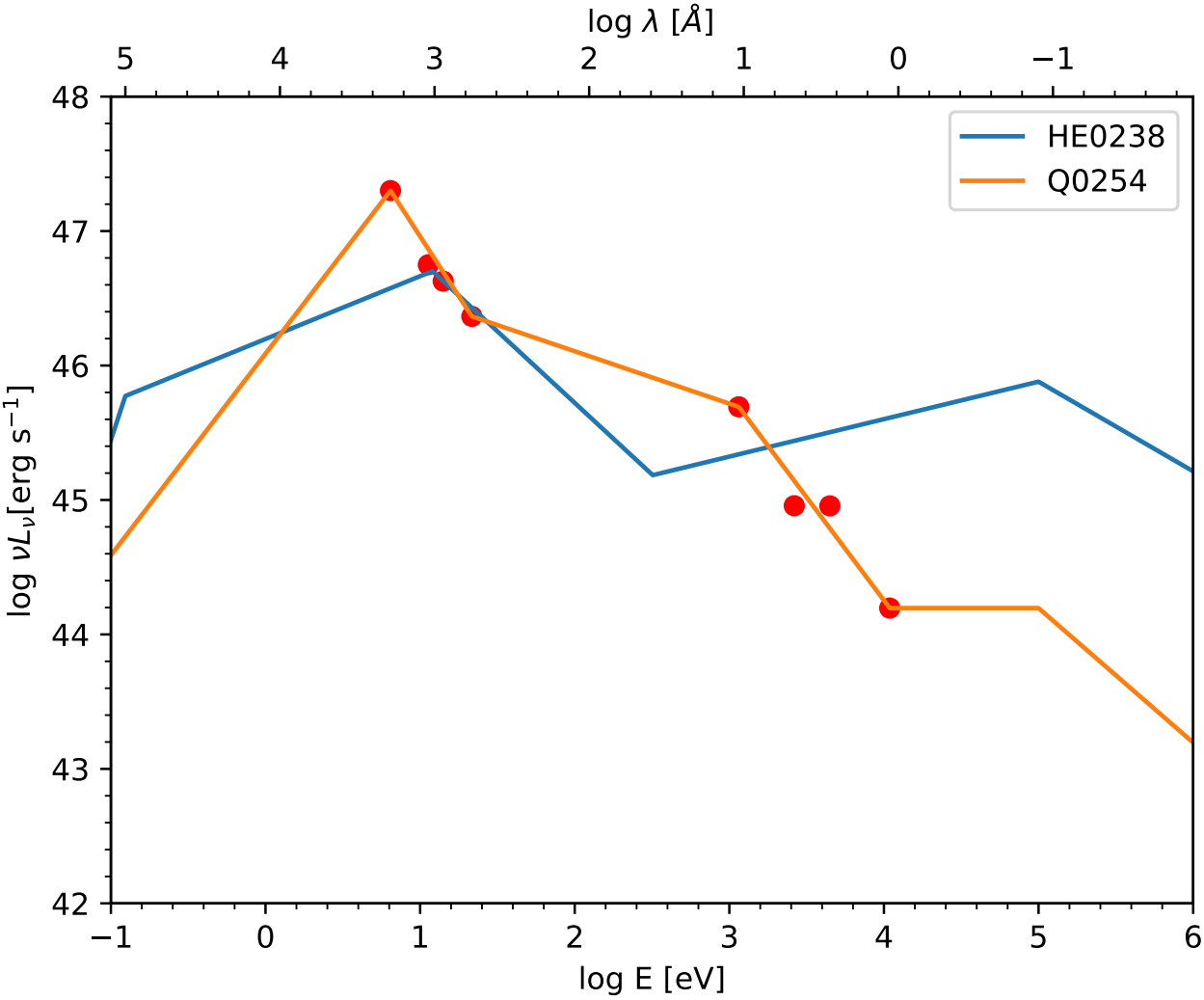

Figure 6.8 Comparison of SED shapes of HE0238 [14] and Q0254-334. The Q0254-334 SED was formed by using the V-band magnitude [the first red dot, 15], UV continuum flux measured at three different wavelengths (rest wavelengths $\lambda = 574, 880, 1097$ Å; second, third, and fourth red dots), and the X-ray fluxes reported by Chandra (5th–8th dots). The HE0238 SED was scaled to match the UV continuum flux for the sake of this comparison. We use the Q0254-334 SED for the analysis in this paper.

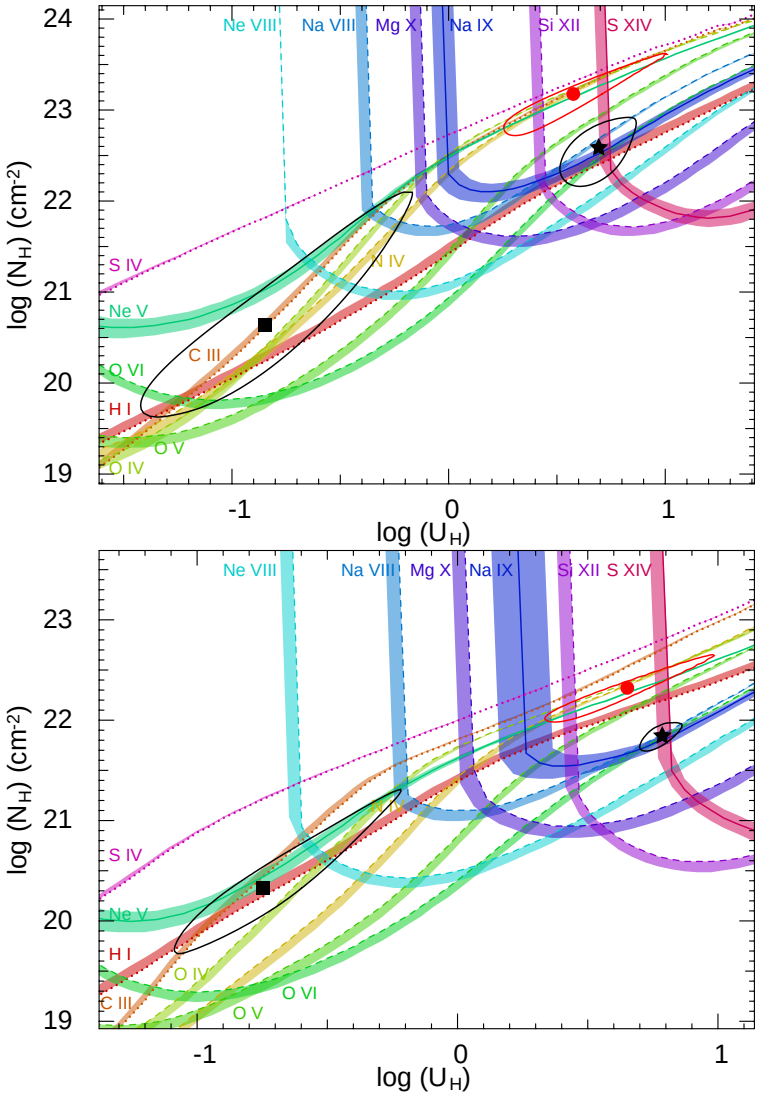

Figure 6.9 Plots of the Hydrogen column density (N_H) vs. ionization parameter (U_H), assuming solar (top) and supersolar (bottom) metallicities, with the Q0254-334 SED shown in Figure 6.8. Constraints on the parameters are based on measured column densities shown in Table 6.1. Measurements are shown as solid curves, while upper and lower limits are represented with dotted and dashed curves, respectively. The colored bands represent the uncertainties in the constraints. The red circle shows the one-phase solution of N_H and U_H, while the black square and star show the high ionization and very high-ionization phase of the two-phase solution respectively. The 1-σ uncertainties of the solutions are shown as black/red ellipses.

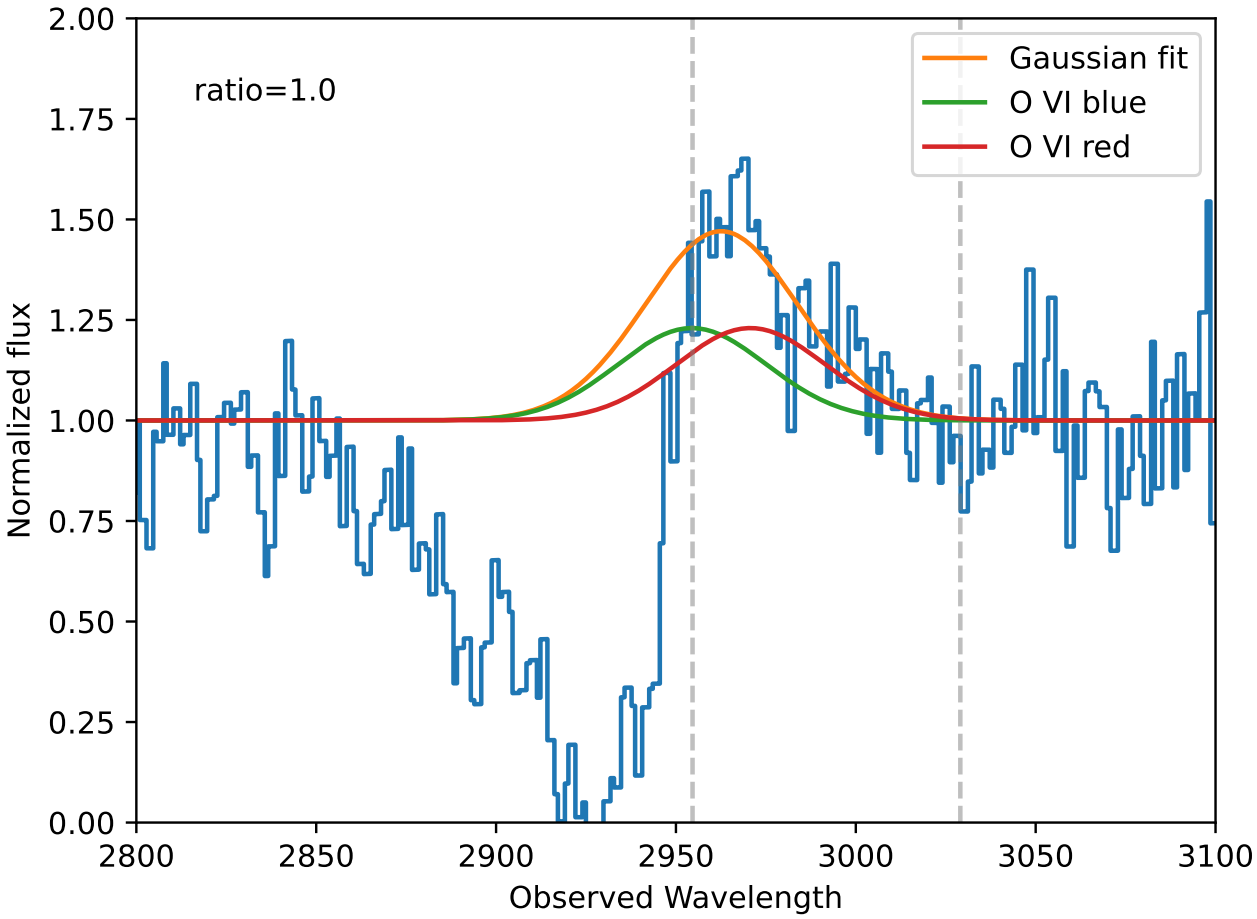

Figure 6.10 Gaussian fitting of the O VI emission feature. The dashed vertical lines denote the range of data used for the Gaussian fit. The green and red curves are the modeled blue and red emission features respectively, and the orange curve represents the combined modeled emission.

of $M_{BH} = 5.3^{+5.5}_{-2.7} \times 10^9 M_\odot$, and Eddington luminosity $L_{Edd} = 6.6^{+6.9}_{-3.4} \times 10^{47}$ erg s^{-1}. Note that we have limited our Gaussian fit to the red wing of the emission feature, as the blue wing has been contaminated by the absorption outflow (see Fig. 6.10). While this contamination has contributed significantly to the uncertainty, we were unable to find alternative emission features with which to estimate the black hole mass.

6.5 Discussion

6.5.1 Distance of the Outflow from the Central Source

With the parameters we found as described in Section 6.4, we could calculate the distance of the outflow from the central source, as well as the kinetic luminosity of the outflow. The distance can be found based on the definition of the ionization parameter U_H:

$$U_H \equiv \frac{Q_H}{4\pi R^2 n_H c} \tag{6.6}$$

where Q_H is the emission rate of ionizing photons, R is the outflow distance from the source, n_H is the hydrogen number density, and c is the speed of light. Solving the equation for R gives us

$$R = \sqrt{\frac{Q_H}{4\pi U_H n_H c}} \tag{6.7}$$

For highly ionized plasma, $n_e \approx 1.2 n_H$ [83], and the values of U_H and n_e were found in Section 6.4.

We followed the method of other works [e.g. 17, 19, 82] to find Q_H and integrated over the SED mentioned in Subsection 6.4.3, limiting our range to energies over 1 Ryd. This yielded the bolometric luminosity $L_{Bol} = 2.40^{+0.24}_{-0.24} \times 10^{47}$ erg s^{-1} and $Q_H = 9.33^{+0.94}_{-0.94} \times 10^{56}$ s^{-1}. The distance estimates of the outflow calculated with this value are shown in Tables 6.3 and 6.5.

6.5.2 Contribution of the Outflow to AGN Feedback

For an outflow to contribute to AGN feedback, its kinetic luminosity must be at least $\sim 0.5\%$ [58] or $\sim 5\%$ [53] of the quasar's Eddington luminosity. Assuming an incomplete spherical

Table 6.3 Physical Properties of the Q0254-334 Outflow. The high and very high ionization phases for the two-phase solution are assumed to be co-spatial.

Metallicity	$Z_\odot$			$4.68Z_\odot$		
Solution	One-phase	Two-phase		One-phase	Two-phase	
Phase		High	Very High		High	Very High
$log(N_{\rm H})$ [cm^{-2}]	$23.18^{+0.45}_{-0.46}$	$20.63^{+1.47}_{-1.01}$	$22.59^{+0.33}_{-0.43}$	$22.32^{+0.33}_{-0.34}$	$20.32^{+0.99}_{-0.65}$	$21.84^{+0.13}_{-0.15}$
$log(U_{\rm H})$ [dex]	$0.58^{+0.43}_{-0.32}$	$-0.85^{+0.68}_{-0.57}$	$0.69^{+0.17}_{-0.18}$	$0.65^{+0.33}_{-0.32}$	$-0.75^{+0.53}_{-0.34}$	$0.79^{+0.08}_{-0.09}$
$log(n_{\rm e})^*$ [cm^{-3}]	$4.0^{+0.1}_{-0.1}$	$4.0^{+0.1}_{-0.1}$	$2.5^{+0.7}_{-0.6}$	$4.0^{+0.2}_{-0.2}$	$4.0^{+0.1}_{-0.1}$	$2.5^{+0.5}_{-0.4}$
Distance [pc]	100^{+50}_{-40}	500^{+490}_{-280}		90^{+40}_{-30}	450^{+240}_{-210}	
$\dot{M}$ [$M_\odot$yr^{-1}]	1400^{+1000}_{-700}	1800^{+800}_{-300}		180^{+90}_{-60}	290^{+50}_{-90}	
$\dot{M}v$ [10^{36} ergs cm^{-1}]	28^{+21}_{-14}	37^{+16}_{-6}		4^{+2}_{-1}	6^{+1}_{-2}	
$log(\dot{E}_k)$ [erg s^{-1}]	$45.65^{+0.30}_{-0.24}$	$45.78^{+0.07}_{-0.16}$		$44.76^{+0.20}_{-0.18}$	$44.98^{+0.15}_{-0.07}$	
$\dot{E}_k/L_{Edd}$ [%]	$0.7^{+1.1}_{-0.4}$	$0.9^{+0.9}_{-0.5}$		$0.08^{+0.10}_{-0.05}$	$0.14^{+0.16}_{-0.07}$	
$\dot{E}_k/L_{Bol}$ [%]	$3.5^{+3.6}_{-1.5}$	$4.6^{+1.0}_{-1.4}$		$0.4^{+0.3}_{-0.2}$	$0.7^{+0.3}_{-0.1}$	

* The n_e of the very high-ionization phase is the n_e of the high phase times the ratio of the high/very-high ionization parameters.

Table 6.4 Photoionization solution for the Q0254-334 outflow assuming the HE0238 SED.

Metallicity	$Z_\odot$			$4.68Z_\odot$		
Solution	One-phase	Two-phase		One-phase	Two-phase	
Phase		High	Very High		High	Very High
$log(N_{\rm H})$ [cm^{-2}]	$23.08^{+0.38}_{-0.38}$	$20.83^{+0.85}_{-0.59}$	$22.58^{+0.16}_{-0.19}$	$22.29^{+0.36}_{-0.34}$	$20.61^{+0.98}_{-0.94}$	$21.84^{+0.48}_{-0.19}$
$log(U_{\rm H})$ [dex]	$0.88^{+0.30}_{-0.24}$	$-0.39^{+0.47}_{-0.40}$	$1.00^{+0.06}_{-0.08}$	$0.87^{+0.29}_{-0.25}$	$-0.24^{+0.54}_{-0.59}$	$1.01^{+0.07}_{-0.09}$

shell, the mass flow rate can be calculated as follows:

$$\dot{M} \simeq 4\pi\Omega R N_H \mu m_p v \tag{6.8}$$

followed by the kinetic luminosity:

$$\dot{E}_k \simeq \frac{1}{2}\dot{M}v^2 \tag{6.9}$$

where Ω is the global covering factor, $\mu = 1.4$ is the mean atomic mass per proton, v is outflow velocity, and m_p is the mass of a proton [118]. We assumed $\Omega = 0.2$, as C IV BALs are found in $\sim 20\%$ of quasars [37]. We use the Ω associated with C IV BALs, since our high-ionization phase has troughs from ions of very similar ionization potential. For example, in our spectrum, we detect O IV λ787. O IV has an ionization potential of 77 eV, which is quite similar to the C IV ionization potential of 64 eV. Assuming supersolar metallicity, this calculation yielded a kinetic luminosity of $\log \dot{E}_k = 44.76^{+0.20}_{-0.18}$[erg s^{-1}] for the one-phase solution, and $\log \dot{E}_k = 44.98^{+0.15}_{-0.07}$[erg s^{-1}] for the two-phase solution, leaving a ~ 0.2 dex difference between the solutions.

The ratio between the kinetic luminosity and Eddington luminosity yields $\dot{E}_k/L_{Edd} = 0.08^{+0.10}_{-0.05}\%$ for the one-phase solution, and $\dot{E}_k/L_{Edd} = 0.14^{+0.16}_{-0.07}\%$ for the two-phase solution, which is below the 0.5% threshold. For the sake of completeness, we have also found the ratio between $\dot{E}_k$ and the bolometric luminosity L_{Bol}, resulting in $\dot{E}_k/L_{Bol} = 0.4^{+0.3}_{-0.2}\%$ and $0.7^{+0.3}_{-0.1}\%$ (see Table 6.3). Based on the ratio between $\dot{E}_k$ and L_{Edd}, the outflow would be unable to contribute to AGN feedback. It is important to note that the different assumed metallicity values have significant effects on the physical parameters of the outflow, such as a near order of magnitude difference in kinetic luminosity, leading to values that may be sufficient for AGN feedback contribution (see Table 6.3).

6.5.3 The Two-Phase Outflow

As mentioned earlier in Section 6.4.3, the two-phase photoionization solution provides a better fit to the constraints from the measured ionic column densities. While the values of $\dot{E}_k$ for the one-phase and two-phase solutions agree with each other within error (see Table 6.3), there are significant differences to be found in the other parameters, such as distance, N_H, and U_H.

Note that the difference in N_H between the high- and very high-ionization phases is ~ 1.5 orders of magnitude, as well as the difference in U_H. Assuming the two phases are co-spatial, the volume filling factor of the high-ionization phase is as follows [14, 82]:

$$f_{\rm V} = \frac{U_{H,HP}}{U_{H,VHP}} \times \frac{N_{H,HP}}{N_{H,VHP}} \tag{6.10}$$

resulting in $\log f_{\rm V} = -3.1^{+1.1}_{-0.9}$, which follows our expectations from the high-ionization phase's larger n_e and smaller N_H values compared to those of the very high-ionization phase.

6.5.4 Connection to X-Ray Warm Absorbers

The two-phase solution for the outflow of Q0254-334 is comparable to the parameters measured in X-ray warm absorbers. For instance, in their analysis of the Seyfert galaxy NGC 3783, [163] found the parameters of the absorbing gas composed of three different components, with the oxygen ionization parameter ranging from $\log U_{ox} = -2.4$ to -0.6. To effectively compare the U_H of Q0254-334 to the U_{ox} values of NGC 3783, we calculated the oxygen ionizing emission rate Q_{ox} as defined below:

$$Q_{ox} = \int_{\nu(0.54\ \mathrm{keV})}^{\nu(10\ \mathrm{keV})} \frac{L_\nu}{h\nu} d\nu \tag{6.11}$$

Table 6.5 Physical Properties of the Q0254-334 Outflow, based on the Si XII template-based fitting of the Ne V absorption. The high and very high ionization phases for the two-phase solution are assumed to be co-spatial.

Metallicity	$Z_\odot$			$4.68Z_\odot$		
Solution	One-phase	Two-phase		One-phase	Two-phase	
Phase		High	Very High		High	Very High
$log(n_e)$ [cm^{-3}]	$4.3^{+0.1}_{-0.1}$	$4.3^{+0.1}_{-0.1}$	$2.8^{+0.7}_{-0.6}$	$4.3^{+0.1}_{-0.1}$	$4.3^{+0.1}_{-0.1}$	$2.8^{+0.5}_{-0.3}$
Distance [pc]	70^{+30}_{-20}	370^{+350}_{-200}		70^{+30}_{-20}	330^{+170}_{-150}	
$\dot{M}$ [$M_\odot$yr^{-1}]	1000^{+700}_{-500}	1300^{+500}_{-200}		130^{+60}_{-50}	210^{+30}_{-60}	
$\dot{M}v$ [10^{36} ergs cm^{-1}]	20^{+15}_{-10}	27^{+10}_{-3}		$2.6^{+1.3}_{-0.9}$	$4.4^{+0.6}_{-1.2}$	
$log(\dot{E}_k)$ [erg s^{-1}]	$45.52^{+0.30}_{-0.24}$	$45.64^{+0.06}_{-0.15}$		$44.63^{+0.19}_{-0.17}$	$44.85^{+0.14}_{-0.06}$	
$\dot{E}_k/L_{Edd}$ [%]	$0.5^{+0.8}_{-0.3}$	$0.6^{+0.6}_{-0.3}$		$0.06^{+0.08}_{-0.03}$	$0.10^{+0.11}_{-0.05}$	
$\dot{E}_k/L_{Bol}$ [%]	$2.6^{+2.6}_{-1.1}$	$3.4^{+0.6}_{-1.0}$		$0.33^{+0.19}_{-0.11}$	$0.55^{+0.23}_{-0.08}$	

such that the ratio $\frac{Q_{ox}}{Q_H} = \frac{U_{ox}}{U_H}$. The resulting value of the emission rate was $Q_{ox} = 3.9^{+0.4}_{-0.4} \times 10^{54}$ s^{-1}, which is 2.4 ± 0.1 orders of magnitude smaller than Q_H. Subtracting 2.4 ± 0.1 from the $\log U_H$ values of the high- and very high-ionization phases leads to $\log U_{ox} = -3.2^{+0.5}_{-0.5}$ and $-1.6^{+0.3}_{-0.3}$ respectively. The very high-ionization phase has a U_{ox} within the range of U_{ox} values of the NGC 3783 absorbing gas. We note that NGC 3783 is a much lower luminosity AGN than Q0254-334, and that its SED may be different. However, lacking high quality X-ray spectra of $z \sim 1$ quasars, it is still illuminating to compare the NGC 3783 X-ray wind with the EUV wind seen in Q0254-334.

6.5.5 Comparison to Other Extreme UV Objects

As the spectrum of Q0254-334 covers observed wavelengths as short as 400Å, we found it appropriate to compare it with other quasars observed in the extreme UV range [hereafter EUV500, 9]. We compiled a list of the physical parameters of 28 EUV500 quasar outflow systems analyzed in previous works [3, 9, 16, 82, 86, 91, 122], and added the parameters of Q0254-334 for comparison, with a total of 29 EUV500 outflow systems. Out of the 29 outflow systems, 24, including the outflow discussed in this paper, have measurements of kinetic luminosity and distance from the source. We compared the parameters of the Q0254-334 outflow such as $\dot{E}_K$, N_H, R, and U_H, with the other 23 outflow systems.

As seen in Figure 6.12, no strong correlation has been found between $\log \dot{E}_k$ and $\log L_{Edd}$, or between $\log \dot{E}_k$ and $\log L_{Bol}$. 4 of the 24 outflows ($\sim$ 16%) are above the threshold of $\dot{E}_k/L_{Edd} \sim 5\%$, while 7 ($\sim$ 29%) are between the 0.5% and 5% thresholds. With regards to L_{Bol}, 5 of the outflow systems ($\sim$ 20%) are above the 5% threshold, while 7 ($\sim$ 29%) are between the 0.5% and 5% thresholds. Note that while the values of $\log \dot{E}_k$ range between 41–47, $\log L_{Edd}$ and $\log L_{Bol}$ range between 47.0–47.9 and 46.6–47.6 respectively, which is much narrower than the range of $\log \dot{E}_k$. It is also indicative of the ability of line-of-sight analysis to identify outflow systems at large ranges of kinetic luminosity, as well as velocity. Figure 6.13 shows the $\log N_H$ and $\log U_H$ values of the high- and very high-ionization phases of each of the outflow systems. With the exception of the very high-ionization phase of the outflow system of UM425 traveling at -9420 km s^{-1}, the high-ionization phases tend to have values of $\log U_H < 0$, while the very high-ionization phases have $\log U_H > 0$. Note that the very high-ionization phase of the Q0254-334 outflow has a higher $\log U_H$ value relative to the average of the other outflows. We largely attribute this to the detection of S XIV. As can be seen in Figure 6.9, the very high-ionization phase solution is at the intersection between the Na IX and S XIV constraints. The $\log U_H$ value is $\sim$ 0.3 dex higher than what it would have

been if S XIV were not detected, and the parameters were constrained by other ions such as Si XII. It is also notable that as shown in Figure 6.13, the $\log U_H$ of the very high-ionization phase of the Q0254-334 outflow is higher than the average $\log U_H$ of the other outflows. We suspect that future observed outflows with S XIV would yield comparably high U_H values.

Note that there is an apparent edge in the range of $\log N_H$ and $\log U_H$ values of the outflows. In Figure 6.13, we have indicated the approximate locations of the hydrogen ionization front ($N_H \approx 10^{23} U_H$), as well as the He II ionization front ($N_H \approx 10^{22.2} U_H$). The N_H/U_H ratio for the He II ionization front was calculated based on the average $\log N_H$ value at which the He II to He III ratio is 1:1 in a series of CLOUDY models created with a range of $-2.0 < \log U_H < 1.0$. We used the aforementioned SED of HE0238 for the models, as this SED was used for the analysis of the majority of the EUV500 outflows in question. Interestingly, the $\log N_H$ vs. $\log U_H$ values of all of the EUV500 outflows fall under the He II ionization front, which would suggest that they are high ionized BALs (HiBALs) as opposed to low ionized BALs (LoBALs). This is supported by the lack of BALs from low-ionization species. For instance, there is a noticeable lack of absorption where the trough of C II λ687 would be, despite a large oscillator strength of f=0.336 (see Figure 6.11).

We also examined the ranges of R and v of the outflow systems (see Figure 6.14). To examine the correlation between distance and velocity, we conducted a weighted least squares linear fit between $\log R$ and $\log |v|$, taking into account the asymmetry of the reported errors in R. We adopted the weight determination method described by [136]. The weight of each data point $w_i = 1/V_i$ was determined by the value of V_i:

$$V_i = \sigma_i^2 + (1 - \frac{2}{\pi})\alpha_i^2 \tag{6.12}$$

in which $\sigma_i = \frac{\sigma_i^+ + \sigma_i^-}{2}$ is the mean of the upper and lower errors of $\log R$, while $\alpha_i = \frac{\sigma_i^+ - \sigma_i^-}{2}$.

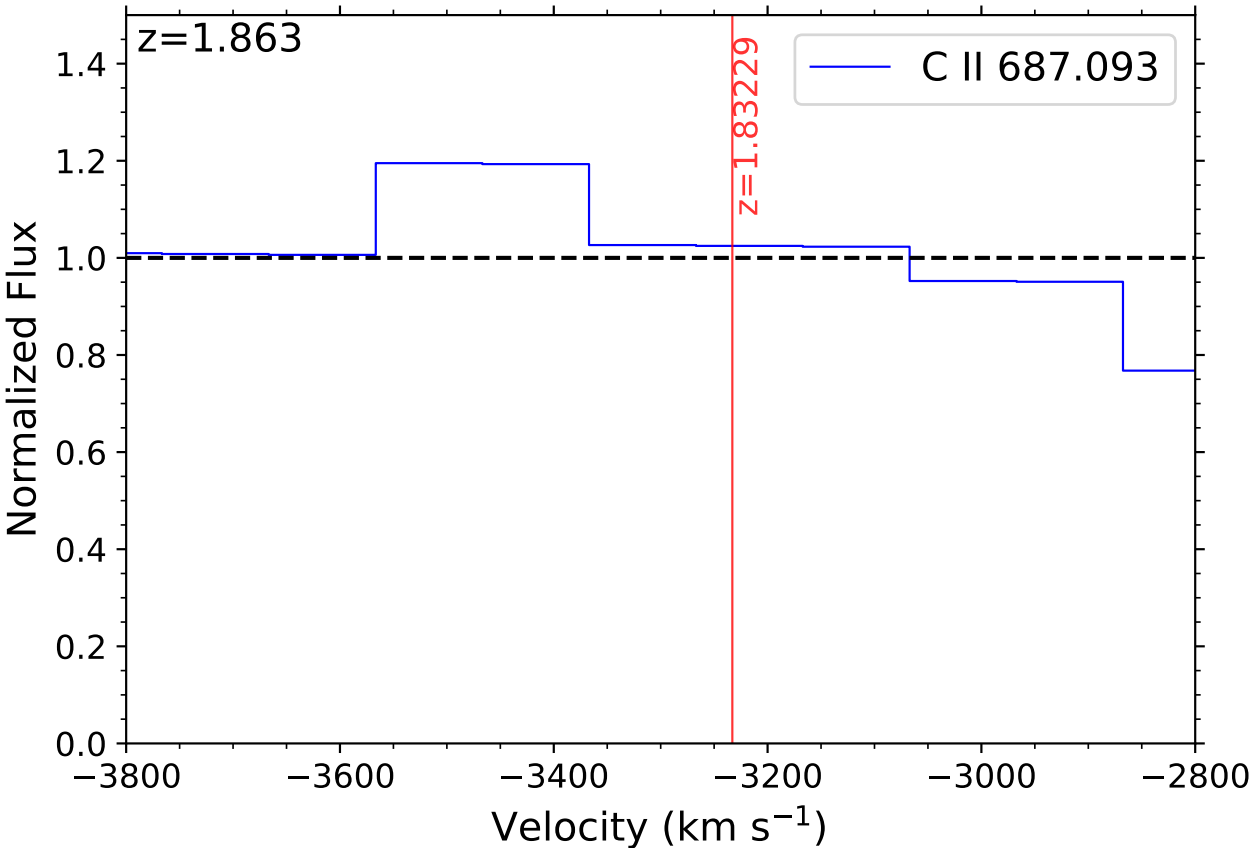

Figure 6.11 Region in which C II λ687 absorption is expected to be found.

The weighted linear fit yielded a slope of -1.08 and an intercept of 6.44, suggesting a negative correlation. To determine the strength of the correlation, we calculated a modified value of the coefficient of determination r^2 that would take into account the weight of each data point. The residual sum of squares SS_{res} was modified so that:

$$SS_{res} = \sum_i w_i(\log R_i - f_i)^2 \tag{6.13}$$

where f_i is the value of $\log R$ according to the linear fit. The total sum of squares SS_{tot} was adjusted so that:

$$SS_{tot} = \sum_i w_i(\log R_i - \langle \log R \rangle)^2 \tag{6.14}$$

where $\langle \log R \rangle$ is the weighted mean of $\log R$. The resulting value of $r^2 = 1 - \frac{SS_{res}}{SS_{tot}}$ is 0.28, suggesting a weak negative correlation between $\log R$ and $\log |v|$. This correlation is further supported by a Spearman correlation of -0.43 and associated p value of 0.05. We find it worth mentioning that [85] have conducted a similar analysis of iron low ionized BALs (FeLoBALs), in which they determined that the correlation (or anti-correlation) between distance and velocity was dependent on the E1 parameter, which is formulated based on the relationship between the equivalent width of [O III] emission and the ratio between Fe II and H β fluxes [149].

6.6 Summary and Conclusion

We have identified a BAL outflow in the HST/STIS spectrum of the quasar QSO B0254-3327B, of which we have found the ionic column densities (see Table 6.1). Based on the column densities, we conducted photoionization analysis to find the values of hydrogen column density N_H and ionization parameter U_H. The results of our analysis are as follows:

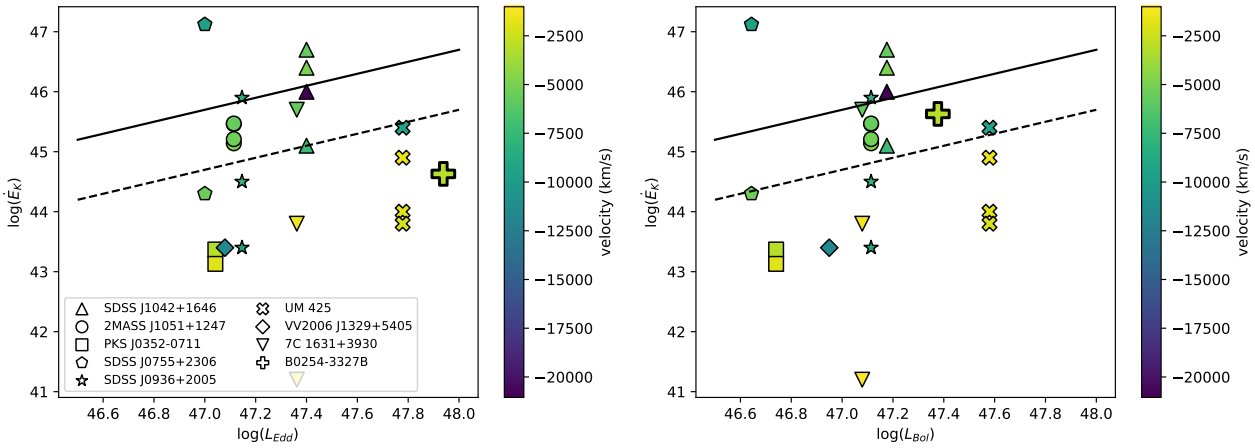

Figure 6.12 Distribution of $\log \dot{E}_k$ vs. $\log L_{Edd}$ (left) and $\log L_{Bol}$ (right) of EUV500 outflows. The dashed and solid lines on the left (right) indicate the $\dot{E}_k/L_{Edd}$ ($\dot{E}_k/L_{Bol}$) thresholds of 0.5% and 5% respectively. The plus-sign symbol denotes the outflow of Q0254-334 as reported in this paper, while the other symbols denote the parameters of other EUV outflows reported by [9] and [16]. The color map corresponds to the velocities of the outflow systems.

1. *The two-phase solution.* The constraints from the measured ionic column densities required a solution with two ionization phases: the high-ionization phase and the very high-ionization phase. The two-phase solution showed a significant improvement in the χ^2 value compared to that of the one-phase solution (reduced $\chi^2 = 5.1$ vs. 22.3).

2. *The energetics of the outflow.* We were able to determine the composition of the Ne v trough via Gaussian fitting of the blended features (see Figure 6.6), thanks to which we were able to narrow down the electron number density n_e. Through the use of Equations 6.7, 6.8, and 6.9, we were able to determine the distance, mass flow rate, and kinetic luminosity of the outflow (see Table 6.3). There were notable differences in the energetics parameters based on different values of assumed metallicity ($Z = Z_\odot$ vs $Z = 4.68 Z_\odot$, see Tables 6.3 and 6.5).

3. *Potential contribution to AGN feedback.* As the ratio between the kinetic luminosity and the quasar's Eddington luminosity $\dot{E}_k/L_{Edd} = 0.9^{+0.9}_{-0.5}\%$ assuming solar abundance, and

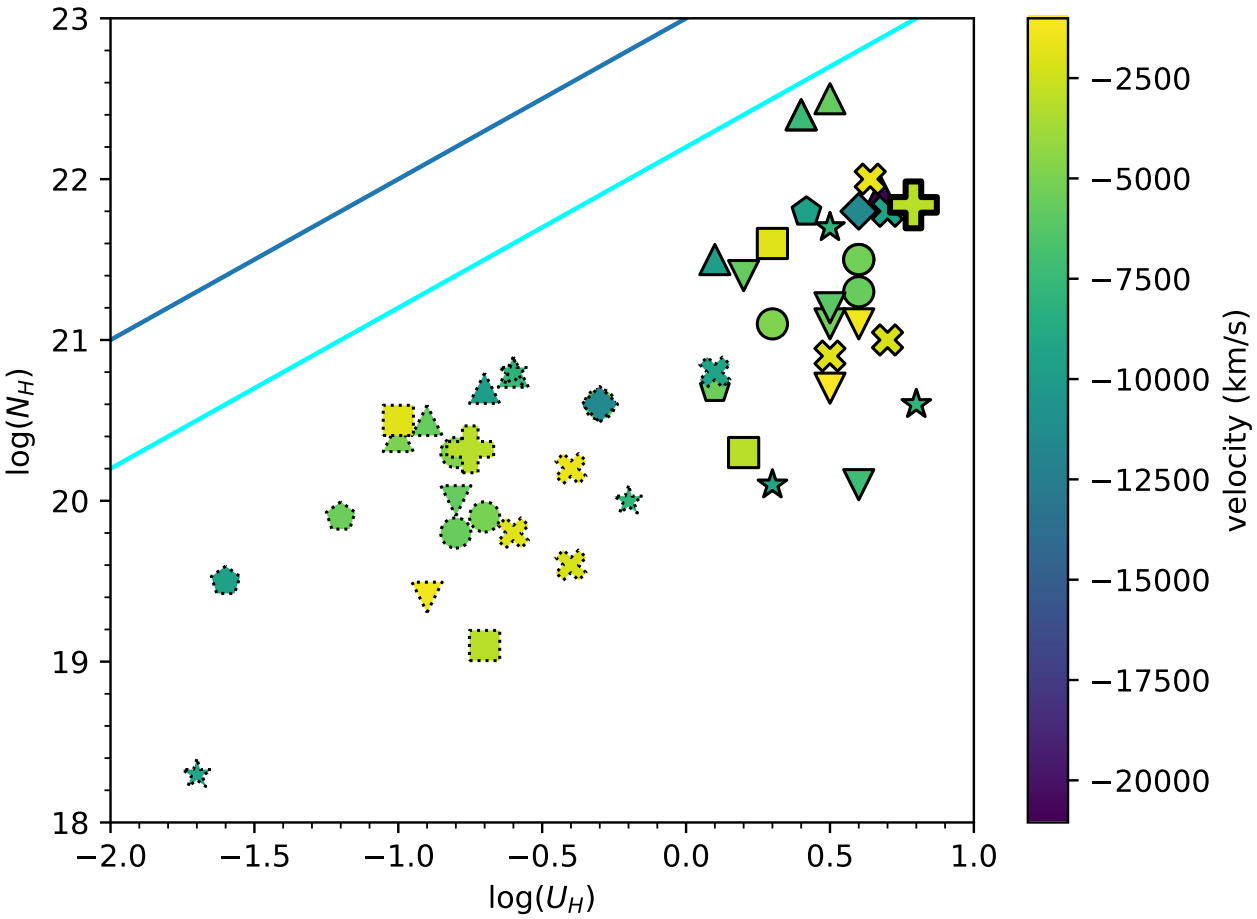

Figure 6.13 Distribution of $\log N_H$ vs. $\log U_H$ of EUV500 outflows. Symbols are coded as they are in Figure 6.12. Symbols with dotted outlines denote high-ionization phases, while symbols with solid outlines denote very high-ionization phases. The color map corresponds to the velocities of the outflow systems. The dark blue and cyan curves show the H I and He II ionization fronts respectively.

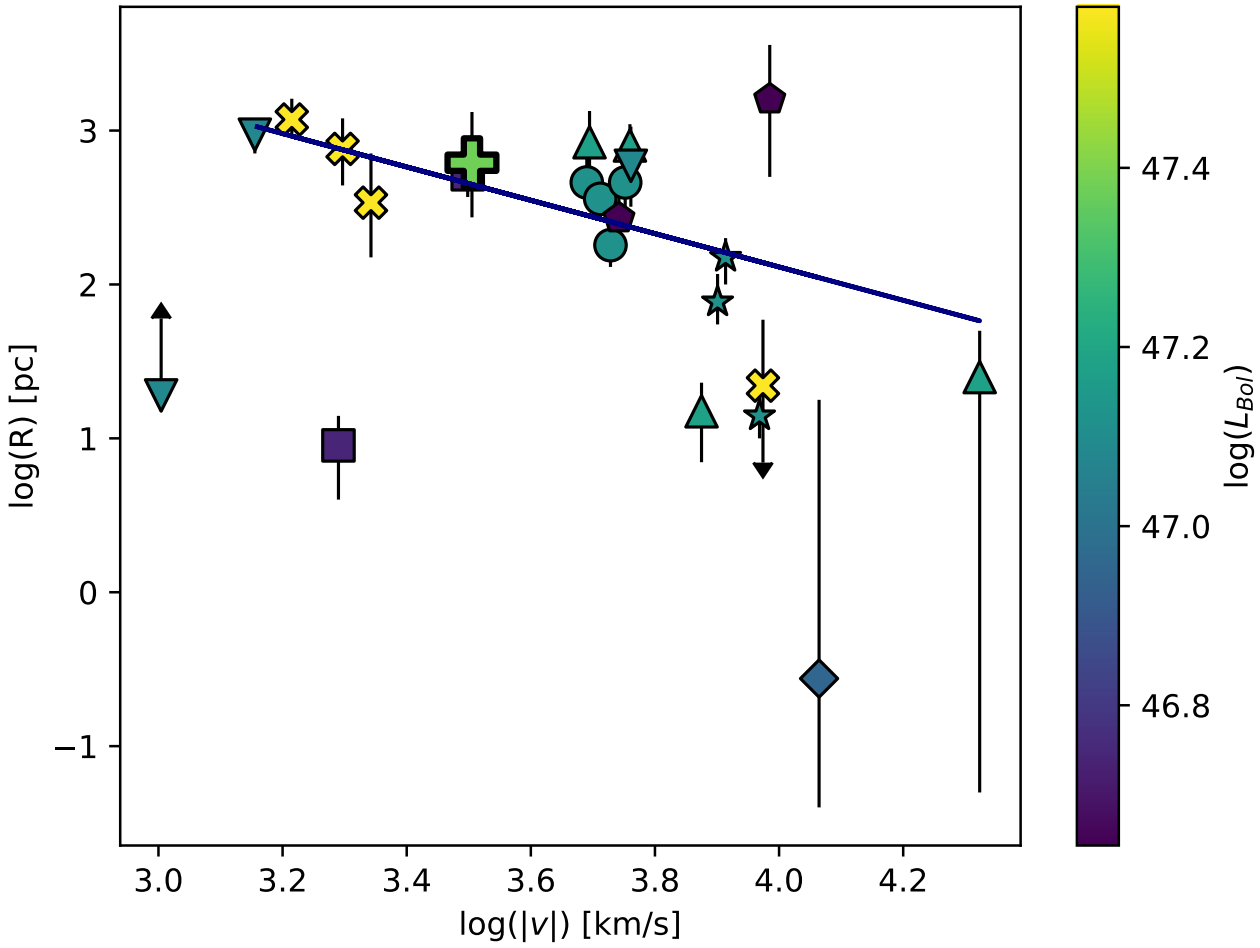

Figure 6.14 Distribution of $\log R$ vs. $\log|v|$ of EUV500 outflows. Symbols are coded as they are in Figure 6.12, with errors in $\log R$ indicated with error bars. The dark blue line shows the weighted least squares linear fit of $\log R = -1.08 \times \log|v| + 6.44$, with adjusted $r^2 = 0.28$. The color map corresponds to the $\log L_{Bol}$ values of the outflows.

$0.14^{+0.16}_{-0.07}$ assuming super-solar abundance, its contribution to AGN feedback is model dependent, as the theoretical thresholds for the ratio are $\sim 0.5\%$ [58] and $\sim 5\%$ [53].

4. *Comparison to X-ray warm absorbers.* We have compared the ionization parameter values of the high-ionization and very high-ionization phase to that of the X-ray warm absorber of NGC 3783 analyzed by [163]. Converting U_H to the oxygen ionization parameter U_{ox} as defined by [163] showed that the U_{ox} of the very high-ionization phase agreed with that of the NGC 3783 absorber within the error.

5. *Comparison with other EUV500 outflows.*We have also examined the physical parameters of previously studied EUV500 outflows [3, 9, 16, 82, 86, 91, 122], and determined that out of the sample of 24 outflow systems with measured kinetic luminosity, up to $\sim 50\%$ may contribute to AGN feedback, depending on the theoretical model. The trend between $\log R$ and $\log |v|$ was also analyzed via a weighted least squares linear fit, showing a weak negative correlation, indicated by a Spearman rank of –0.43, and p value of 0.05. We have also found that the very high-ionization phase of the Q0254-334 outflow had one of the highest U_H values of all UV absorption outflows to date.

The process of finding $\log n_e$ was limited to the examination of a blended trough of Ne v. Further observations and analyses of the quasar may reveal more excited state troughs, which could help improve the uncertainty in $\log n_e$. Studying additional EUV500 outflows will be essential in a more thorough statistical analysis of their parameters as well.

Acknowledgements

We thank Dr. J. Michael Shull and Dr. Kirk Korista for their input and advice, and Dr. Paola Rodriguez Hidalgo for her insight. We also thank the anonymous reviewer for their

valuable input. We acknowledge support from NSF grant AST 2106249, as well as NASA STScI grants AR-15786, AR-16600, and AR-16601. This research has made use of the NASA/IPAC Extragalactic Database (NED), which is funded by the National Aeronautics and Space Administration and operated by the California Institute of Technology.

Data Availability

The STIS data of Q0254-334 described in this paper may be obtained from the MAST archive at https://dx.doi.org/10.17909/63xd-4s51. The FOS data shown for comparison can be obtained at https://dx.doi.org/10.17909/z7ta-9048.

Chapter 7

Conclusions

In this dissertation, we present the analyses of the outflows of five different quasars. In order to contribute to AGN feedback, a quasar's outflow must have a kinetic luminosity ($\dot{E}_k$) of at least $\sim 0.5\%$ the quasar's Eddington luminosity [58]. We found the physical characteristics of the outflows, including electron number density (n_e), Hydrogen column density (N_H), ionization parameter (U_H), and outflow distance from the source (R).

In Chapter 2, we examined the VLT/UVES spectrum of the quasar SDSS J0242+0049, identifying 4 different outflow systems. Two of the outflow systems were found to have sufficient kinetic luminosity to contribute to AGN feedback, one of which being a mini-BAL system with a distance of $R \sim 67$ kpc from the quasar. We also examined the time variability in the velocity and equivalent width of a high-velocity C IV BAL, which was previously studied by [98]. Between September 2001 and January 2017, its velocity increased monotonically, and its equivalent width steadily decreased, suggesting that its time variability was caused by a change in ionization.

In Chapter 3, we conducted a similar analysis of the outflow of SDSS J2357-0048. In its VLT/UVES spectrum, we identified a BAL outflow with four subcomponents, as well as a high-velocity C IV mini-BAL. Based on the analysis of one of the subcomponents of the BAL outflow, we determined that its ability to contribute to AGN feedback to be dependent on the selected chemical abundance model. In examining the time variability of the C IV mini-BAL, we found a smaller absorption feature within the trough that disappeared between

2001 and 2005.

In Chapter 4, we discuss the analysis of the outflow of SDSS J1439-0106. We identified two outflow systems: a mini-BAL system and a NAL system. We were able to find the mini-BAL's n_e and R values thanks to the presence of Fe II absorption at six different energy levels. The resulting ratio of $\dot{E}_k/L_{Edd}$ was 0.099 or 0.023 depending on the model used, which is insufficient for AGN feedback contribution.

In Chapter 5, we show the analysis of the FeLoBAL outflow found in the VLT/UVES spectrum of SDSS J1321-0041. The presence of Si II and C II BALs makes it unusual among FeLoBAL outflows. Due to a lack of diagnostics that could be used to find the black hole mass, we were limited to using bolometric luminosity L_{Bol} as a substitute for L_{Edd}. Comparing the outflow's kinetic luminosity with the bolometric luminosity resulted in a ratio of $\sim$ 4.8%, which, assuming $L_{Bol} \approx L_{Edd}$, would make it enough to contribute to AGN feedback.

In Chapter 6, we analyzed the EUV500 BAL outflow of QSO B0254-3327B (hereafter Q0254-334), and compared its physical characteristics with those of other outflows observed in the EUV500 wavelength range. We constructed a new SED based on HST and Chandra observations of the object, resulting in a range of $\dot{E}_k/L_{Edd}$ from 0.08% to 0.9%. The best fitting solution, the two-phase supersolar metallicity solution, resulted in a distance $R = 450$ pc, and $\dot{E}_k/L_{Edd} = 0.14$, making it insufficient to contribute to AGN feedback. In its comparison with other EUV500 outflows, the outflow of Q0254-334 was among the most ionized. We have also found a weak negative correlation between outflow velocity and distance from the central source.

Overall, while we have found that some of the studied outflows are powerful enough to contribute to AGN feedback, the results of our analysis are dependent on factors such as the

chemical abundance of the outflow. Further analysis of a larger sample of quasar outflows will be required to examine the general trend of outflows, and new methods of estimating outflow chemical abundance may be needed to improve the accuracy of future studies.

Bibliography

[1] F. Fiore, C. Feruglio, F. Shankar, M. Bischetti, A. Bongiorno, M. Brusa, S. Carniani, C. Cicone, F. Duras, A. Lamastra, V. Mainieri, A. Marconi, N. Menci, R. Maiolino, E. Piconcelli, G. Vietri, and L. Zappacosta, "AGN wind scaling relations and the co-evolution of black holes and galaxies," *Astronomy and Astrophysics*, vol. 601, p. A143, May 2017.

[2] T. R. Miller, N. Arav, X. Xu, and G. A. Kriss, "The contribution of quasar absorption outflows to AGN feedback," *Monthly Notices of the Royal Astronomical Society*, vol. 499, no. 1, pp. 1522–1529, Nov. 2020.

[3] T. R. Miller, N. Arav, X. Xu, G. A. Kriss, and R. J. Plesha, "HST/COS Observations of Quasar Outflows in the 500-1050 Å Rest Frame. V. Richness of Physical Diagnostics and Ionization Potential-dependent Velocity Shift in PKS J0352-0711," *The Astrophysical Journal Supplement Series*, vol. 247, no. 2, p. 41, Apr. 2020.

[4] D. Byun, "Quasar Outflows and Active Galactic Nucleus Feedback," 2021, Presentation at the Virginia Space Grant Consortium Student Research Conference.

[5] G. Walker, "High Mass Flow Rate in a BAL Outflow of Quasar SDSS J1130+0411," 2023, Presentation at AGN Winds at the Chesapeake.

[6] B. C. J. Borguet, N. Arav, D. Edmonds, C. Chamberlain, and C. Benn, "Major Contributor to AGN Feedback: VLT X-shooter Observations of S IV BALQSO Outflows," *The Astrophysical Journal*, vol. 762, no. 1, p. 49, Jan. 2013.

[7] X. Xu, N. Arav, T. Miller, and C. Benn, "A Mini-BAL Outflow at 900 pc from the

Central Source: VLT/X-shooter Observations," *The Astrophysical Journal*, vol. 858, no. 1, p. 39, May 2018.

[8] J. P. Dunn, B. Wasik, C. L. Holtzclaw, D. Yenerall, M. Bautista, N. Arav, D. Hayes, M. Moe, L. C. Ho, and S. Harper Dutton, "Determining the Locations of Dust Sources in FeLoBAL Quasars," *The Astrophysical Journal*, vol. 808, no. 1, p. 94, Jul. 2015.

[9] N. Arav, X. Xu, T. Miller, G. A. Kriss, and R. Plesha, "HST/COS Observations of Quasar Outflows in the 500-1050 Å Rest Frame. I. The Most Energetic Outflows in the Universe and Other Discoveries," *The Astrophysical Journal Supplement Series*, vol. 247, no. 2, p. 37, Apr. 2020.

[10] M. T. Murphy, G. G. Kacprzak, G. A. Savorgnan, and R. F. Carswell, "The UVES Spectral Quasar Absorption Database (SQUAD) data release 1: The first 10 million seconds," *Monthly Notices of the Royal Astronomical Society*, vol. 482, no. 3, pp. 3458–3479, jan 2019. [Online]. Available: http://quasars.org/milliquas.htm.

[11] S. K. Ballero, F. Matteucci, L. Ciotti, F. Calura, and P. Padovani, "Evolution of chemical abundances in Seyfert galaxies," *Astronomy & Astrophysics*, vol. 478, no. 2, pp. 335–351, Feb. 2008.

[12] K. P. Dere, E. Landi, H. E. Mason, B. C. Monsignori Fossi, and P. R. Young, "CHIANTI - an atomic database for emission lines," *"Astronomy & Astrophysics Supplement Series"*, vol. 125, pp. 149–173, Oct. 1997.

[13] K. P. Dere, G. D. Zanna, P. R. Young, E. Landi, and R. S. Sutherland, "CHIANTI—an atomic database for emission lines. XV. version 9, improvements for the x-ray satellite lines," *The Astrophysical Journal Supplement Series*, vol. 241, no. 2, p. 22, mar 2019. [Online]. Available: https://doi.org/10.3847/1538-4365/ab05cf

[14] N. Arav, B. Borguet, C. Chamberlain, D. Edmonds, and C. Danforth, "Quasar outflows and AGN feedback in the extreme UV: HST/COS observations of HE 0238-1904," *Monthly Notices of the Royal Astronomical Society*, vol. 436, no. 4, pp. 3286–3305, Dec. 2013.

[15] S. M. Rao, D. A. Turnshek, and D. B. Nestor, "Damped Lyα Systems at z<1.65: The Expanded Sloan Digital Sky Survey Hubble Space Telescope Sample," *The Astrophysical Journal*, vol. 636, no. 2, pp. 610–630, Jan. 2006.

[16] T. R. Miller, N. Arav, X. Xu, G. A. Kriss, and R. J. Plesha, "HST/COS Observations of Quasar Outflows in the 500-1050 ŠRest Frame. VII. Distances and Energetics for 11 Outflows in Five Quasars," *The Astrophysical Journal Supplement Series*, vol. 249, no. 1, p. 15, Jul. 2020.

[17] D. Byun, N. Arav, and P. B. Hall, "The Farthest Quasar Mini-Broad Absorption Line Outflow from Its Central Source: Very Large Telescope/UVES Observation of SDSS J0242+0049," *The Astrophysical Journal*, vol. 927, no. 2, p. 176, Mar. 2022.

[18] ——, "VLT/UVES observation of the SDSS J2357−0048 outflow," *Monthly Notices of the Royal Astronomical Society*, vol. 517, no. 1, pp. 1048–1057, 09 2022. [Online]. Available: https://doi.org/10.1093/mnras/stac2638

[19] D. Byun, N. Arav, and A. Walker, "VLT/UVES observation of the outflow in quasar SDSS J1439-0106," *Monthly Notices of the Royal Astronomical Society*, vol. 516, no. 1, pp. 100–105, 08 2022. [Online]. Available: https://doi.org/10.1093/mnras/stac2194

[20] D. Byun, N. Arav, M. Sharma, M. Dehghanian, and G. Walker, "Extreme FeLoBAL outflow in the VLT/UVES spectrum of quasar SDSS J1321−0041," *Astronomy and Astrophysics*, vol. 684, p. A158, Apr. 2024.

[21] G. J. Ferland, M. Chatzikos, F. Guzmán, M. L. Lykins, P. A. M. van Hoof, R. J. R. Williams, N. P. Abel, N. R. Badnell, F. P. Keenan, R. L. Porter, and P. C. Stancil, "The 2017 Release Cloudy," *Revista Mexicana de Astronomía y Astrofísica*, vol. 53, pp. 385–438, Oct. 2017.

[22] D. Byun, N. Arav, M. Dehghanian, G. Walker, and G. A. Kriss, "BAL outflow in quasar B0254-3327B: analysis and comparison with other extreme UV outflows," *Monthly Notices of the Royal Astronomical Society*, vol. 529, no. 4, pp. 3550–3562, Apr. 2024.

[23] A. Walker, N. Arav, and D. Byun, "High mass flow rate in a BAL outflow of quasar SDSS J1130 + 0411," *Monthly Notices of the Royal Astronomical Society*, vol. 516, no. 3, pp. 3778–3785, Nov. 2022.

[24] E. Kara, M. Mehdipour, G. A. Kriss, E. M. Cackett, N. Arav, A. J. Barth, D. Byun, M. S. Brotherton, G. De Rosa, J. Gelbord, J. V. Hernández Santisteban, C. Hu, J. Kaastra, H. Landt, Y.-R. Li, J. A. Miller, J. Montano, E. Partington, J. Aceituno, J.-M. Bai, D. Bao, M. C. Bentz, T. G. Brink, D. Chelouche, Y.-J. Chen, E. R. Colmenero, E. Dalla Bontà, M. Dehghanian, P. Du, R. Edelson, G. J. Ferland, L. Ferrarese, C. Fian, A. V. Filippenko, T. Fischer, M. R. Goad, D. H. González Buitrago, V. Gorjian, C. J. Grier, W.-J. Guo, P. B. Hall, L. C. Ho, Y. Homayouni, K. Horne, D. Ilić, B.-W. Jiang, M. D. Joner, S. Kaspi, C. S. Kochanek, K. T. Korista, D. Kynoch, S.-S. Li, J.-R. Liu, I. M. McHardy, J. N. McLane, J. A. J. Mitchell, H. Netzer, K. A. Olson, R. W. Pogge, L. Č. Popović, D. Proga, T. Storchi-Bergmann, E. Strasburger, T. Treu, M. Vestergaard, J.-M. Wang, M. J. Ward, T. Waters, P. R. Williams, S. Yang, Z.-H. Yao, T. E. Zastrocky, S. Zhai, and Y. Zu, "AGN STORM 2. I. First results: A Change in the Weather of Mrk 817," *The Astrophysical Journal*, vol. 922, no. 2, p. 151, Dec. 2021.

[25] E. R. Partington, E. M. Cackett, E. Kara, G. A. Kriss, A. J. Barth, G. De Rosa, Y. Homayouni, K. Horne, H. Landt, A. Zoghbi, R. Edelson, N. Arav, B. D. Boizelle, M. C. Bentz, M. S. Brotherton, D. Byun, E. Dalla Bontà, M. Dehghanian, P. Du, C. Fian, A. V. Filippenko, J. Gelbord, M. R. Goad, D. H. González Buitrago, C. J. Grier, P. B. Hall, C. Hu, D. Ilić, M. D. Joner, S. Kaspi, C. S. Kochanek, K. T. Korista, A. B. Kovačević, D. Kynoch, J. N. McLane, M. Mehdipour, J. A. Miller, C. Panagiotou, R. Plesha, L. Č. Popović, D. Proga, D. Rogantini, T. Storchi-Bergmann, D. Sanmartim, M. R. Siebert, M. Vestergaard, M. J. Ward, T. Waters, and F. Zaidouni, "AGN STORM 2. III. A NICER View of the Variable X-Ray Obscurer in Mrk 817," *The Astrophysical Journal*, vol. 947, no. 1, p. 2, Apr. 2023.

[26] M. Dehghanian, N. Arav, D. Byun, G. Walker, and M. Sharma, "Narrow absorption line outflow in Seyfert 1 galaxy J1429+4518: outflow's distance from the central source and its energetics," *Monthly Notices of the Royal Astronomical Society*, vol. 527, no. 3, pp. 7825–7834, Jan. 2024.

[27] C. Hazard, M. B. Mackey, and A. J. Shimmins, "Investigation of the Radio Source 3C 273 By The Method of Lunar Occultations," *Nature*, vol. 197, no. 4872, pp. 1037–1039, Mar. 1963.

[28] M. Schmidt, "3C 273 : A Star-Like Object with Large Red-Shift," *Nature*, vol. 197, no. 4872, p. 1040, Mar. 1963.

[29] J. B. Oke, "Absolute Energy Distribution in the Optical Spectrum of 3C 273," *Nature*, vol. 197, no. 4872, pp. 1040–1041, Mar. 1963.

[30] J. L. Greenstein and M. Schmidt, "The Quasi-Stellar Radio Sources 3C 48 and 3C 273." *The Astrophysical Journal*, vol. 140, p. 1, Jul. 1964.

[31] C. Hoffmeister, "354 neue Veränderliche," *Astronomische Nachrichten*, vol. 236, p. 233, Sep. 1929.

[32] J. L. Schmitt, "BL Lac identified as a Radio Source," *Nature*, vol. 218, no. 5142, p. 663, May 1968.

[33] J. B. Oke and J. E. Gunn, "The Distance of BL Lacertae," *The Astrophysical Journal*, vol. 189, p. L5, Apr. 1974.

[34] J. Silk and M. J. Rees, "Quasars and galaxy formation," *Astronomy & Astrophysics*, vol. 331, pp. L1–L4, Mar. 1998.

[35] F. Yuan, D. Yoon, Y.-P. Li, Z.-M. Gan, L. C. Ho, and F. Guo, "Active Galactic Nucleus Feedback in an Elliptical Galaxy with the Most Updated AGN Physics. I. Low Angular Momentum Case," *The Astrophysical Journal*, vol. 857, no. 2, p. 121, Apr. 2018.

[36] A. Vayner, S. A. Wright, N. Murray, L. Armus, A. Boehle, M. Cosens, J. E. Larkin, E. Mieda, and G. Walth, "A Spatially Resolved Survey of Distant Quasar Host Galaxies. I. Dynamics of Galactic Outflows," *The Astrophysical Journal*, vol. 919, no. 2, p. 122, Oct. 2021.

[37] P. C. Hewett and C. B. Foltz, "The Frequency and Radio Properties of Broad Absorption Line Quasars," *The Astronomical Journal*, vol. 125, no. 4, pp. 1784–1794, Apr. 2003.

[38] X. Dai, F. Shankar, and G. R. Sivakoff, "2MASS Reveals a Large Intrinsic Fraction of BALQSOs," *The Astrophysical Journal*, vol. 672, no. 1, pp. 108–114, Jan. 2008.

[39] R. D. Blandford and M. C. Begelman, "Two-dimensional adiabatic flows on to a black

hole - I. Fluid accretion," *Monthly Notices of the Royal Astronomical Society,* vol. 349, no. 1, pp. 68–86, Mar. 2004.

[40] P. F. Hopkins, N. Murray, and T. A. Thompson, "The small scatter in BH-host correlations and the case for self-regulated BH growth," *Monthly Notices of the Royal Astronomical Society,* vol. 398, no. 1, pp. 303–311, Sep. 2009.

[41] J. P. Ostriker, E. Choi, L. Ciotti, G. S. Novak, and D. Proga, "Momentum Driving: Which Physical Processes Dominate Active Galactic Nucleus Feedback?" *The Astrophysical Journal,* vol. 722, no. 1, pp. 642–652, Oct. 2010.

[42] Y. Dubois, M. Volonteri, and J. Silk, "Black hole evolution - III. Statistical properties of mass growth and spin evolution using large-scale hydrodynamical cosmological simulations," *Monthly Notices of the Royal Astronomical Society,* vol. 440, no. 2, pp. 1590–1606, May 2014.

[43] Y. M. Rosas-Guevara, R. G. Bower, J. Schaye, M. Furlong, C. S. Frenk, C. M. Booth, R. A. Crain, C. Dalla Vecchia, M. Schaller, and T. Theuns, "The impact of angular momentum on black hole accretion rates in simulations of galaxy formation," *Monthly Notices of the Royal Astronomical Society,* vol. 454, no. 1, pp. 1038–1057, Nov. 2015.

[44] M. Volonteri, Y. Dubois, C. Pichon, and J. Devriendt, "The cosmic evolution of massive black holes in the Horizon-AGN simulation," *Monthly Notices of the Royal Astronomical Society,* vol. 460, no. 3, pp. 2979–2996, Aug. 2016.

[45] D. Anglés-Alcázar, R. Davé, C.-A. Faucher-Giguère, F. Özel, and P. F. Hopkins, "Gravitational torque-driven black hole growth and feedback in cosmological simulations," *Monthly Notices of the Royal Astronomical Society,* vol. 464, no. 3, pp. 2840–2853, Jan. 2017.

[46] J. Magorrian, S. Tremaine, D. Richstone, R. Bender, G. Bower, A. Dressler, S. M. Faber, K. Gebhardt, R. Green, C. Grillmair, J. Kormendy, and T. Lauer, "The Demography of Massive Dark Objects in Galaxy Centers," *The Astronomical Journal*, vol. 115, no. 6, pp. 2285–2305, Jun. 1998.

[47] L. Ciotti, J. P. Ostriker, and D. Proga, "Feedback from Central Black Holes in Elliptical Galaxies. I. Models with Either Radiative or Mechanical Feedback but not Both," *The Astrophysical Journal*, vol. 699, no. 1, pp. 89–104, Jul. 2009.

[48] C.-A. Faucher-Giguère, E. Quataert, and N. Murray, "A physical model of FeLoBALs: implications for quasar feedback," *Monthly Notices of the Royal Astronomical Society*, vol. 420, no. 2, pp. 1347–1354, Feb. 2012.

[49] K. Zubovas and A. R. King, "Galaxy-wide outflows: cold gas and star formation at high speeds," *Monthly Notices of the Royal Astronomical Society*, vol. 439, no. 1, pp. 400–406, Mar. 2014.

[50] J. Schaye, R. A. Crain, R. G. Bower, M. Furlong, M. Schaller, T. Theuns, C. Dalla Vecchia, C. S. Frenk, I. G. McCarthy, J. C. Helly, A. Jenkins, Y. M. Rosas-Guevara, S. D. M. White, M. Baes, C. M. Booth, P. Camps, J. F. Navarro, Y. Qu, A. Rahmati, T. Sawala, P. A. Thomas, and J. Trayford, "The EAGLE project: simulating the evolution and assembly of galaxies and their environments," *Monthly Notices of the Royal Astronomical Society*, vol. 446, no. 1, pp. 521–554, Jan. 2015.

[51] E. Choi, J. P. Ostriker, T. Naab, R. S. Somerville, M. Hirschmann, A. Núñez, C.-Y. Hu, and L. Oser, "Physics of Galactic Metals: Evolutionary Effects due to Production, Distribution, Feedback, and Interaction with Black Holes," *The Astrophysical Journal*, vol. 844, no. 1, p. 31, Jul. 2017.

[52] S. Peirani, Y. Dubois, M. Volonteri, J. Devriendt, K. Bundy, J. Silk, C. Pichon, S. Kaviraj, R. Gavazzi, and M. Habouzit, "Density profile of dark matter haloes and galaxies in the HORIZON-AGN simulation: the impact of AGN feedback," *Monthly Notices of the Royal Astronomical Society*, vol. 472, no. 2, pp. 2153–2169, Dec. 2017.

[53] E. Scannapieco and S. P. Oh, "Quasar Feedback: The Missing Link in Structure Formation," *The Astrophysical Journal*, vol. 608, no. 1, pp. 62–79, Jun. 2004.

[54] A. Khalatyan, A. Cattaneo, M. Schramm, S. Gottlöber, M. Steinmetz, and L. Wisotzki, "Is AGN feedback necessary to form red elliptical galaxies?" *Monthly Notices of the Royal Astronomical Society*, vol. 387, no. 1, pp. 13–30, Jun. 2008.

[55] P. Barai, D. Proga, and K. Nagamine, "Smoothed particle hydrodynamics simulations of black hole accretion: a step to model black hole feedback in galaxies," *Monthly Notices of the Royal Astronomical Society*, vol. 418, no. 1, pp. 591–611, Nov. 2011.

[56] P. Taylor and C. Kobayashi, "Quantifying AGN-driven metal-enhanced outflows in chemodynamical simulations," *Monthly Notices of the Royal Astronomical Society*, vol. 452, no. 1, pp. L59–L63, Sep. 2015.

[57] T. A. Thompson, A. C. Fabian, E. Quataert, and N. Murray, "Dynamics of dusty radiation-pressure-driven shells and clouds: fast outflows from galaxies, star clusters, massive stars, and AGN," *Monthly Notices of the Royal Astronomical Society*, vol. 449, no. 1, pp. 147–161, May 2015.

[58] P. F. Hopkins and M. Elvis, "Quasar feedback: more bang for your buck," *Monthly Notices of the Royal Astronomical Society*, vol. 401, no. 1, pp. 7–14, Jan. 2010.

[59] A. Hewitt and G. Burbidge, "A Revised and Updated Catalog of Quasi-stellar Objects," *The Astrophysical Journal Supplemental Series*, vol. 87, p. 451, Aug. 1993.

[60] D. J. Whalen, M. A. Latif, and M. Mezcua, "Radio emission from a z = 10.1 black hole in uhz1," *The Astrophysical Journal*, vol. 956, no. 2, p. 133, oct 2023. [Online]. Available: https://dx.doi.org/10.3847/1538-4357/acf92c

[61] C. Ilie, K. Freese, A. Petric, and J. Paulin, "UHZ1 and the other three most distant quasars observed: possible evidence for Supermassive Dark Stars," *arXiv e-prints*, p. arXiv:2312.13837, Dec. 2023.

[62] M. Krips, S. Martín, A. Eckart, R. Neri, S. García-Burillo, S. Matsushita, A. Peck, I. Stoklasová, G. Petitpas, A. Usero, F. Combes, E. Schinnerer, L. Humphreys, and A. J. Baker, "Submillimeter array/plateau de bure interferometer multiple line observations of the nearby seyfert 2 galaxy ngc 1068: Shock-related gas kinematics and heating in the central 100 pc?*," *The Astrophysical Journal*, vol. 736, no. 1, p. 37, jul 2011. [Online]. Available: https://dx.doi.org/10.1088/0004-637X/736/1/37

[63] C. Cicone, R. Maiolino, E. Sturm, J. Graciá-Carpio, C. Feruglio, R. Neri, S. Aalto, R. Davies, F. Fiore, J. Fischer, S. García-Burillo, E. González-Alfonso, S. Hailey-Dunsheath, E. Piconcelli, and S. Veilleux, "Massive molecular outflows and evidence for AGN feedback from CO observations," *Astronomy and Astrophysics*, vol. 562, p. A21, Feb. 2014.

[64] C. Feruglio, F. Fiore, S. Carniani, E. Piconcelli, L. Zappacosta, A. Bongiorno, C. Cicone, R. Maiolino, A. Marconi, N. Menci, S. Puccetti, and S. Veilleux, "The multi-phase winds of Markarian 231: from the hot, nuclear, ultra-fast wind to the galaxy-scale, molecular outflow," *Astronomy and Astrophysics*, vol. 583, p. A99, Nov. 2015.

[65] N. Kanekar and J. N. Chengalur, "Outflowing atomic and molecular gas at z $\sim$0.67 towards 1504 + 377," *Monthly Notices of the Royal Astronomical Society*, vol. 384, no. 1, pp. L6–L10, Feb. 2008.

[66] J. N. H. S. Aditya and N. Kanekar, "A Giant Metrewave Radio Telescope survey for associated H I 21 cm absorption in the Caltech-Jodrell flat-spectrum sample," *Monthly Notices of the Royal Astronomical Society,* vol. 481, no. 2, pp. 1578–1596, Dec. 2018.

[67] D. S. N. Rupke and S. Veilleux, "The Multiphase Structure and Power Sources of Galactic Winds in Major Mergers," *The Astrophysical Journal,* vol. 768, no. 1, p. 75, May 2013.

[68] C. M. Harrison, D. M. Alexander, J. R. Mullaney, and A. M. Swinbank, "Kiloparsec-scale outflows are prevalent among luminous AGN: outflows and feedback in the context of the overall AGN population," *Monthly Notices of the Royal Astronomical Society,* vol. 441, no. 4, pp. 3306–3347, Jul. 2014.

[69] M. Bischetti, E. Piconcelli, G. Vietri, A. Bongiorno, F. Fiore, E. Sani, A. Marconi, F. Duras, L. Zappacosta, M. Brusa, A. Comastri, G. Cresci, C. Feruglio, E. Giallongo, F. La Franca, V. Mainieri, F. Mannucci, S. Martocchia, F. Ricci, R. Schneider, V. Testa, and C. Vignali, "The WISSH quasars project. I. Powerful ionised outflows in hyper-luminous quasars," *Astronomy and Astrophysics,* vol. 598, p. A122, Feb. 2017.

[70] K. T. Korista, M. A. Bautista, N. Arav, M. Moe, E. Costantini, and C. Benn, "Physical Conditions in Quasar Outflows: Very Large Telescope Observations of QSO 2359-1241," *The Astrophysical Journal,* vol. 688, no. 1, pp. 108–115, Nov. 2008.

[71] J. P. Dunn, M. Bautista, N. Arav, M. Moe, K. Korista, E. Costantini, C. Benn, S. Ellison, and D. Edmonds, "The Quasar Outflow Contribution to AGN Feedback: VLT Measurements of SDSS J0318-0600," *The Astrophysical Journal,* vol. 709, no. 2, pp. 611–631, Feb. 2010.

[72] Y. Shen, G. T. Richards, M. A. Strauss, P. B. Hall, D. P. Schneider, S. Snedden, D. Bizyaev, H. Brewington, V. Malanushenko, E. Malanushenko, D. Oravetz, K. Pan,

and A. Simmons, "A Catalog of Quasar Properties from Sloan Digital Sky Survey Data Release 7," *The Astrophysical Journal Supplemental Series*, vol. 194, no. 2, p. 45, Jun. 2011.

[73] G. Chartas, C. Saez, W. N. Brandt, M. Giustini, and G. P. Garmire, "Confirmation of and Variable Energy Injection by a Near-Relativistic Outflow in APM 08279+5255," *The Astrophysical Journal*, vol. 706, no. 1, pp. 644–656, Nov. 2009.

[74] E. Nardini, J. N. Reeves, J. Gofford, F. A. Harrison, G. Risaliti, V. Braito, M. T. Costa, G. A. Matzeu, D. J. Walton, E. Behar, S. E. Boggs, F. E. Christensen, W. W. Craig, C. J. Hailey, G. Matt, J. M. Miller, P. T. O'Brien, D. Stern, T. J. Turner, and M. J. Ward, "Black hole feedback in the luminous quasar PDS 456," *Science*, vol. 347, no. 6224, pp. 860–863, Feb. 2015.

[75] F. Tombesi, M. Meléndez, S. Veilleux, J. N. Reeves, E. González-Alfonso, and C. S. Reynolds, "Wind from the black-hole accretion disk driving a molecular outflow in an active galaxy," *Nature*, vol. 519, no. 7544, pp. 436–438, Mar. 2015.

[76] R. J. Weymann, S. L. Morris, C. B. Foltz, and P. C. Hewett, "Comparisons of the Emission-Line and Continuum Properties of Broad Absorption Line and Normal Quasi-stellar Objects," *The Astrophysical Journal*, vol. 373, p. 23, May 1991.

[77] X. Xu, N. Arav, T. Miller, and C. Benn, "VLT/X-Shooter Survey of BAL Quasars: Large Distance Scale and AGN Feedback," *The Astrophysical Journal*, vol. 876, no. 2, p. 105, May 2019.

[78] G. A. Kriss, M. Mehdipour, J. S. Kaastra, A. Rau, J. Bodensteiner, R. Plesha, N. Arav, E. Behar, S. Bianchi, G. Branduardi-Raymont, M. Cappi, E. Costantini, B. De Marco, L. Di Gesu, J. Ebrero, S. Kaspi, J. Mao, R. Middei, T. Miller, S. Paltani, U. Peretz,

B. M. Peterson, P. O. Petrucci, G. Ponti, F. Ursini, D. J. Walton, and X. Xu, "HST/COS observations of the newly discovered obscuring outflow in NGC 3783," *Astronomy and Astrophysics*, vol. 621, p. A12, Jan. 2019.

[79] T. R. Miller, N. Arav, X. Xu, G. A. Kriss, R. J. Plesha, C. Benn, and G. Liu, "Distance, Energy, and Variability of Quasar Outflows: Two HST/COS Epochs of LBQS 1206+1052," *The Astrophysical Journal*, vol. 865, no. 2, p. 90, Oct. 2018.

[80] X. Xu, N. Arav, T. Miller, K. T. Korista, and C. Benn, "Physical conditions of iron-peak low-ionization lines in the FeLoBAL quasar Q0059-2735," *Monthly Notices of the Royal Astronomical Society*, vol. 506, no. 2, pp. 2725–2738, Sep. 2021.

[81] F. Hamann and B. Sabra, "The Diverse Nature of Intrinsic Absorbers in AGNs," in *AGN Physics with the Sloan Digital Sky Survey*, ser. Astronomical Society of the Pacific Conference Series, G. T. Richards and P. B. Hall, Eds., vol. 311, Jun. 2004, p. 203.

[82] T. R. Miller, N. Arav, X. Xu, G. A. Kriss, and R. J. Plesha, "HST/COS Observations of Quasar Outflows in the 500-1050 Å Rest Frame. III. Four Similar Outflows in 2MASS J1051+1247 with Enough Energy to Be Major Contributors to AGN Feedback," *The Astrophysical Journal Supplement Series*, vol. 247, no. 2, p. 39, Apr. 2020.

[83] D. E. Osterbrock and G. J. Ferland, *Astrophysics of Gaseous Nebulae and Active Galactic Nuclei*. University Science Books, 2006.

[84] H. Choi, K. M. Leighly, D. M. Terndrup, C. Dabbieri, S. C. Gallagher, and G. T. Richards, "The Physical Properties of Low-redshift FeLoBAL Quasars. I. Spectral-synthesis Analysis of the Broad Absorption-line (BAL) Outflows Using SimBAL," *The Astrophysical Journal*, vol. 937, no. 2, p. 74, Oct. 2022.

[85] H. Choi, K. M. Leighly, C. Dabbieri, D. M. Terndrup, S. C. Gallagher, and G. T.

Richards, "The Physical Properties of Low-redshift FeLoBAL Quasars. III. The Location and Geometry of the Outflows," *The Astrophysical Journal*, vol. 936, no. 2, p. 110, Sep. 2022.

[86] X. Xu, N. Arav, T. Miller, G. A. Kriss, and R. Plesha, "HST/COS Observations of Quasar Outflows in the 500-1050 Å Rest Frame. II. The Most Energetic Quasar Outflow Measured to Date," *The Astrophysical Journal Supplement Series*, vol. 247, no. 2, p. 38, Apr. 2020.

[87] G. Liu, N. L. Zakamska, J. E. Greene, N. P. H. Nesvadba, and X. Liu, "Observations of feedback from radio-quiet quasars - II. Kinematics of ionized gas nebulae," *Monthly Notices of the Royal Astronomical Society*, vol. 436, no. 3, pp. 2576–2597, Dec. 2013.

[88] C. Knigge, S. Scaringi, M. R. Goad, and C. E. Cottis, "The intrinsic fraction of broad-absorption line quasars," *Monthly Notices of the Royal Astronomical Society*, vol. 386, no. 3, pp. 1426–1435, May 2008.

[89] M. Moe, N. Arav, M. A. Bautista, and K. T. Korista, "Quasar Outflow Contribution to AGN Feedback: Observations of QSO SDSS J0838+2955," *The Astrophysical Journal*, vol. 706, no. 1, pp. 525–534, Nov. 2009.

[90] C. Chamberlain, N. Arav, and C. Benn, "Strong candidate for AGN feedback: VLT/X-shooter observations of BALQSO SDSS J0831+0354," *Monthly Notices of the Royal Astronomical Society*, vol. 450, no. 1, pp. 1085–1093, Jun. 2015.

[91] X. Xu, N. Arav, T. Miller, G. A. Kriss, and R. Plesha, "HST/COS Observations of Quasar Outflows in the 500-1050 Å Rest Frame. VI. Wide, Energetic Outflows in SDSS J0755+2306," *The Astrophysical Journal Supplement Series*, vol. 247, no. 2, p. 42, Apr. 2020.

[92] B. C. J. Borguet, D. Edmonds, N. Arav, C. Benn, and C. Chamberlain, "BAL Phosphorus Abundance and Evidence for Immense Ionic Column Densities in Quasar Outflows: VLT/X-Shooter Observations of Quasar SDSS J1512+1119," *The Astrophysical Journal*, vol. 758, no. 1, p. 69, Oct. 2012.

[93] M. de Kool, N. Arav, R. H. Becker, M. D. Gregg, R. L. White, S. A. Laurent-Muehleisen, T. Price, and K. T. Korista, "Keck HIRES Observations of the QSO FIRST J104459.6+365605: Evidence for a Large-Scale Outflow," *The Astrophysical Journal*, vol. 548, no. 2, pp. 609–623, Feb. 2001.

[94] M. de Kool, R. H. Becker, M. D. Gregg, R. L. White, and N. Arav, "Intrinsic Absorption in the QSO FIRST J121442.3+280329," *The Astrophysical Journal*, vol. 567, no. 1, pp. 58–67, Mar. 2002.

[95] F. W. Hamann, T. A. Barlow, F. C. Chaffee, C. B. Foltz, and R. J. Weymann, "High-Resolution Keck Spectra of the Associated Absorption Lines in 3C 191," *The Astrophysical Journal*, vol. 550, no. 1, pp. 142–152, Mar. 2001.

[96] J. R. Gabel, S. B. Kraemer, D. M. Crenshaw, I. M. George, W. N. Brandt, F. W. Hamann, M. E. Kaiser, S. Kaspi, G. A. Kriss, S. Mathur, K. Nandra, H. Netzer, B. M. Peterson, J. C. Shields, T. J. Turner, and W. Zheng, "The Ionized Gas and Nuclear Environment in NGC 3783. V. Variability and Modeling of the Intrinsic Ultraviolet Absorption," *The Astrophysical Journal*, vol. 631, no. 2, pp. 741–761, Oct. 2005.

[97] N. Arav, G. Liu, X. Xu, J. Stidham, C. Benn, and C. Chamberlain, "Evidence that 50% of BALQSO Outflows Are Situated at Least 100 pc from the Central Source," *The Astrophysical Journal*, vol. 857, no. 1, p. 60, Apr. 2018.

[98] P. B. Hall, S. I. Sadavoy, D. Hutsemekers, J. E. Everett, and A. Rafiee, "Acceleration

and Substructure Constraints in a Quasar Outflow," *The Astrophysical Journal*, vol. 665, no. 1, pp. 174–186, Aug. 2007.

[99] C. L. Bennett, D. Larson, J. L. Weiland, and G. Hinshaw, "THE 1% CONCORDANCE HUBBLE CONSTANT," *The Astrophysical Journal*, vol. 794, no. 2, p. 135, oct 2014. [Online]. Available: https://doi.org/10.1088/0004-637x/794/2/135

[100] Astropy Collaboration, T. P. Robitaille, E. J. Tollerud, P. Greenfield, M. Droettboom, E. Bray, T. Aldcroft, M. Davis, A. Ginsburg, A. M. Price-Whelan, W. E. Kerzendorf, A. Conley, N. Crighton, K. Barbary, D. Muna, H. Ferguson, F. Grollier, M. M. Parikh, P. H. Nair, H. M. Unther, C. Deil, J. Woillez, S. Conseil, R. Kramer, J. E. H. Turner, L. Singer, R. Fox, B. A. Weaver, V. Zabalza, Z. I. Edwards, K. Azalee Bostroem, D. J. Burke, A. R. Casey, S. M. Crawford, N. Dencheva, J. Ely, T. Jenness, K. Labrie, P. L. Lim, F. Pierfederici, A. Pontzen, A. Ptak, B. Refsdal, M. Servillat, and O. Streicher, "Astropy: A community Python package for astronomy," *Astronomy & Astrophysics*, vol. 558, p. A33, Oct. 2013.

[101] Astropy Collaboration, A. M. Price-Whelan, B. M. Sipőcz, H. M. Günther, P. L. Lim, S. M. Crawford, S. Conseil, D. L. Shupe, M. W. Craig, N. Dencheva, A. Ginsburg, J. T. Vand erPlas, L. D. Bradley, D. Pérez-Suárez, M. de Val-Borro, T. L. Aldcroft, K. L. Cruz, T. P. Robitaille, E. J. Tollerud, C. Ardelean, T. Babej, Y. P. Bach, M. Bachetti, A. V. Bakanov, S. P. Bamford, G. Barentsen, P. Barmby, A. Baumbach, K. L. Berry, F. Biscani, M. Boquien, K. A. Bostroem, L. G. Bouma, G. B. Brammer, E. M. Bray, H. Breytenbach, H. Buddelmeijer, D. J. Burke, G. Calderone, J. L. Cano Rodríguez, M. Cara, J. V. M. Cardoso, S. Cheedella, Y. Copin, L. Corrales, D. Crichton, D. D'Avella, C. Deil, É. Depagne, J. P. Dietrich, A. Donath, M. Droettboom, N. Earl, T. Erben, S. Fabbro, L. A. Ferreira, T. Finethy, R. T. Fox, L. H. Garrison, S. L. J. Gibbons, D. A. Goldstein, R. Gommers, J. P. Greco, P. Greenfield, A. M.

Groener, F. Grollier, A. Hagen, P. Hirst, D. Homeier, A. J. Horton, G. Hosseinzadeh, L. Hu, J. S. Hunkeler, Ž. Ivezić, A. Jain, T. Jenness, G. Kanarek, S. Kendrew, N. S. Kern, W. E. Kerzendorf, A. Khvalko, J. King, D. Kirkby, A. M. Kulkarni, A. Kumar, A. Lee, D. Lenz, S. P. Littlefair, Z. Ma, D. M. Macleod, M. Mastropietro, C. McCully, S. Montagnac, B. M. Morris, M. Mueller, S. J. Mumford, D. Muna, N. A. Murphy, S. Nelson, G. H. Nguyen, J. P. Ninan, M. Nöthe, S. Ogaz, S. Oh, J. K. Parejko, N. Parley, S. Pascual, R. Patil, A. A. Patil, A. L. Plunkett, J. X. Prochaska, T. Rastogi, V. Reddy Janga, J. Sabater, P. Sakurikar, M. Seifert, L. E. Sherbert, H. Sherwood-Taylor, A. Y. Shih, J. Sick, M. T. Silbiger, S. Singanamalla, L. P. Singer, P. H. Sladen, K. A. Sooley, S. Sornarajah, O. Streicher, P. Teuben, S. W. Thomas, G. R. Tremblay, J. E. H. Turner, V. Terrón, M. H. van Kerkwijk, A. de la Vega, L. L. Watkins, B. A. Weaver, J. B. Whitmore, J. Woillez, V. Zabalza, and Astropy Contributors, "The Astropy Project: Building an Open-science Project and Status of the v2.0 Core Package," *The Astronomical Journal*, vol. 156, no. 3, p. 123, Sep. 2018.

[102] I. Pâris, P. Petitjean, É. Aubourg, A. D. Myers, A. Streblyanska, B. W. Lyke, S. F. Anderson, É. Armengaud, J. Bautista, M. R. Blanton, M. Blomqvist, J. Brinkmann, J. R. Brownstein, W. N. Brandt, É. Burtin, K. Dawson, S. de la Torre, A. Georgakakis, H. Gil-Marín, P. J. Green, P. B. Hall, J.-P. Kneib, S. M. LaMassa, J.-M. Le Goff, C. MacLeod, V. Mariappan, I. D. McGreer, A. Merloni, P. Noterdaeme, N. Palanque-Delabrouille, W. J. Percival, A. J. Ross, G. Rossi, D. P. Schneider, H.-J. Seo, R. Tojeiro, B. A. Weaver, A.-M. Weijmans, C. Yèche, P. Zarrouk, and G.-B. Zhao, "The Sloan Digital Sky Survey Quasar Catalog: Fourteenth data release," *Astronomy & Astrophysics*, vol. 613, p. A51, May 2018.

[103] C. Chen, F. Hamann, B. Ma, and M. Murphy, "A Catalog of High-velocity C IV

Mini-broad Absorption Lines in the VLT-UVES and Keck-HIRES Archives," *The Astrophysical Journal*, vol. 907, no. 2, p. 84, Feb. 2021.

[104] E. F. Schlafly and D. P. Finkbeiner, "Measuring Reddening with Sloan Digital Sky Survey Stellar Spectra and Recalibrating SFD," *The Astrophysical Journal*, vol. 737, no. 2, p. 103, Aug. 2011.

[105] D. P. Schneider, G. T. Richards, P. B. Hall, M. A. Strauss, S. F. Anderson, T. A. Boroson, N. P. Ross, Y. Shen, W. N. Brandt, X. Fan, N. Inada, S. Jester, G. R. Knapp, C. M. Krawczyk, A. R. Thakar, D. E. Vanden Berk, W. Voges, B. Yanny, D. G. York, N. A. Bahcall, D. Bizyaev, M. R. Blanton, H. Brewington, J. Brinkmann, D. Eisenstein, J. A. Frieman, M. Fukugita, J. Gray, J. E. Gunn, P. Hibon, Ž. Ivezić, S. M. Kent, R. G. Kron, M. G. Lee, R. H. Lupton, E. Malanushenko, V. Malanushenko, D. Oravetz, K. Pan, J. R. Pier, I. Price, Ted N., D. H. Saxe, D. J. Schlegel, A. Simmons, S. A. Snedden, M. U. SubbaRao, A. S. Szalay, and D. H. Weinberg, "The Sloan Digital Sky Survey Quasar Catalog. V. Seventh Data Release," *The Astronomical Journal*, vol. 139, no. 6, p. 2360, Jun. 2010.

[106] S. A. Smee, J. E. Gunn, A. Uomoto, N. Roe, D. Schlegel, C. M. Rockosi, M. A. Carr, F. Leger, K. S. Dawson, M. D. Olmstead, J. Brinkmann, R. Owen, R. H. Barkhouser, K. Honscheid, P. Harding, D. Long, R. H. Lupton, C. Loomis, L. Anderson, J. Annis, M. Bernardi, V. Bhardwaj, D. Bizyaev, A. S. Bolton, H. Brewington, J. W. Briggs, S. Burles, J. G. Burns, F. J. Castander, A. Connolly, J. R. A. Davenport, G. Ebelke, H. Epps, P. D. Feldman, S. D. Friedman, J. Frieman, T. Heckman, C. L. Hull, G. R. Knapp, D. M. Lawrence, J. Loveday, E. J. Mannery, E. Malanushenko, V. Malanushenko, A. J. Merrelli, D. Muna, P. R. Newman, R. C. Nichol, D. Oravetz, K. Pan, A. C. Pope, P. G. Ricketts, A. Shelden, D. Sandford, W. Siegmund, A. Simmons, D. S. Smith, S. Snedden, D. P. Schneider, M. SubbaRao, C. Tremonti, P. Wad-

dell, and D. G. York, "The Multi-object, Fiber-fed Spectrographs for the Sloan Digital Sky Survey and the Baryon Oscillation Spectroscopic Survey," *The Astronomical Journal*, vol. 146, no. 2, p. 32, Aug. 2013.

[107] B. D. Savage and K. R. Sembach, "The analysis of apparent optical depth profiles for interstellar absorption lines," *The Astrophysical Journal*, vol. 379, p. 245, sep 1991. [Online]. Available: http://adsabs.harvard.edu/doi/10.1086/170498

[108] T. A. Barlow, F. Hamann, and W. L. W. Sargent, "Partial Coverage and Time Variability of Narrow-Line Intrinsic QSO Absorption Systems," in *Mass Ejection from Active Galactic Nuclei*, ser. Astronomical Society of the Pacific Conference Series, N. Arav, I. Shlosman, and R. J. Weymann, Eds., vol. 128, Jan. 1997, p. 13.

[109] N. Arav, R. H. Becker, S. A. Laurent-Muehleisen, M. D. Gregg, R. L. White, M. S. Brotherton, and M. de Kool, "What Determines the Depth of Broad Absorption Lines? Keck HIRES Observations of BALQSO 1603+3002," *The Astrophysical Journal*, vol. 524, no. 2, pp. 566–571, Oct. 1999.

[110] N. Arav, K. T. Korista, M. de Kool, V. T. Junkkarinen, and M. C. Begelman, "Hubble Space Telescope Observations of the Broad Absorption Line QuasarPG 0946+301," *The Astrophysical Journal*, vol. 516, no. 1, pp. 27–46, may 1999. [Online]. Available: https://iopscience.iop.org/article/10.1086/307073

[111] M. de Kool, K. T. Korista, and N. Arav, "The Effects of Inhomogeneous Absorbers on the Formation of Intrinsic Quasar Absorption Lines," *The Astrophysical Journal*, vol. 580, no. 1, pp. 54–62, nov 2002. [Online]. Available: https://ui.adsabs.harvard.edu/abs/2002ApJ...580...54D/abstract

[112] N. Arav, J. Kaastra, G. A. Kriss, K. T. Korista, J. Gabel, and D. Proga, "X-Ray/

Ultraviolet Campaign on the Mrk 279 AGN Outflow: Constraining Inhomogeneous Absorber Models," *The Astrophysical Journal*, vol. 620, no. 2, pp. 665–672, Feb. 2005.

[113] D. Edmonds, B. Borguet, N. Arav, J. P. Dunn, S. Penton, G. A. Kriss, K. Korista, E. Costantini, K. Steenbrugge, J. I. Gonzalez-Serrano, K. Aoki, M. Bautista, E. Behar, C. Benn, D. M. Crenshaw, J. Everett, J. Gabel, J. Kaastra, M. Moe, and J. Scott, "Galactic-scale Absorption Outflow in the Low-luminosity Quasar IRAS F04250-5718: Hubble Space Telescope/Cosmic Origins Spectrograph Observations," *The Astrophysical Journal*, vol. 739, no. 1, p. 7, Sep. 2011.

[114] B. Borguet, D. Edmonds, N. Arav, J. Dunn, and G. A. Kriss, "A 10 kpc Scale Seyfert Galaxy Outflow: HST/COS Observations of IRAS F22456-5125," *The Astrophysical Journal*, vol. 751, no. 2, p. 107, may 2012. [Online]. Available: http://arxiv.org/abs/1205.0189http://dx.doi.org/10.1088/0004-637X/751/2/107

[115] J. R. Gabel, N. Arav, and T.-S. Kim, "The AGN Outflow in the HDF-S Target QSO J2233-606 from a High-Resolution VLT UVES Spectrum," *The Astrophysical Journal*, vol. 646, no. 2, pp. 742–753, Aug. 2006.

[116] J. T. Allen, P. C. Hewett, N. Maddox, G. T. Richards, and V. Belokurov, "A strong redshift dependence of the broad absorption line quasar fraction," *Monthly Notices of the Royal Astronomical Society*, vol. 410, no. 2, pp. 860–884, Jan. 2011.

[117] G. T. Richards, M. Lacy, L. J. Storrie-Lombardi, P. B. Hall, S. C. Gallagher, D. C. Hines, X. Fan, C. Papovich, D. E. Vanden Berk, G. B. Trammell, D. P. Schneider, M. Vestergaard, D. G. York, S. Jester, S. F. Anderson, T. Budavári, and A. S. Szalay, "Spectral Energy Distributions and Multiwavelength Selection of Type 1 Quasars," *The Astrophysical Journal Supplement Series*, vol. 166, no. 2, pp. 470–497, Oct. 2006.

[118] B. C. J. Borguet, D. Edmonds, N. Arav, J. Dunn, and G. A. Kriss, "A 10 kpc Scale Seyfert Galaxy Outflow: HST/COS Observations of IRAS F22456-5125," *The Astrophysical Journal*, vol. 751, no. 2, p. 107, Jun. 2012.

[119] D. C. Abbott, "The theory of radiatively driven stellar winds. II. The line acceleration." *The Astrophysical Journal*, vol. 259, pp. 282–301, Aug. 1982.

[120] N. Arav and Z.-Y. Li, "The Role of Radiative Acceleration in Outflows from Broad Absorption Line QSOs. I. Comparison with O Star Winds," *The Astrophysical Journal*, vol. 427, p. 700, Jun. 1994.

[121] L. B. Lucy and D. C. Abbott, "Multiline Transfer and the Dynamics of Wolf-Rayet Winds," *The Astrophysical Journal*, vol. 405, p. 738, Mar. 1993.

[122] X. Xu, N. Arav, T. Miller, G. A. Kriss, and R. Plesha, "HST/COS Observations of Quasar Outflows in the 500-1050 Å Rest Frame. IV. The Largest Broad Absorption Line Acceleration," *The Astrophysical Journal Supplement Series*, vol. 247, no. 2, p. 40, Apr. 2020.

[123] H. Bahk, J.-H. Woo, and D. Park, "Calibrating Mg II-based Black Hole Mass Estimators with Hβ Reverberation Measurements," *The Astrophysical Journal*, vol. 875, no. 1, p. 50, Apr. 2019.

[124] Y. Tsuzuki, K. Kawara, Y. Yoshii, S. Oyabu, T. Tanabé, and Y. Matsuoka, "Fe II Emission in 14 Low-Redshift Quasars. I. Observations," *The Astrophysical Journal*, vol. 650, no. 1, pp. 57–79, Oct. 2006.

[125] J.-H. Woo, H. A. N. Le, M. Karouzos, D. Park, D. Park, M. A. Malkan, T. Treu, and V. N. Bennert, "Calibration and Limitations of the Mg II Line-based Black Hole Masses," *The Astrophysical Journal*, vol. 859, no. 2, p. 138, Jun. 2018.

[126] W. G. Mathews and G. J. Ferland, "What Heats the Hot Phase in Active Nuclei?" *The Astrophysical Journal*, vol. 323, p. 456, Dec. 1987.

[127] M. A. Bautista, J. P. Dunn, N. Arav, K. T. Korista, M. Moe, and C. Benn, "Distance to Multiple Kinematic Components of Quasar Outflows: Very Large Telescope Observations of QSO 2359-1241 and SDSS J0318-0600," *The Astrophysical Journal*, vol. 713, no. 1, pp. 25–31, Apr. 2010.

[128] L. Sun, H. Zhou, T. Ji, P. Jiang, B. Liu, W. Liu, X. Pan, X. Shi, J. Wang, T. Wang, C. Yang, S. Zhang, and L. P. Miller, "Photoionization-driven Absorption-line Variability in Balmer Absorption Line Quasar LBQS 1206+1052," *The Astrophysical Journal*, vol. 838, no. 2, p. 88, Apr. 2017.

[129] R. Maiolino, S. Gallerani, R. Neri, C. Cicone, A. Ferrara, R. Genzel, D. Lutz, E. Sturm, L. J. Tacconi, F. Walter, C. Feruglio, F. Fiore, and E. Piconcelli, "Evidence of strong quasar feedback in the early Universe," *Monthly Notices of the Royal Astronomical Society*, vol. 425, no. 1, pp. L66–L70, Sep. 2012.

[130] Z. He, G. Liu, T. Wang, G. Mou, R. Green, W. Bian, H. Wang, L. C. Ho, M. Sun, L. Shen, N. Arav, C. Chen, Q. Wu, H. Guo, Z. Lin, J. Li, and W. Yi, "Evidence for quasar fast outflows being accelerated at the scale of tens of parsecs," *Science Advances*, vol. 8, no. 6, p. eabk3291, Feb. 2022.

[131] K. M. Leighly, D. M. Terndrup, S. C. Gallagher, G. T. Richards, and M. Dietrich, "The z = 0.54 LoBAL Quasar SDSS J085053.12+445122.5. I. Spectral Synthesis Analysis Reveals a Massive Outflow," *The Astrophysical Journal*, vol. 866, no. 1, p. 7, Oct. 2018.

[132] C. P. Ahn, R. Alexandroff, C. Allende Prieto, S. F. Anderson, T. Anderton, B. H. Andrews, É. Aubourg, S. Bailey, E. Balbinot, R. Barnes, J. Bautista, T. C. Beers,

A. Beifiori, A. A. Berlind, V. Bhardwaj, D. Bizyaev, C. H. Blake, M. R. Blanton, M. Blomqvist, J. J. Bochanski, A. S. Bolton, A. Borde, J. Bovy, W. N. Brandt, J. Brinkmann, P. J. Brown, J. R. Brownstein, K. Bundy, N. G. Busca, W. Carithers, A. R. Carnero, M. A. Carr, D. I. Casetti-Dinescu, Y. Chen, C. Chiappini, J. Comparat, N. Connolly, J. R. Crepp, S. Cristiani, R. A. C. Croft, A. J. Cuesta, L. N. da Costa, J. R. A. Davenport, K. S. Dawson, R. de Putter, N. De Lee, T. Delubac, S. Dhital, A. Ealet, G. L. Ebelke, E. M. Edmondson, D. J. Eisenstein, S. Escoffier, M. Esposito, M. L. Evans, X. Fan, B. Femenía Castellá, E. Fernández Alvar, L. D. Ferreira, N. Filiz Ak, H. Finley, S. W. Fleming, A. Font-Ribera, P. M. Frinchaboy, D. A. García-Hernández, A. E. García Pérez, J. Ge, R. Génova-Santos, B. A. Gillespie, L. Girardi, J. I. González Hernández, E. K. Grebel, J. E. Gunn, H. Guo, D. Haggard, J.-C. Hamilton, D. W. Harris, S. L. Hawley, F. R. Hearty, S. Ho, D. W. Hogg, J. A. Holtzman, K. Honscheid, J. Huehnerhoff, I. I. Ivans, Ž. Ivezić, H. R. Jacobson, L. Jiang, J. Johansson, J. A. Johnson, G. Kauffmann, D. Kirkby, J. A. Kirkpatrick, M. A. Klaene, G. R. Knapp, J.-P. Kneib, J.-M. Le Goff, A. Leauthaud, K.-G. Lee, Y. S. Lee, D. C. Long, C. P. Loomis, S. Lucatello, B. Lundgren, R. H. Lupton, B. Ma, Z. Ma, N. MacDonald, C. E. Mack, S. Mahadevan, M. A. G. Maia, S. R. Majewski, M. Makler, E. Malanushenko, V. Malanushenko, A. Manchado, R. Mandelbaum, M. Manera, C. Maraston, D. Margala, S. L. Martell, C. K. McBride, I. D. McGreer, R. G. McMahon, B. Ménard, S. Meszaros, J. Miralda-Escudé, A. D. Montero-Dorta, F. Montesano, H. L. Morrison, D. Muna, J. A. Munn, H. Murayama, A. D. Myers, A. F. Neto, D. C. Nguyen, R. C. Nichol, D. L. Nidever, P. Noterdaeme, S. E. Nuza, R. L. C. Ogando, M. D. Olmstead, D. J. Oravetz, R. Owen, N. Padmanabhan, N. Palanque-Delabrouille, K. Pan, J. K. Parejko, P. Parihar, I. Pâris, P. Pattarakijwanich, J. Pepper, W. J. Percival, I. Pérez-Fournon, I. Pérez-Ràfols, P. Petitjean, J. Pforr, M. M. Pieri, M. H. Pinsonneault, G. F. Porto de Mello, F. Prada, A. M. Price-Whelan, M. J. Raddick,

R. Rebolo, J. Rich, G. T. Richards, A. C. Robin, H. J. Rocha-Pinto, C. M. Rockosi, N. A. Roe, A. J. Ross, N. P. Ross, G. Rossi, J. A. Rubiño-Martin, L. Samushia, J. Sanchez Almeida, A. G. Sánchez, B. Santiago, C. Sayres, D. J. Schlegel, K. J. Schlesinger, S. J. Schmidt, D. P. Schneider, M. Schultheis, A. D. Schwope, C. G. Scóccola, U. Seljak, E. Sheldon, Y. Shen, Y. Shu, J. Simmerer, A. E. Simmons, R. A. Skibba, M. F. Skrutskie, A. Slosar, F. Sobreira, J. S. Sobeck, K. G. Stassun, O. Steele, M. Steinmetz, M. A. Strauss, A. Streblyanska, N. Suzuki, M. E. C. Swanson, T. Tal, A. R. Thakar, D. Thomas, B. A. Thompson, J. L. Tinker, R. Tojeiro, C. A. Tremonti, M. Vargas Magaña, L. Verde, M. Viel, S. K. Vikas, N. P. Vogt, D. A. Wake, J. Wang, B. A. Weaver, D. H. Weinberg, B. J. Weiner, A. A. West, M. White, J. C. Wilson, J. P. Wisniewski, W. M. Wood-Vasey, B. Yanny, C. Yèche, D. G. York, O. Zamora, G. Zasowski, I. Zehavi, G.-B. Zhao, Z. Zheng, G. Zhu, and J. C. Zinn, "The Ninth Data Release of the Sloan Digital Sky Survey: First Spectroscopic Data from the SDSS-III Baryon Oscillation Spectroscopic Survey," *The Astrophysical Journal Supplement Series*, vol. 203, no. 2, p. 21, Dec. 2012.

[133] F. D. Albareti, C. Allende Prieto, A. Almeida, F. Anders, S. Anderson, B. H. Andrews, A. Aragón-Salamanca, M. Argudo-Fernández, E. Armengaud, E. Aubourg, V. Avila-Reese, C. Badenes, S. Bailey, B. Barbuy, K. Barger, J. Barrera-Ballesteros, C. Bartosz, S. Basu, D. Bates, G. Battaglia, F. Baumgarten, J. Baur, J. Bautista, T. C. Beers, F. Belfiore, M. Bershady, S. Bertran de Lis, J. C. Bird, D. Bizyaev, G. A. Blanc, M. Blanton, M. Blomqvist, A. S. Bolton, J. Borissova, J. Bovy, W. N. Brandt, J. Brinkmann, J. R. Brownstein, K. Bundy, E. Burtin, N. G. Busca, H. O. Camacho Chavez, M. Cano Díaz, M. Cappellari, R. Carrera, Y. Chen, B. Cherinka, E. Cheung, C. Chiappini, D. Chojnowski, C.-H. Chuang, H. Chung, R. F. Cirolini, N. Clerc, R. E. Cohen, J. M. Comerford, J. Comparat, J. Correa do Nascimento, M.-C. Cousi-

nou, K. Covey, J. D. Crane, R. Croft, K. Cunha, J. Darling, J. Davidson, James W., K. Dawson, L. Da Costa, G. Da Silva Ilha, A. Deconto Machado, T. Delubac, N. De Lee, A. De la Macorra, S. De la Torre, A. M. Diamond-Stanic, J. Donor, J. J. Downes, N. Drory, C. Du, H. Du Mas des Bourboux, T. Dwelly, G. Ebelke, A. Eigenbrot, D. J. Eisenstein, Y. P. Elsworth, E. Emsellem, M. Eracleous, S. Escoffier, M. L. Evans, J. Falcón-Barroso, X. Fan, G. Favole, E. Fernandez-Alvar, J. G. Fernandez-Trincado, D. Feuillet, S. W. Fleming, A. Font-Ribera, G. Freischlad, P. Frinchaboy, H. Fu, Y. Gao, R. A. Garcia, R. Garcia-Dias, D. A. Garcia-Hernández, A. E. Garcia Pérez, P. Gaulme, J. Ge, D. Geisler, B. Gillespie, H. Gil Marin, L. Girardi, D. Goddard, Y. Gomez Maqueo Chew, V. Gonzalez-Perez, K. Grabowski, P. Green, C. J. Grier, T. Grier, H. Guo, J. Guy, A. Hagen, M. Hall, P. Harding, R. E. Harley, S. Hasselquist, S. Hawley, C. R. Hayes, F. Hearty, S. Hekker, H. Hernandez Toledo, S. Ho, D. W. Hogg, K. Holley-Bockelmann, J. A. Holtzman, P. H. Holzer, J. Hu, D. Huber, T. A. Hutchinson, H. S. Hwang, H. J. Ibarra-Medel, I. I. Ivans, K. Ivory, K. Jaehnig, T. W. Jensen, J. A. Johnson, A. Jones, E. Jullo, T. Kallinger, K. Kinemuchi, D. Kirkby, M. Klaene, J.-P. Kneib, J. A. Kollmeier, I. Lacerna, R. R. Lane, D. Lang, P. Laurent, D. R. Law, A. Leauthaud, J.-M. Le Goff, C. Li, C. Li, N. Li, R. Li, F.-H. Liang, Y. Liang, M. Lima, L. Lin, L. Lin, Y.-T. Lin, C. Liu, D. Long, S. Lucatello, N. MacDonald, C. L. MacLeod, J. T. Mackereth, S. Mahadevan, M. A. G. Maia, R. Maiolino, S. R. Majewski, O. Malanushenko, V. Malanushenko, N. D. Mallmann, A. Manchado, C. Maraston, R. Marques-Chaves, I. Martinez Valpuesta, K. L. Masters, S. Mathur, I. D. McGreer, A. Merloni, M. R. Merrifield, S. Mészáros, A. Meza, A. Miglio, I. Minchev, K. Molaverdikhani, A. D. Montero-Dorta, B. Mosser, D. Muna, A. Myers, P. Nair, K. Nandra, M. Ness, J. A. Newman, R. C. Nichol, D. L. Nidever, C. Nitschelm, J. O'Connell, A. Oravetz, D. J. Oravetz, Z. Pace, N. Padilla, N. Palanque-Delabrouille, K. Pan, J. Parejko, I. Paris, C. Park, J. A. Peacock, S. Peirani, M. Pellejero-Ibanez,

S. Penny, W. J. Percival, J. W. Percival, I. Perez-Fournon, P. Petitjean, M. Pieri, M. H. Pinsonneault, A. Pisani, F. Prada, A. Prakash, N. Price-Jones, M. J. Raddick, M. Rahman, A. Raichoor, S. Barboza Rembold, A. M. Reyna, J. Rich, H. Richstein, J. Ridl, R. A. Riffel, R. Riffel, H.-W. Rix, A. C. Robin, C. M. Rockosi, S. Rodríguez-Torres, T. S. Rodrigues, N. Roe, A. Roman Lopes, C. Román-Zúñiga, A. J. Ross, G. Rossi, J. Ruan, R. Ruggeri, J. C. Runnoe, S. Salazar-Albornoz, M. Salvato, S. F. Sanchez, A. G. Sanchez, J. R. Sanchez-Gallego, B. X. Santiago, R. Schiavon, J. S. Schimoia, E. Schlafly, D. J. Schlegel, D. P. Schneider, R. Schönrich, M. Schultheis, A. Schwope, H.-J. Seo, A. Serenelli, B. Sesar, Z. Shao, M. Shetrone, M. Shull, V. Silva Aguirre, M. F. Skrutskie, A. Slosar, M. Smith, V. V. Smith, J. Sobeck, G. Somers, D. Souto, D. V. Stark, K. G. Stassun, M. Steinmetz, D. Stello, T. Storchi Bergmann, M. A. Strauss, A. Streblyanska, G. S. Stringfellow, G. Suarez, J. Sun, M. Taghizadeh-Popp, B. Tang, C. Tao, J. Tayar, M. Tembe, D. Thomas, J. Tinker, R. Tojeiro, C. Tremonti, N. Troup, J. R. Trump, E. Unda-Sanzana, O. Valenzuela, R. Van den Bosch, M. Vargas-Magaña, J. A. Vazquez, S. Villanova, M. Vivek, N. Vogt, D. Wake, R. Walterbos, Y. Wang, E. Wang, B. A. Weaver, A.-M. Weijmans, D. H. Weinberg, K. B. Westfall, D. G. Whelan, E. Wilcots, V. Wild, R. A. Williams, J. Wilson, W. M. Wood-Vasey, D. Wylezalek, T. Xiao, R. Yan, M. Yang, J. E. Ybarra, C. Yeche, F.-T. Yuan, N. Zakamska, O. Zamora, G. Zasowski, K. Zhang, C. Zhao, G.-B. Zhao, Z. Zheng, Z. Zheng, Z.-M. Zhou, G. Zhu, J. C. Zinn, and H. Zou, "The 13th Data Release of the Sloan Digital Sky Survey: First Spectroscopic Data from the SDSS-IV Survey Mapping Nearby Galaxies at Apache Point Observatory," *The Astrophysical Journal Supplement Series*, vol. 233, no. 2, p. 25, Dec. 2017.

[134] T. Zafar, A. Popping, and C. Péroux, "The ESO UVES advanced data products quasar sample. I. Dataset and new N_{HI} measurements of damped absorbers," *Astronomy &*

Astrophysics, vol. 556, p. A140, Aug. 2013.

[135] E. L. Fitzpatrick, "Correcting for the Effects of Interstellar Extinction," *The Publications of the Astronomical Society of the Pacific*, vol. 111, no. 755, pp. 63–75, Jan. 1999.

[136] R. Barlow, "Asymmetric Errors," in *Statistical Problems in Particle Physics, Astrophysics, and Cosmology*, L. Lyons, R. Mount, and R. Reitmeyer, Eds., Jan. 2003, p. 250.

[137] N. Arav, C. Chamberlain, G. A. Kriss, J. S. Kaastra, M. Cappi, M. Mehdipour, P. O. Petrucci, K. C. Steenbrugge, E. Behar, S. Bianchi, R. Boissay, G. Branduardi-Raymont, E. Costantini, J. C. Ely, J. Ebrero, L. di Gesu, F. A. Harrison, S. Kaspi, J. Malzac, B. De Marco, G. Matt, K. P. Nandra, S. Paltani, B. M. Peterson, C. Pinto, G. Ponti, F. Pozo Nuñez, A. De Rosa, H. Seta, F. Ursini, C. P. de Vries, D. J. Walton, and M. Whewell, "Anatomy of the AGN in NGC 5548. II. The spatial, temporal, and physical nature of the outflow from HST/COS Observations," *Astronomy & Astrophysics*, vol. 577, p. A37, May 2015.

[138] M. Vestergaard and B. M. Peterson, "Determining Central Black Hole Masses in Distant Active Galaxies and Quasars. II. Improved Optical and UV Scaling Relationships," *The Astrophysical Journal*, vol. 641, no. 2, pp. 689–709, Apr. 2006.

[139] L. Coatman, P. C. Hewett, M. Banerji, G. T. Richards, J. F. Hennawi, and J. X. Prochaska, "Correcting C IV-based virial black hole masses," *Monthly Notices of the Royal Astronomical Society*, vol. 465, no. 2, pp. 2120–2142, Feb. 2017.

[140] C. Chamberlain and N. Arav, "Large-scale outflow in quasar LBQS J1206+1052: HST/COS observations," *Monthly Notices of the Royal Astronomical Society*, vol. 454, no. 1, pp. 675–680, Nov. 2015.

[141] C. J. Grier, W. N. Brandt, P. B. Hall, J. R. Trump, N. Filiz Ak, S. F. Anderson, P. J. Green, D. P. Schneider, M. Sun, M. Vivek, T. G. Beatty, J. R. Brownstein, and A. Roman-Lopes, "C IV Broad Absorption Line Acceleration in Sloan Digital Sky Survey Quasars," *The Astrophysical Journal*, vol. 824, no. 2, p. 130, Jun. 2016.

[142] M. Murphy. (2018, Oct.) MTMurphy77/UVES_SQUAD_DR1: First data release of the UVES Spectral Quasar Absorption Database (SQUAD). Zenodo. [Online]. Available: https://doi.org/10.5281/zenodo.1463251

[143] C. Stoughton, R. H. Lupton, M. Bernardi, M. R. Blanton, S. Burles, F. J. Castander, A. J. Connolly, D. J. Eisenstein, J. A. Frieman, G. S. Hennessy, R. B. Hindsley, Ž. Ivezić, S. Kent, P. Z. Kunszt, B. C. Lee, A. Meiksin, J. A. Munn, H. J. Newberg, R. C. Nichol, T. Nicinski, J. R. Pier, G. T. Richards, M. W. Richmond, D. J. Schlegel, J. A. Smith, M. A. Strauss, M. SubbaRao, A. S. Szalay, A. R. Thakar, D. L. Tucker, D. E. Vanden Berk, B. Yanny, J. K. Adelman, J. Anderson, John E., S. F. Anderson, J. Annis, N. A. Bahcall, J. A. Bakken, M. Bartelmann, S. Bastian, A. Bauer, E. Berman, H. Böhringer, W. N. Boroski, S. Bracker, C. Briegel, J. W. Briggs, J. Brinkmann, R. Brunner, L. Carey, M. A. Carr, B. Chen, D. Christian, P. L. Colestock, J. H. Crocker, I. Csabai, P. C. Czarapata, J. Dalcanton, A. F. Davidsen, J. E. Davis, W. Dehnen, S. Dodelson, M. Doi, T. Dombeck, M. Donahue, N. Ellman, B. R. Elms, M. L. Evans, L. Eyer, X. Fan, G. R. Federwitz, S. Friedman, M. Fukugita, R. Gal, B. Gillespie, K. Glazebrook, J. Gray, E. K. Grebel, B. Greenawalt, G. Greene, J. E. Gunn, E. de Haas, Z. Haiman, M. Haldeman, P. B. Hall, M. Hamabe, B. Hansen, F. H. Harris, H. Harris, M. Harvanek, S. L. Hawley, J. J. E. Hayes, T. M. Heckman, A. Helmi, A. Henden, C. J. Hogan, D. W. Hogg, D. J. Holmgren, J. Holtzman, C.-H. Huang, C. Hull, S.-I. Ichikawa, T. Ichikawa, D. E. Johnston, G. Kauffmann, R. S. J. Kim, T. Kimball, E. Kinney, M. Klaene, S. J. Kleinman, A. Klypin, G. R.

Knapp, J. Korienek, J. Krolik, R. G. Kron, J. Krzesiński, D. Q. Lamb, R. F. Leger, S. Limmongkol, C. Lindenmeyer, D. C. Long, C. Loomis, J. Loveday, B. MacKinnon, E. J. Mannery, P. M. Mantsch, B. Margon, P. McGehee, T. A. McKay, B. McLean, K. Menou, A. Merelli, H. J. Mo, D. G. Monet, O. Nakamura, V. K. Narayanan, T. Nash, J. Neilsen, Eric H., P. R. Newman, A. Nitta, M. Odenkirchen, N. Okada, S. Okamura, J. P. Ostriker, R. Owen, A. G. Pauls, J. Peoples, R. S. Peterson, D. Petravick, A. Pope, R. Pordes, M. Postman, A. Prosapio, T. R. Quinn, R. Rechenmacher, C. H. Rivetta, H.-W. Rix, C. M. Rockosi, R. Rosner, K. Ruthmansdorfer, D. Sandford, D. P. Schneider, R. Scranton, M. Sekiguchi, G. Sergey, R. Sheth, K. Shimasaku, S. Smee, S. A. Snedden, A. Stebbins, C. Stubbs, I. Szapudi, P. Szkody, G. P. Szokoly, S. Tabachnik, Z. Tsvetanov, A. Uomoto, M. S. Vogeley, W. Voges, P. Waddell, R. Walterbos, S.-i. Wang, M. Watanabe, D. H. Weinberg, R. L. White, S. D. M. White, B. Wilhite, D. Wolfe, N. Yasuda, D. G. York, I. Zehavi, and W. Zheng, "Sloan Digital Sky Survey: Early Data Release," *The Astronomical Journal*, vol. 123, no. 1, pp. 485–548, Jan. 2002.

[144] H. Aihara, C. Allende Prieto, D. An, S. F. Anderson, É. Aubourg, E. Balbinot, T. C. Beers, A. A. Berlind, S. J. Bickerton, D. Bizyaev, M. R. Blanton, J. J. Bochanski, A. S. Bolton, J. Bovy, W. N. Brandt, J. Brinkmann, P. J. Brown, J. R. Brownstein, N. G. Busca, H. Campbell, M. A. Carr, Y. Chen, C. Chiappini, J. Comparat, N. Connolly, M. Cortes, R. A. C. Croft, A. J. Cuesta, L. N. da Costa, J. R. A. Davenport, K. Dawson, S. Dhital, A. Ealet, G. L. Ebelke, E. M. Edmondson, D. J. Eisenstein, S. Escoffier, M. Esposito, M. L. Evans, X. Fan, B. Femenía Castellá, A. Font-Ribera, P. M. Frinchaboy, J. Ge, B. A. Gillespie, G. Gilmore, J. I. González Hernández, J. R. Gott, A. Gould, E. K. Grebel, J. E. Gunn, J.-C. Hamilton, P. Harding, D. W. Harris, S. L. Hawley, F. R. Hearty, S. Ho, D. W. Hogg, J. A. Holtzman, K. Honscheid,

N. Inada, I. I. Ivans, L. Jiang, J. A. Johnson, C. Jordan, W. P. Jordan, E. A. Kazin, D. Kirkby, M. A. Klaene, G. R. Knapp, J.-P. Kneib, C. S. Kochanek, L. Koesterke, J. A. Kollmeier, R. G. Kron, H. Lampeitl, D. Lang, J.-M. Le Goff, Y. S. Lee, Y.-T. Lin, D. C. Long, C. P. Loomis, S. Lucatello, B. Lundgren, R. H. Lupton, Z. Ma, N. MacDonald, S. Mahadevan, M. A. G. Maia, M. Makler, E. Malanushenko, V. Malanushenko, R. Mandelbaum, C. Maraston, D. Margala, K. L. Masters, C. K. McBride, P. M. McGehee, I. D. McGreer, B. Ménard, J. Miralda-Escudé, H. L. Morrison, F. Mullally, D. Muna, J. A. Munn, H. Murayama, A. D. Myers, T. Naugle, A. F. Neto, D. C. Nguyen, R. C. Nichol, R. W. O'Connell, R. L. C. Ogando, M. D. Olmstead, D. J. Oravetz, N. Padmanabhan, N. Palanque-Delabrouille, K. Pan, P. Pandey, I. Pâris, W. J. Percival, P. Petitjean, R. Pfaffenberger, J. Pforr, S. Phleps, C. Pichon, M. M. Pieri, F. Prada, A. M. Price-Whelan, M. J. Raddick, B. H. F. Ramos, C. Reylé, J. Rich, G. T. Richards, H.-W. Rix, A. C. Robin, H. J. Rocha-Pinto, C. M. Rockosi, N. A. Roe, E. Rollinde, A. J. Ross, N. P. Ross, B. M. Rossetto, A. G. Sánchez, C. Sayres, D. J. Schlegel, K. J. Schlesinger, S. J. Schmidt, D. P. Schneider, E. Sheldon, Y. Shu, J. Simmerer, A. E. Simmons, T. Sivarani, S. A. Snedden, J. S. Sobeck, M. Steinmetz, M. A. Strauss, A. S. Szalay, M. Tanaka, A. R. Thakar, D. Thomas, J. L. Tinker, B. M. Tofflemire, R. Tojeiro, C. A. Tremonti, J. Vandenberg, M. Vargas Magaña, L. Verde, N. P. Vogt, D. A. Wake, J. Wang, B. A. Weaver, D. H. Weinberg, M. White, S. D. M. White, B. Yanny, N. Yasuda, C. Yeche, and I. Zehavi, "The Eighth Data Release of the Sloan Digital Sky Survey: First Data from SDSS-III," *The Astrophysical Journal Supplement Series*, vol. 193, no. 2, p. 29, Apr. 2011.

[145] Z. He, G. Liu, T. Wang, G. Mou, R. Green, W. Bian, H. Wang, L. C. Ho, M. Sun, L. Shen, N. Arav, C. Chen, Q. Wu, H. Guo, Z. Lin, J. Li, and W. Yi, "Evidence for quasar fast outflows being accelerated at the scale of tens of parsecs," *Science*

Advances, vol. 8, no. 6, p. eabk3291, Feb. 2022.

[146] N. Arav, J. R. Gabel, K. T. Korista, J. S. Kaastra, G. A. Kriss, E. Behar, E. Costantini, C. M. Gaskell, A. Laor, C. N. Kodituwakku, D. Proga, M. Sako, J. E. Scott, and K. C. Steenbrugge, "Chemical Abundances in an AGN Environment: X-Ray/UV Campaign on the Markarian 279 Outflow," *The Astrophysical Journal*, vol. 658, no. 2, pp. 829–839, Apr. 2007.

[147] A. King and S. I. Muldrew, "Black hole winds II: Hyper-Eddington winds and feedback," *Monthly Notices of the Royal Astronomical Society*, vol. 455, no. 2, pp. 1211–1217, Jan. 2016.

[148] H. Choi, K. M. Leighly, D. M. Terndrup, S. C. Gallagher, and G. T. Richards, "Discovery of a Remarkably Powerful Broad Absorption-line Quasar Outflow in SDSS J135246.37+423923.5," *The Astrophysical Journal*, vol. 891, no. 1, p. 53, Mar. 2020.

[149] K. M. Leighly, H. Choi, C. DeFrancesco, J. Voelker, D. M. Terndrup, S. C. Gallagher, and G. T. Richards, "The Physical Properties of Low-redshift FeLoBAL Quasars. II. The Rest-frame Optical Emission Line Properties," *The Astrophysical Journal*, vol. 935, no. 2, p. 92, Aug. 2022.

[150] P. C. Hewett and V. Wild, "Improved redshifts for SDSS quasar spectra," *Monthly Notices of the Royal Astronomical Society*, vol. 405, no. 4, pp. 2302–2316, Jul. 2010.

[151] L. Spitzer, *Physical processes in the interstellar medium*. Wiley, 1978.

[152] J. R. Trump, P. B. Hall, T. A. Reichard, G. T. Richards, D. P. Schneider, D. E. Vanden Berk, G. R. Knapp, S. F. Anderson, X. Fan, J. Brinkman, S. J. Kleinman, and A. Nitta, "A Catalog of Broad Absorption Line Quasars from the Sloan Digital

Sky Survey Third Data Release," *The Astrophysical Journal Supplementary Series*, vol. 165, no. 1, pp. 1–18, Jul. 2006.

[153] P. Virtanen, R. Gommers, T. E. Oliphant, M. Haberland, T. Reddy, D. Cournapeau, E. Burovski, P. Peterson, W. Weckesser, J. Bright, S. J. van der Walt, M. Brett, J. Wilson, K. J. Millman, N. Mayorov, A. R. J. Nelson, E. Jones, R. Kern, E. Larson, C. J. Carey, İ. Polat, Y. Feng, E. W. Moore, J. VanderPlas, D. Laxalde, J. Perktold, R. Cimrman, I. Henriksen, E. A. Quintero, C. R. Harris, A. M. Archibald, A. H. Ribeiro, F. Pedregosa, P. van Mulbregt, and SciPy 1.0 Contributors, "SciPy 1.0: Fundamental Algorithms for Scientific Computing in Python," *Nature Methods*, vol. 17, pp. 261–272, 2020.

[154] C. R. Harris, K. J. Millman, S. J. van der Walt, R. Gommers, P. Virtanen, D. Cournapeau, E. Wieser, J. Taylor, S. Berg, N. J. Smith, R. Kern, M. Picus, S. Hoyer, M. H. van Kerkwijk, M. Brett, A. Haldane, J. F. del Río, M. Wiebe, P. Peterson, P. Gérard-Marchant, K. Sheppard, T. Reddy, W. Weckesser, H. Abbasi, C. Gohlke, and T. E. Oliphant, "Array programming with NumPy," *Nature*, vol. 585, no. 7825, pp. 357–362, Sep. 2020. [Online]. Available: https://doi.org/10.1038/s41586-020-2649-2

[155] J. Reback, W. McKinney, jbrockmendel, J. V. den Bossche, T. Augspurger, P. Cloud, S. Hawkins, gfyoung, Sinhrks, M. Roeschke, A. Klein, T. Petersen, J. Tratner, C. She, W. Ayd, S. Naveh, patrick, M. Garcia, J. Schendel, A. Hayden, D. Saxton, V. Jancauskas, M. Gorelli, R. Shadrach, A. McMaster, P. Battiston, S. Seabold, K. Dong, chris b1, and h vetinari. (2021, Apr.) pandas-dev/pandas: Pandas 1.2.4. Zenodo. [Online]. Available: https://doi.org/10.5281/zenodo.4681666

[156] Wes McKinney, "Data Structures for Statistical Computing in Python," in *Proceedings*

of the 9th Python in Science Conference, Stéfan van der Walt and Jarrod Millman, Eds., 2010, pp. 56 – 61.

[157] J. D. Hunter, "Matplotlib: A 2d graphics environment," *Computing in Science & Engineering*, vol. 9, no. 3, pp. 90–95, 2007.

[158] A. E. Wright, D. C. Morton, B. A. Peterson, and D. L. Jauncey, "Spectroscopy of the QSO pair PKS 0254-334." *Monthly Notices of the Royal Astronomical Society*, vol. 199, pp. 81–91, Apr. 1982.

[159] H. Tananbaum, Y. Avni, G. Branduardi, M. Elvis, G. Fabbiano, E. Feigelson, R. Giacconi, J. P. Henry, J. P. Pye, A. Soltan, and G. Zamorani, "X-ray studies of quasars with the Einstein Observatory." *The Astrophysical Journal*, vol. 234, pp. L9–L13, Nov. 1979.

[160] M. A. Sobolewska, M. Gierliński, and A. Siemiginowska, "What can we learn about quasars from oxmeasurements in galactic black hole binaries?" *Monthly Notices of the Royal Astronomical Society*, vol. 394, no. 3, p. 1640–1648, Apr. 2009. [Online]. Available: http://dx.doi.org/10.1111/j.1365-2966.2009.14436.x

[161] S. C. Gallagher, W. N. Brandt, G. Chartas, R. Priddey, G. P. Garmire, and R. M. Sambruna, "An Exploratory Chandra Survey of a Well-defined Sample of 35 Large Bright Quasar Survey Broad Absorption Line Quasars," *The Astrophysical Journal*, vol. 644, no. 2, pp. 709–724, Jun. 2006.

[162] E. M. Tilton and J. M. Shull, "Ultraviolet Emission-line Correlations in HST/COS Spectra of Active Galactic Nuclei: Single-epoch Black Hole Masses," *The Astrophysical Journal*, vol. 774, no. 1, p. 67, Sep. 2013.

[163] H. Netzer, S. Kaspi, E. Behar, W. N. Brandt, D. Chelouche, I. M. George, D. M.

Crenshaw, J. R. Gabel, F. W. Hamann, S. B. Kraemer, G. A. Kriss, K. Nandra, B. M. Peterson, J. C. Shields, and T. J. Turner, "The Ionized Gas and Nuclear Environment in NGC 3783. IV. Variability and Modeling of the 900 Kilosecond Chandra Spectrum," *The Astrophysical Journal*, vol. 599, no. 2, pp. 933–948, Dec. 2003.